Instabilities of Rotating Liquid Columns and Orientation Dynamics of Spheroids in Shearing Flows

Pulkit Kumar Dubey

Engineering Mechanics Unit
JNCASR

This dissertation is submitted for the degree of
M.S.(Engg.)

July 2020

to my grandmother . . .

Declaration

I hereby declare that except where specific reference is made to the work of others, the contents of this dissertation are original and have not been submitted in whole or in part for consideration for any other degree or qualification in this, or any other university. This dissertation is my own work and contains nothing which is the outcome of work done in collaboration with others, except as specified in the text and Acknowledgements.

Pulkit Kumar Dubey
July 2020

Certificate

I hereby certify that the matter embodied in this thesis entitled **Instabilities of Rotating Liquid Columns and Orientation Dynamics of Spheroids in Shearing Flow**, has been carried out by Mr. Pulkit Kumar Dubey at the Engineering Mechanics Unit, Jawaharlal Nehru Centre for Advanced Scientific Research, Bangalore, India, under my supervision, and that it has not been submitted elsewhere for the award of any degree or diploma.

Dr. Ganesh Subramanian
Professor
Engineering Mechanics Unit
JNCASR, Bangalore
January 2020

Acknowledgements

I would like to thank my advisor, friends, family and the institute for their support through the course of this work.

Abstract

As suggested by the title, the research reported in this thesis concerns two problems.

The first (and main) part of the thesis, which consists of Chapters 1 and 2, concerns the surface-tension-driven instability of rotating liquid columns. This research is motivated by experimental results reported by Prof. Raghuram Govardhan's group that concerned the interaction of a vortex ring with a bubble. The general sequence of events in the experiment involves the initial capture of the bubble within the low-pressure vortex core, its elongation along the circumferential direction into a near-toroidal shape, and subsequent break-up (which also leads to the disruption of the vortex ring in many cases). The authors suggested a possible instability governing the bubble breakup, and the thesis therefore assesses the possibility of a linear instability of such a configuration.

In building towards the stability of the vortex-ring-bubble configuration, the thesis first considers the somewhat classical problem, of the stability of a rotating column of liquid surrounded by air, in Chapter 1. In the absence of rotation, the problem reduces to the classical Rayleigh-Plateau analysis. There has been considerable prior work on this problem in the presence of rotation. Centrifugal forces are expected to destabilize this configuration, and the necessary and sufficient condition for viscous stability has been derived in earlier efforts. In contrast, arguments in the literature, based on the inviscid equations, suggest only a sufficient condition for stability. The clarification of the rather subtle relationship between the inviscid and viscous stability of a rotating column forms the subject matter of Chapter 1. It is shown, based on the inviscid dispersion relation, that there appear inviscidly stable islands within the known viscously unstable region in the Weber-number-axial-wavenumber plane. For each azimuthal wavenumber, there exists a dominant stable island that terminates in a cusp at a critical Weber number. More interestingly, however, it is shown that there very likely exists an infinite number of additional and much smaller satellite islands within the viscously unstable region. The infinite hierarchy of islands that arises is intimately related to the nature of the rotating column spectrum which comprises a pair of capillary modes and an infinity of Coriolis modes. In dynamical systems parlance, the finding is equivalent to an infinite sequence of cusp catastrophes. The existence of inviscid islands has implications even for the viscous scenario. The growth rate outside the islands must asymptote to an order

unity value as the Reynolds number approaches infinity, while that within must decay with increasing Reynolds number. As a result, just above the threshold Weber number, where there exist a large number of inviscid islands, an increase in axial wavenumber should lead to a rapid variation in the long-time growth rate for any large but finite Reynolds number.

Chapter 2 moves towards the stability of the vortex-column-bubble configuration via a sequence of simpler related configurations. The most elementary of these is the configuration inverse to the rotating liquid column in air examined in chapter 1 – an air column surrounded by a body of rigidly rotating liquid. This configuration is stabilized by centrifugal forces, and is, in fact, linearly stable to all perturbations above a fairly modest Weber number. Thus, such a configuration is too simple to explain the apparent instability observed in the experiments above, which occurs at fairly large Weber numbers. The next step in complexity is to confine the rigidly rotating liquid to an annular cylindrical region, with an irrotational azimuthal flow in the exterior; in other words, the linear stability of a Rankine-vortex-like configuration, but with an air column embedded within the vortex core. An analysis of this configuration, however, reveals no instability. The final step in complexity is to incorporate the self-induced straining flow characteristic of the original vortex-ring-bubble configuration. For thin rings, this effect may be incorporated via an externally imposed (linear) straining flow on the above Rankine-vortex-air-core configuration. As in the original case of a vortex ring (analysed jointly by Moore, Saffman, Tsai and Widnall, and termed the MSTW instability), an instability is expected as the result of a parametric resonance. The possibility of an instability of the aforementioned strained configuration may therefore be assessed based on the dispersion curve intersections in the absence of the strain. Accordingly, the nature of the dispersion curve intersections which, in addition to the Coriolis mode intersections for the original vortex ring, now include novel classes of capillary-capillary and capillary-Coriolis intersections, is studied as a function of the Weber number and the radius ratio of the air core to the vortex core. It is thereby shown that, unlike the original MSTW instability, the straining flow is likely to induce a resonance between modes corresponding to azimuthal numbers of zero and two at large Weber numbers.

The third and final chapter examines the orientation dynamics of spheroids (both prolate and oblate) in the one parameter family of planar linear flows. The objective is to assess the effect of fluid inertia on the orientation dynamics. In the inertialess limit, spheroids are known to rotate along Jeffery orbits in planar linear flows, provided the ratio of vorticity to strain is above an aspect-ratio-dependent threshold. The degeneracy implied by the existence of closed orbits in orientation space is resolved with the inclusion of fluid inertia. The effect of fluid inertia in planar linear flows was analysed earlier within a one-dimensional framework, that involved the derivation of the orbital drift, with the sign of the orbital drift determining

the stability of particular Jeffery orbits (for instance, the spinning and tumbling modes). The one-dimensional analysis, in terms of the Jeffery orbit constant, is only valid when the inertial drift occurs on a time scale asymptotically long compared to the Jeffery period. This assumption invariably breaks down in the vicinity of the aforementioned aspect-ratio-dependent threshold, when the trajectory topology changes from an elliptic to a hyperbolic type. Thus, the precise nature of bifurcations in the orientation dynamics, in the vicinity of this threshold, would require an analysis of the full two-dimensional equations comprising the two Jeffery angles. The third chapter takes the first steps towards characterizing the sequence of bifurcations that occur for both prolate and oblate spheroids at small but finite Reynolds numbers. The picture that comes about is considerably more complicated than that revealed by the earlier one-dimensional analysis.

Table of contents

List of figures

Chapter 1

Linear Stability of Rotating Liquid Columns

1.1 Introduction

In this chapter, we consider the linear stability of a rigidly rotating column. The problem is classical - the limit of zero rotation corresponds to the Rayleigh-Plateau instability - and has been well studied since the 1950's. The pertinent literature generally adheres to derivations of the necessary and/or sufficient conditions for stability while largely ignoring an analysis of the complete spectrum which would include the entire ensemble of neutral modes. Although the neutral modes characterize the oscillatory response of a system to small amplitude perturbations, the coalescence of neutral dispersion curves may lead to instabilities. In the following sections, we review earlier works on the instabilities of rotating liquid columns which focus on unstable modes alone and supplement them with a discussion of the entire spectrum.

Before delving further into the subject matter, we briefly note the basic premise of a linear stability analysis and the associated terminology. The objective is to understand the circumstances under which a small perturbation may grow exponentially and destabilize the system. The unperturbed state (henceforth referred to as the *base state*), that is axially symmetric for the problem under consideration, is subject to an elementary modal perturbation which is characterized by its azimuthal wavenumber (n), axial wavenumber (k) and the frequency and/or growth rate (σ). Thus, in presence of the perturbation, a given field takes the form:

$$q = q_0 + \varepsilon \tilde{q} e^{i(n\theta + kz - \sigma t)} \tag{1.1}$$

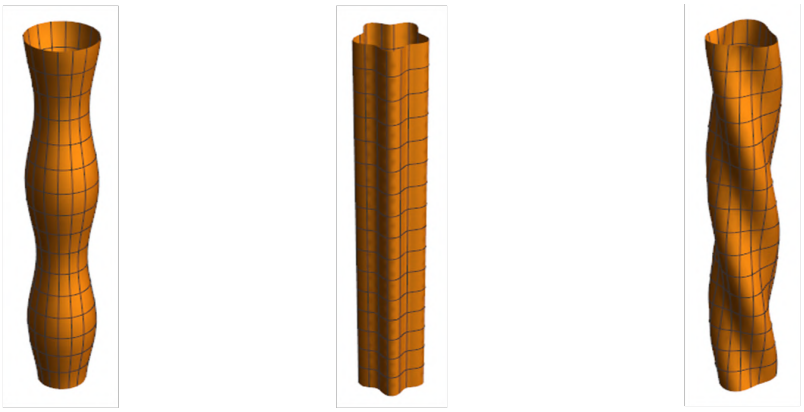

Fig. 1.1 Three possible variations of the perturbations of a liquid column - axisymmetric perturbations (left), Planar perturbations (middle) and three-dimensional perturbations (right).

whereq_0 pertains to the base state and ε is the amplitude of the perturbation (assumed much smaller than any other length scale in the problem). σ, which is complex in the general case, governs the stability of the system. According to the ansatz above, if σ has a positive imaginary part, the perturbations grow exponentially (unstable perturbations) and decay if the imaginary part is negative (stable perturbations). If σ is purely real, the perturbations persist as traveling waves and are termed as the neutral modes of the system.

Based on the azimuthal (n) and axial (k) wavenumber, one can classify the perturbations into three categories (Figure 1.1)

- Axisymmetric perturbations: $n = 0, k \neq 0$
- Planar perturbations: $n \neq 0, k = 0$
- Three-dimensional (or Helical) perturbations: $n \neq 0, k \neq 0$

We study in turn the dispersion curves for each of the aforementioned classes of perturbations on an inviscid rotating liquid column. The nature of the dispersion curves are studied as a function of the relevant dimensionless parameters which include the Weber number $We = \rho\Omega^2 a^3/\gamma$, where ρ is the density of liquid, Ω is angular velocity of the column, a is the radius of the column and γ is the coefficient of surface tension. We begin with the simplest case of a stationary column of liquid.

1.2 The Stationary Liquid Column

In this section we summarize the response of a non-rotating liquid column to the three kinds of perturbations mentioned above, beginning with the axisymmetric perturbations. This is

the Rayleigh-Plateau instability which is responsible for the breakup of a (slow) jet into nearly uniformly sized droplets in response to long wavelength axisymmetric perturbations (the jet may be made equivalent to a stationary column via a Galilean transformation). This instability was identified by Plateau who showed that perturbations with axial wavelength greater than the circumference of the column ($\lambda > 2\pi a$ or, if the wavelength is scaled with the column radius, $k < 1$) reduce the surface area, and thence the surface energy of the resulting column. The column therefore continues to deform so as to lower its surface energy, eventually breaking into droplets. Plateau concluded that the perturbations in a column of liquid would persist as neutral oscillations if $k > 1$ and will grow, leading to a column break up if $0 < k < 1$.

Plateau's analysis was, however, a quasi-static one, and did not account for the inertia associated with the fluid motion driven by the imposed perturbation. Building on Plateau's effort, Rayleigh [13], in 1878, provided a complete linear stability analysis, that accounted for the effects of both inertia and surface tension, and thereby, calculated the wavenumber corresponding to the fastest growing perturbation. Rayleigh obtained an explicit expression for the oscillation frequency (σ) an axisymmetric perturbation with axial wavenumber (k) as

$$\sigma^2 = k(k^2-1)\frac{I_1(k)}{I_0(k)}. \tag{1.2}$$

where the dimensional frequency (σ^*) and the dimensional axial wavenumber (k^*) have been scaled as

$$\sigma = \frac{\sigma^*}{\sqrt{\frac{\gamma}{\rho a^3}}}, \quad k = k^* a$$

Here, γ is the surface tension, ρ is the density of the fluid and a is the radius of the liquid column. The stability criterion for the Rayleigh-Plateau instability is immediately evident from equation (1.2). For $k < 1$, $\sigma^2 < 0$ and σ is purely imaginary. This verifies Plateau's finding that an instability results if $0 < k < 1$. Note that the neglect of inertia in the original quasi-static arguments of Plateau does not alter the threshold, since the growth (or decay) rate becomes asymptotically small in the vicinity of the threshold, and so do inertial forces. For $k > 1$, one obtains two neutral modes. These findings are summarized in fig. 1.2. The purely imaginary eigenvalues (dashed orange curves) indicate a stationary growing and a decaying mode, while the purely real eigenvalues (solid blue curves) indicate neutral modes. It can be seen from fig. 1.2 that as one crosses the stability threshold, the two neutral modes transform to a stable and an unstable mode, with the resulting eigenvalues having a vanishing real part. The resulting eigenvalues have vanishing real parts. This is an example of an *exchange of stabilities* bifurcation [1], where the instability is not oscillatory in nature but

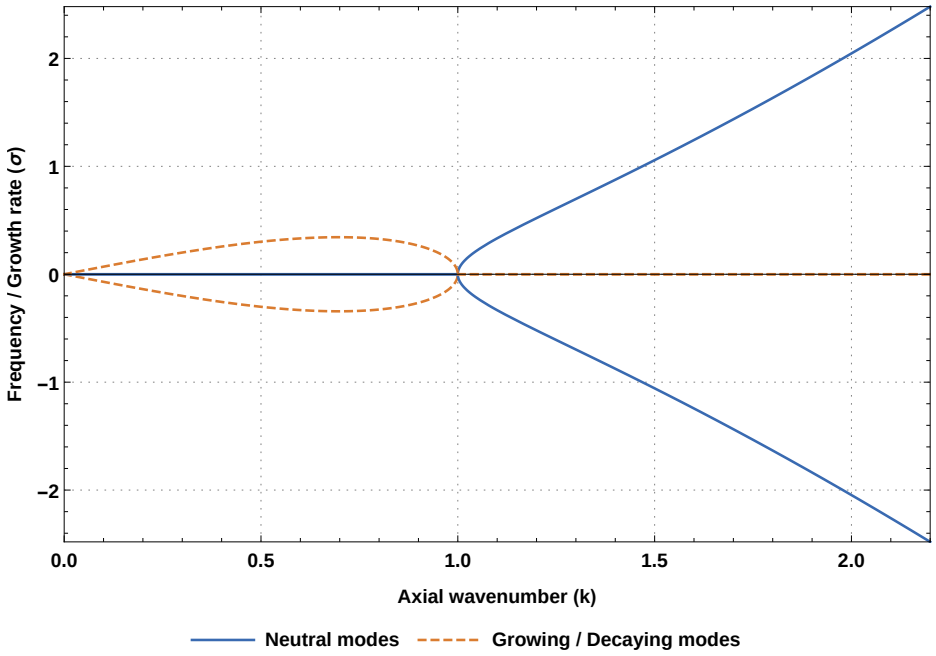

Fig. 1.2 Behaviour of neutral (solid curves), growing (dashed curve) and decaying (dot-dashed curve) modes with wavenumber (k). The eigenvalues for the orange curves are purely imaginary and those for the blue curves are purely real.

grows monotonically in time. The simultaneous presence of a growing and a decaying mode, or a pair of neutral modes which propagate up and down the liquid column, arises from the time reversibility of the underlying Euler equations.

We can further verify some limiting cases of the dispersion relation 1.2. For $k \to \infty$, one obtains

$$\sigma^2 = k\left(k^2-1\right)\frac{I_1(k)}{I_0(k)} \sim k\left(k^2\right)\frac{e^k/\sqrt{2\pi k}}{e^k/\sqrt{2\pi k}} \sim k^3$$

$$\Rightarrow \sigma \propto k^{3/2}$$

which denotes the dispersion relation for capillary waves propagating on an infinite plane interface, with the well known (dimensional) relation $\sigma = \sqrt{\gamma k^3/\rho}$. Hence, in the limit of a large axial wavenumber (short wavelengths), the neutral modes behave as capillary waves moving in opposite directions close to the surface of the column. For small k, we have

$$\sigma^2 = k\left(k^2-1\right)\frac{I_1(k)}{I_0(k)} \sim k(-1)\frac{k/2}{1} \sim \frac{-k^2}{2} \tag{1.3}$$

indicating that the growth rates scale linearly with k for small k.

The dispersion relation (eq. 1.2) allowed Rayleigh to determine the wavenumber corresponding to the fastest growing perturbation ($k_{max} \approx 0.697$, as can be seen from fig. 1.2). That the maximum growth rate occurs at a finite wavelength implies a characteristic drop size that would result from the breakup of the jet. This has indeed been verified in experiments [2]. Considerations of non-linear effects in the analysis leads to the formation of satellite drops seen in the experiments.

The stationary liquid column is stable to planar and three-dimensional perturbations, consistent with quasi-static arguments which show that both these classes of perturbations lead to an increase in the surface area. The general dispersion relation obtained from a linear analysis, when both k and n are non-zero is [2]

$$\sigma^2 = k\frac{I_n'(k)}{I_n(k)}(k^2+n^2-1) \tag{1.4}$$

If $n > 1$, the eigenvalues are always purely real and the perturbations remain neutral. Therefore, only sufficiently long-wavelength axisymmetric perturbations can destabilize the system and lead to droplet formation.

1.3 The Rotating Liquid Column

In this section we analyze the linear stability of a rigidly rotating column of liquid where the base state is given by

$$\begin{aligned} u_r &= 0 \\ u_\theta &= \Omega r \\ u_z &= 0 \\ p &= p_0 + \frac{\rho\Omega^2 r^2}{2} \end{aligned} \tag{1.5}$$

where p_o is an arbitrary baseline pressure on account of incompressibility and Ω is the angular velocity of the rigidly rotating liquid column. The governing equations remain the Euler equations and the continuity equation for an incompressible fluid. The boundary conditions involve equating the radial velocity of the fluid with radial velocity of the interface and ensuring continuity of normal stress at the outer surface of the column.

1.3.1 Axisymmetric Perturbations

The criterion for the stability of a inviscid rotating liquid column to axisymmetric perturbations was first obtained by Hocking [4] as

$$We\,\sigma^2\sqrt{\frac{4}{\sigma^2}-1}\frac{J_0(\alpha)}{J_1(\alpha)}-k\left(k^2-1\right)+We\,k=0 \tag{1.6}$$

where $\alpha = k\sqrt{\frac{4}{\sigma^2}-1}$ and $We = \frac{\rho a^3\Omega^2}{\gamma}$ is the Weber number characterizing the relative importance of centrifugal and surface tension forces. Here, as before, k is scaled with $1/a$ but σ is scaled with Ω as opposed to $\sqrt{\gamma k^3/\rho}$ used in the classical Rayleigh-Plateau analysis. Taking the scaling into account, one recovers the Rayleigh-Plateau dispersion relation in the limit $We \to 0$. Using eq. 1.6, Hocking obtained the necessary and sufficient criterion for stability to be

$$We < k^2 - 1. \tag{1.7}$$

For $We = 0$, eq. 1.7 reduces to $k > 1$, the criterion for stability for the Rayleigh-Plateau problem discussed above. Importantly, eq. 1.7 indicates that, regardless of k, there exists a critical We beyond which the column becomes unstable. Centrifugal forces are destabilizing for the rotating liquid column for all k. Thus, for $0 < k < 1$, centrifugal forces reinforce the original Rayleigh-Plateau instability, while for $k > 1$, there is a competition between the restoring force of surface tension and the destabilizing centrifugal force. It can be seen that the range of unstable wavenumbers has increased from $0 < k < 1$ for the non-rotating case to $0 < k < \sqrt{1+We}$ in the rotating case.

Neutral Modes

In what follows, we focus on the complete spectrum for the rotating liquid column starting with the neutral modes. For the stationary column the entire dynamics, which remain irrotational due to the absence of any base-state vorticity, is described by the pair of modes (whether neutral, growing or decaying) sketched in fig. 1.2 ; the dynamics of rotational perturbations, which do not perturb the column surface (such free-surface perturbations can, in any case, be described by the aforementioned pair of modes) are trivial, and also have a degenerate character. In contrast, rotation and the associated Coriolis forces renders the dynamics of vorticity non-trivial. This is reflected in the spectrum for a rotating liquid column which now contains an infinity of Coriolis-driven modes in addition to the original surface-tension-driven modes (modified by rotation).

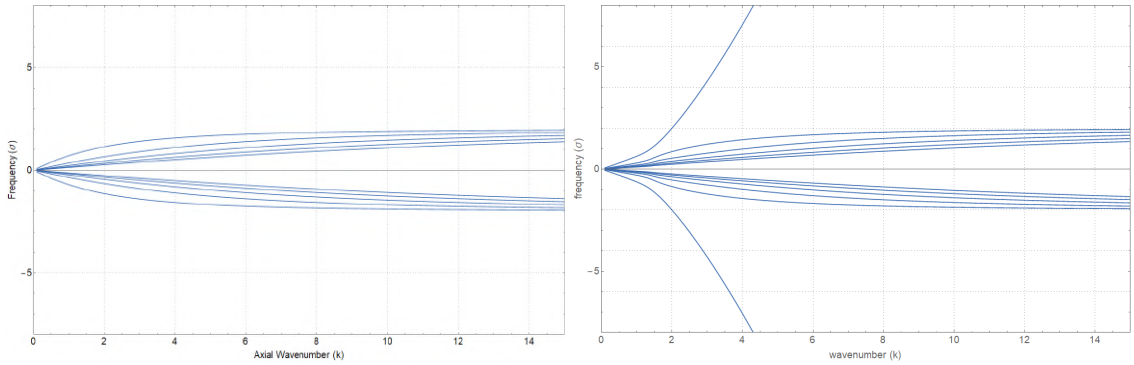

(a) Dispersion curves for axisymmetric perturbations of a Rankine vortex.

(b) Dispersion curves for axisymmetric perturbations of a rotating liquid column. $We = 1$.

Fig. 1.3 The rotating liquid column supports an infinity of Coriolis force dominated modes (akin to those of the Rankine vortex) modified by surface tension and two surface tension dominated modes modified by rotation.

A classical example of a rotating system that supports a discrete spectrum comprising an infinite hierarchy of Coriolis-driven modes is the Rankine vortex (there exists an additional continuous spectrum in this case owing to the irrotational shear outside; see Roy and Subramanian [9]). The discrete spectrum in this case was first determined by Kelvin [18], and the Rankine dispersion curves for axisymmetric perturbations are shown in fig. 1.3a. The corresponding spectrum for a rotating liquid column is shown in fig. 1.3b. The similarity between the two sets of dispersion curves is apparent. Both systems support an infinite sequence of Coriolis-driven modes, with the inner dispersion curves (corresponding to smaller $|\sigma|$) modes having an increasingly fine-scaled radial structure. The rotating liquid column has two additional modes, corresponding to the outermost dispersion curves in fig. 1.3b, that owe their origin to surface tension. We will refer to these as capillary modes modes. Fig. 1.3b shows the family of Coriolis-driven modes along with the two capillary modes and their variation with the wavenumber (k) for $We = 1$. It is apparent from the figure that the two kinds of neutral modes are not distinguished for small wavenumbers, where rotation dominates the character of all neutral modes. On the other hand, it can be seen that the capillary modes (the two outermost modes in fig. 1.3b) follow the $k^{3/2}$ scaling for large k, while the Kelvin modes approach $\sigma = \pm 2$.

Similarly one may explore the behaviour of neutral modes in the limit of small axial wavenumbers. The dispersion relation (eq. (1.6)) in the limit $\sigma, k \to 0$, where the slope (m) of a branch of the dispersion curves is given by $m = \sigma/k$, becomes

$$-m\frac{J_0(2/m)}{J_1(2/m)} = \frac{(1+We)}{2We} \tag{1.8}$$

which can be solved graphically to obtain the slope of the dispersion curves for small k at a fixed We. The largest values of $|m|$ correspond to capillary modes. This can be further simplified for a large modal index (m_i) under the assumption that, for higher modes, $\sigma \ll k$ for small k and therefore $m \ll 1$. Eq. 1.8 then becomes

$$m = -\frac{1+We}{2We}\tan(\frac{2}{m})$$

For a given We, we then have that $\tan(\frac{2}{m}) \to 0$ and thus $\sigma = (\frac{2}{m_i\pi})k$. The linear variation of σ with k is thus explicit for large modal indices.

Having analyzed the variation of frequency with wavenumber k, we proceed to analyze the effect of We on the dispersion curves for the neutral modes (fig. 1.4). If $k \ll \sqrt{We+1}$, the Coriolis force dominates even the capillary modes and these modes also behave as inertial modes. It is only for $k > \sqrt{We+1}$ that the effects of surface tension become apparent and the capillary character of the two modes is seen. It can also be seen from the dispersion relation (eq. 1.6), that if $We \gg k^2 - 1$, the roots are independent of We and vary only with k.

Growing and Decaying modes

We now look at the growing/decaying modes of the rotating liquid column. As indicated before, these modes exist for a range of wavenumbers given by $0 < k < \sqrt{1+We}$. The variation of growth rate with axial wavenumber k, for a set of We has been shown in fig. 1.5. It is clear that the range of unstable wavenumbers increases with increasing We. Note that the unstable modes of a rotating column do not emerge as a result of coalescence of neutral modes, as is the case for the Rayleigh-Plateau instability. The unstable modes of the rotating column arise independently as the stability threshold is crossed. These modes, however, have purely imaginary eigenvalues and therefore the exchange of stabilities still holds i.e the unstable modes grow monotonically without oscillations. Since eigenvalues have no real part, the state of neutral stability is one of rigid rotation.

The fact that the eigenvalue corresponding to the unstable modes goes to zero (both real and imaginary parts) at the curve of marginal stability, can be used to obtain the stability criterion. Taking the limit $\sigma \to 0$, in the dispersion relation (eq. (1.6)), one obtains

$$\begin{aligned} & 2\sigma\, We\, \cot\left(\frac{2k}{\sigma} - \frac{\pi}{4}\right) - k(k^2-1) + We\, k \approx 0 \\ \Rightarrow & -k(k^2-1) + We\, k \approx 0 && \text{(since } \sigma \ll 1\text{)} \\ \Rightarrow & We \approx k^2 - 1 \end{aligned}$$

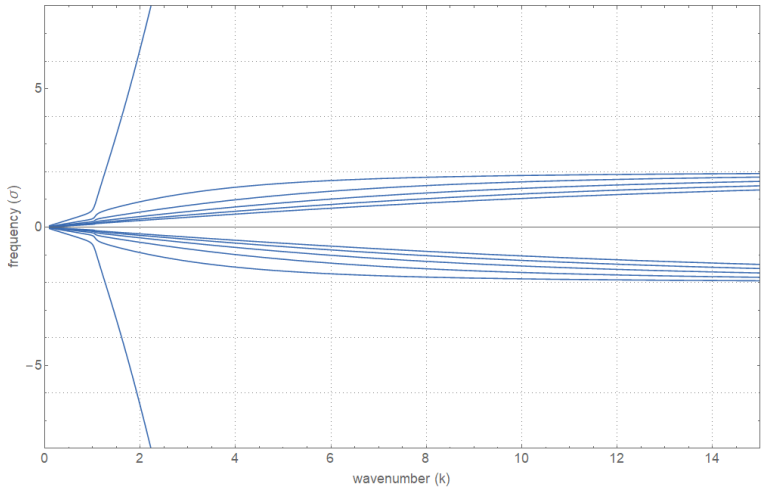

(a) $We = 0.1$

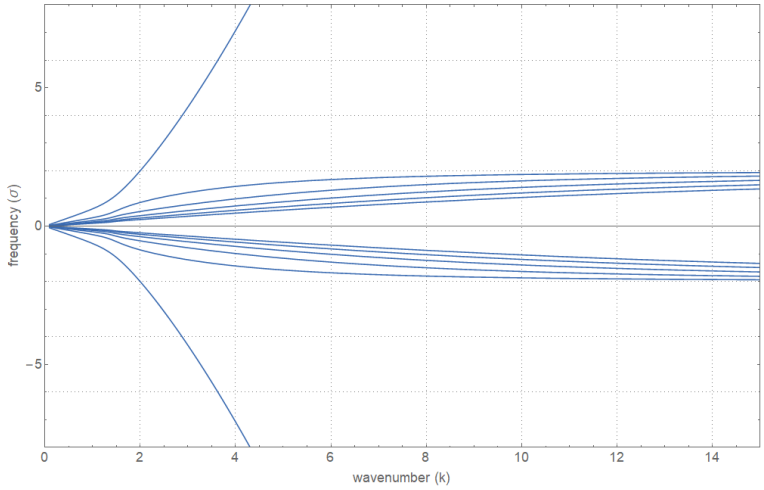

(b) $We = 1$

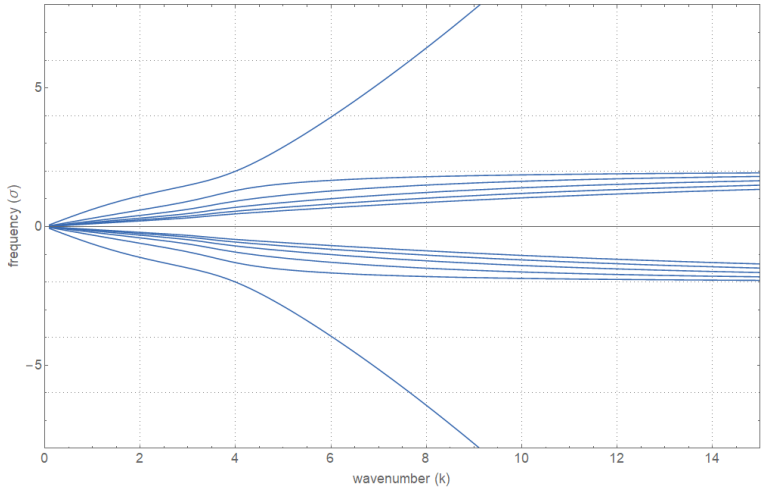

(c) $We = 10$

Fig. 1.4 Variation of the dispersion curves (frequency (σ) vs axial wavenumber (k)) of the rotating liquid column with We

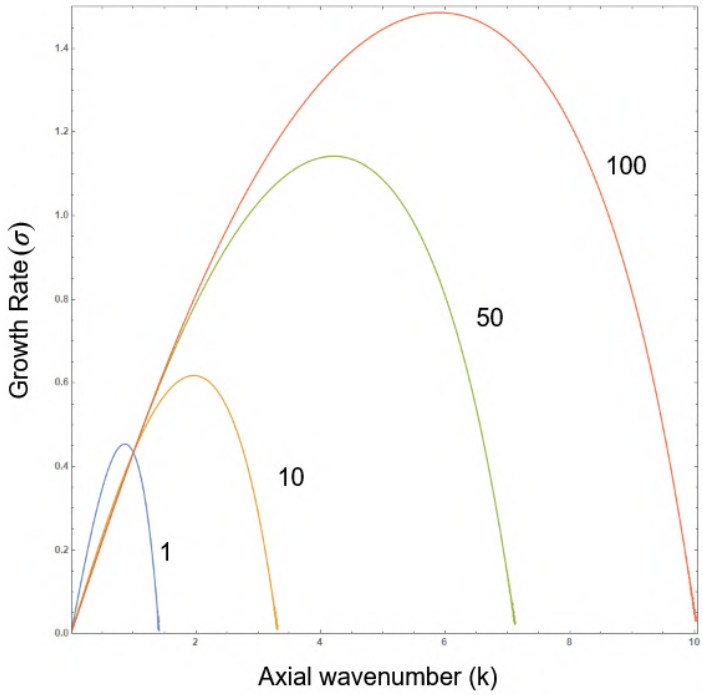

Fig. 1.5 Variation of range of unstable wavenumbers and the maximum growth rate for $We = 1, 10, 50$ and 100 .

which is the criterion for marginal stability, as stated before.

In order to understand the behaviour of unstable modes in the limit of small wavenumbers (i.e. the behaviour of long wavelength perturbations), replace $\sigma \to i\hat{\sigma}$ in eq. (1.6) and consider the limit $\hat{\sigma} \to 0$ and $k \to 0$ but not yet making an assumption regarding $\hat{\sigma}/k$. Then, $\alpha \approx \frac{2ik}{\hat{\sigma}}$ and the dispersion relation becomes

$$\frac{\hat{\sigma}}{k} = \frac{1+We}{2We} \frac{I_1(2k/\hat{\sigma})}{I_0(2k/\hat{\sigma})}$$

Note that real $\hat{\sigma}$ now implies growing modes. If $\hat{\sigma} = C\,k$, then the slope C of the dispersion relation is determined by the following transcendental relation

$$C = \frac{1+We}{2We} \frac{I_1(2/C)}{I_0(2/C)}$$

If one further assumes $C \gg 1$, or $\sigma \gg k$, i.e. a case where growth rate is finite at small axial wavenumber, then the above expression gives

$$C = \sqrt{\frac{1+We}{2We}}$$

which can only be large if $We \ll 1$. Replacing C with $\hat{\sigma}/k$, we get

$$\hat{\sigma} = k\sqrt{\frac{1}{2We}}$$

Rescaling $\hat{\sigma}$ with $\sqrt{\gamma k^3/\rho}$ instead of Ω gives $\hat{\sigma} = k/\sqrt{2}$ which is the Rayleigh-Plateau limit.

We therefore have the growth rate for long wavelength perturbations of slowly rotating columns as

$$\hat{\sigma} = \frac{ik}{\sqrt{2We}}$$

Effect of viscosity

The stability criterion remains unchanged for the viscous column under axisymmetric perturbations. This is due to the marginally stable state being that of a rigid rotation. It therefore follows that viscosity cannot change the stability criteria of the system, as there would be no viscous stresses acting on a rigidly rotating column. Thus, for the case of axisymmetric perturbations, the viscous stability criterion is identical to the inviscid case, namely $We < k^2 - 1$. Although the range of unstable wavenumbers doesn't change, viscosity alters the maximum growth rate and the most unstable wavenumber for a given We. This was explored by Weidman and Kubitschik [7].

1.3.2 Planar Perturbations

In this section we analyze the response of a rotating liquid column to two-dimensional or planar perturbations. Physically, this case involves investigation of a wave, that deforms the originally circular cross section into an n-lobed configuration, running along along the azimuth of the cylindrical liquid column. All cross-sections of the column deform in an identical manner so that there is no variation of system properties along the axis of the column. The Fourier mode ansatz for this case becomes $q = \hat{q}(r)e^{i(n\theta - \sigma t)}$ where n is the integer-valued azimuthal wavenumber.

Before proceeding on to the analysis for the rotating column, we look at the non-rotating (Rayleigh-Plateau), in which case, such perturbations always increase the surface area of the column and surface tension, therefore, acts as a restoring force. Thus, in contrast to axisymmetric perturbations, planar perturbations are always neutrally stable in the inviscid limit regardless of n. The dispersion relation for planar perturbations is given by

$$\sigma^2 = n(n^2 - 1) \tag{1.9}$$

implying that σ is real for all $n > 1$ (note that $n = 1$ is a degenerate case, corresponding to a mere translation of the circular core, so there is no restoring force and $\sigma = 0$). For $n \gg 1$, eq. 1.9 can be approximated as $\sigma = n^{3/2}$ which is along expected lines since these are short-wavelength capillary waves propagating along the azimuth.

The linear stability analysis for a rotating liquid column subject to planar perturbation was first performed by Hocking and Michael[5] in 1959. The authors obtained the following dispersion relation

$$(\sigma - (n-1))^2 = \frac{n(n^2-1)}{We} - (n-1) \tag{1.10}$$

In contrast to the axisymmetric case, the dispersion relation is an algebraic (quadratic) one, and leads to the following pair of eigenvalues:

$$\sigma = n - 1 \pm \sqrt{\frac{n-1}{We}(n(n+1) - We)} \tag{1.11}$$

Eq. (1.11) immediately yields the stability criterion for planar perturbations, since the eigenvalues remain real iff

$$We < n(n+1) \tag{1.12}$$

The system therefore becomes inviscidly unstable if We becomes greater than $n(n+1)$. If We is below the threshold, the system exhibits two neutral modes which physically manifest as two rotation-modified capillary waves propagating along the azimuth with frequencies given by eq. (1.11). If the We is small, the frequencies reduce to

$$\sigma = \pm\sqrt{n(n+1)}$$

which, as already seen, is the relation for the non-rotating column. For a finite rotation rate of the liquid column, one obtains two waves traveling at the speed σ/n. One of these is faster than $n-1$ and the other is slower by the same amount. Note that $\sigma = n - 1$ is the planar mode frequency for the Rankine vortex obtained by Kelvin [18]. At the stability threshold, both waves travel at the same angular speed, that of the 2D Kelvin mode referred to above. Above the threshold, the waves continue to travel at the same speed but with the amplitude of one mode growing and the other decaying with time.

If $We \to \infty$, the eigenvalues reduce to $\sigma = n - 1 \pm i\sqrt{n-1}$ which is the limiting value of the growth/decay rates of the two modes. We therefore have a pair of modes growing /decaying with (dimensional) rates proportional to Ω, as expected in an inertially dominated regime.

Effect of viscosity

Viscosity has a qualitative effect on the stability of the rotating column under planar perturbations. This was first explored by Hocking [4] in 1960 where he gave the viscous stability criterion as

$$We < n^2 - 1 \tag{1.13}$$

There are two remarkable properties of equation (1.13). Firstly, we note that the viscous threshold for instability is less than the inviscid threshold. Viscosity, therefore, hastens the onset of instability. Secondly, the viscous criterion does not contain the Reynolds number (Re). The criteria (1.13), therefore, holds as long as there is any finite non-zero viscosity in the system, but not if the viscosity is exactly zero. These observations warrant a deeper analysis of the viscous case; as will be seen next, the resulting insight will aid in our understanding of helical perturbations.

The transcendental dispersion relation for the viscous case as obtained by Hocking [4] is

$$\left(\alpha^2 - 2n + \frac{2\alpha J_n'(\alpha)}{J_n(\alpha)}\right)\left(\alpha^4 - 2n\left(n^2-1\right)\alpha^2 + 2iRe\alpha^2 + \Lambda Re^2\right) + 2n(n-1)^2\alpha^4 = 0 \tag{1.14}$$

where $\alpha^2 = iRe(\sigma - n)$ and $\Lambda = \frac{n(n^2-1)}{We} - n$. If one takes the limit $Re \to \infty$, retaining only the terms of $O(Re^3)$ in 1.14, the relation reduces to the following algebraic one

$$\alpha^4 + 2iRe\alpha^2 + \Lambda Re^2 = 0 \tag{1.15}$$

which amounts to a neglect of the infinity of modes that continue to decay at viscous rates as $Re \to \infty$. The above equation can be directly solved for α^2. We get

$$\alpha^2 = -iRe \pm iRe\sqrt{1+\Lambda} \tag{1.16}$$

$$\Rightarrow \sigma = n - 1 \pm \sqrt{\frac{n-1}{We}(n(n+1) - We)} \tag{1.17}$$

and thus recover the inviscid eigenvalues and inviscid criteria for stability. Hocking further obtains the leading order viscous correction to the inviscid eigenvalues via a regular perturbation procedure [4]. Letting $\alpha^2 = \alpha_1^2(1+\varepsilon)$, where $\alpha_1^2 = -iRe \pm iRe\sqrt{1+\Lambda}$ is the inviscid root and $\varepsilon(\ll 1)$ is the viscous correction and substituting this in the viscous dispersion

relation (eq. 1.14) yields

$$\varepsilon = \frac{\mp 2in(n-1)}{Re\sqrt{1+\Lambda}} \tag{1.18}$$

$$\Rightarrow \sigma = n-1 \pm \sqrt{1+\Lambda} \mp \frac{2in(n-1)(-1\pm\sqrt{1+\Lambda})}{Re\sqrt{1+\Lambda}} \tag{1.19}$$

If one considers the root

$$\sigma = n-1+\sqrt{1+\Lambda} - \frac{2in(n-1)(-1+\sqrt{1+\Lambda})}{Re\sqrt{1+\Lambda}} \tag{1.20}$$

the imaginary part is positive if

$$\begin{aligned} &-1+\sqrt{1+\Lambda} < 0 \\ \Rightarrow &1+\Lambda < 1 \\ \Rightarrow &\Lambda < 0 \\ \Rightarrow &We > n^2-1 \end{aligned}$$

which is the viscous criterion for instability, and differs from the inviscid criterion by order unity. From the viscous dispersion relation, one may obtain the growth rate as a function of *We*. This has been plotted in fig. 1.6 for various values of *Re*. It can be seen that, for small viscosity (large *Re*), the system is destabilized at $We = n^2-1$ and there exists only an asymptotically small growth rate in the interval $n^2-1 < We < n(n+1)$. In this interval the growth rate exhibits a non-monotonic dependence on *Re*. Thus, at a fixed *We*, the growth rate initially increases as *Re* increases from zero, and then starts to decay as *Re* becomes asymptotically large.

It is therefore clear that rotational inertia can destabilize a viscous column at a lower threshold ($We = n^2-1$) than the inviscid column ($We = n(n+1)$). Note that the correction to the inviscid eigenvalues blows up when $\Lambda \to -1$ or $We \to n(n+1)$ which is precisely the inviscid threshold. This divergence is an artifact of the regular perturbation expansion used by Hocking, and is suggestive of a different scaling with *Re* of the viscous growth rate. In order to recover the growth rate close to $\Lambda = -1$, rewrite the viscous dispersion relation as

$$\alpha^4 + 2iRe\,\alpha^2 + \Lambda Re^2 = \frac{-2n(n-1)\alpha^4}{\alpha^2 - 2n + 2\alpha\frac{J_n'(\alpha)}{J_n(\alpha)}} + 2n(n^2-1)\alpha^2 \tag{1.21}$$

Here, LHS is precisely the inviscid dispersion relation and therefore vanishes for $\Lambda = -1$ if $\sigma = n-1$. Setting $\alpha^2 = iRe(\sigma - n)$ and considering only the leading order terms in *Re*, the

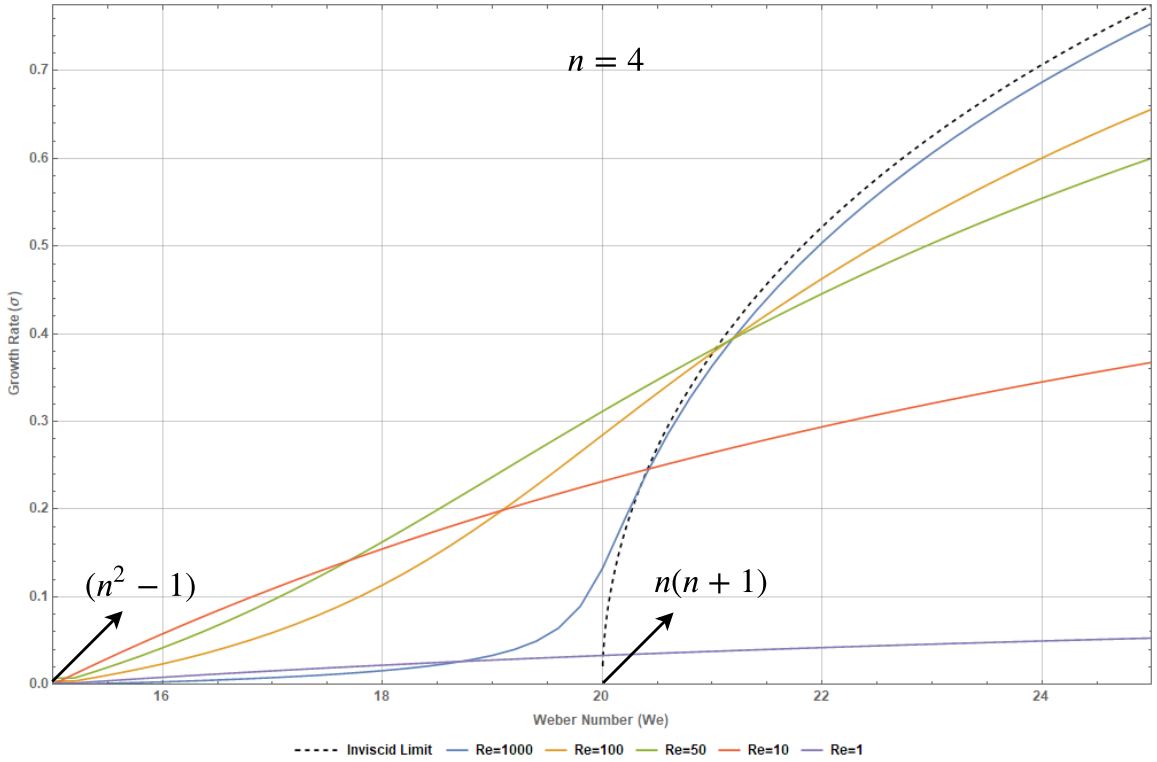

Fig. 1.6 Growth rate vs We for various values of Re with $n = 4$. Introduction of a small viscosity changes the stability criteria discontinuously from $We = 20$, for the inviscid case, to $We = 15$. However, we also see that the growth rate for large Re in the interval $15 < We < 20$ are small compared to those beyond $We = 20$. Also note that the growth rates in this interval initially increase with increasing viscous effects (decreasing Re) and decrease later. The scaling of growth rate with Re is shown in fig. 1.7.

above equation reduces as follows

$$-(\sigma - n)^2 - 2(\sigma - n) + \Lambda = \frac{2n(n-1)^2(\sigma - n)}{i\,Re} + \frac{2\,i\,n(n^2-1)(\sigma - n)}{Re} \tag{1.22}$$

Assume $\sigma = n - 1 + \sigma_r' + i\sigma_i'$ and substitute on the LHS of the above equation. Since RHS is finite at $\sigma = n - 1$, the equation results in

$$\sigma_i' = \sqrt{\frac{2n(n-1)}{Re}} \tag{1.23}$$

which is the growth rate close to $We = n(n+1)$. Fig (1.7) shows the variation in growth rate with Re for $n^2 - 1 < We < n(n+1)$. Note that the growth rate close to $We = n(n+1)$ is $O(1/Re^{1/2})$ as opposed to the $O(1/Re)$ growth rate for $n^2 - 1 < We < n(n+1)$. For large Re, the growth rate in this intermediate region can be made arbitrarily small as Re increases

but close to $We = n(n+1)$, the growth rate is always much larger. For $We > n(n+1)$, the growth rate is an O(1) quantity.

The physical reason for the discontinuous change in the stability criterion, due to viscosity, may be seen via the pressure and displacement eigenfunctions. For $n^2 - 1 < We < n(n+1)$, the phase difference between the pressure and displacement waves is exactly π for the inviscid case. Addition of viscosity alters this phase difference so that the pressure wave is not exactly out of phase with the displacement wave and therefore acts to amplify the displacement. Fig. (1.8) illustrates this.

1.3.3 Three-dimensional Perturbations

As before, we first look at the stationary column under three-dimensional perturbations. The inviscid dispersion relation for this configuration is

$$\sigma^2 = k\frac{I_n'(k)}{I_n(k)}\left(k^2 + n^2 - 1\right) \tag{1.24}$$

As for planar perturbations, 1.24 shows the column to be stable for all k provided $n \geq 1$. Thus, the stationary column is stable to all non-axisymmetric perturbations.

The effect of adding rotation to the liquid column is well understood only in the presence of viscosity. As shown first by Gillis and Kaufman [3], the necessary and sufficient criterion for the stability of the rotating column in the presence of viscosity is then given by

$$We < k^2 + n^2 - 1 \tag{1.25}$$

It is easily seen that 1.25 reduces to the corresponding criteria for viscous planar and axisymmetric perturbations for $n = 0$ and $k = 0$ respectively. For the inviscid case, however, this criterion has only been shown to be a sufficient one [12], pointing to the possible non-trivial relation between the inviscid and viscous stability scenarios. The primary contribution of the remaining part of this chapter is to clarify this relation, which then points towards the nature of the necessary and sufficient criterion for inviscid stability. As will be seen, the viscous-inviscid relation indeed turns out to be non-trivial even for this seemingly simple problem.

The dispersion relation for the inviscid rotating column has, in fact, already been given by Weidman et al [20] as

$$\alpha\frac{J_{n-1}(\alpha)}{J_n(\alpha)} - \frac{We\left(4 - \hat{\sigma}^2\right)}{We + 1 - n^2 - k^2} - n\left(1 + \frac{2}{\hat{\sigma}}\right) = 0 \tag{1.26}$$

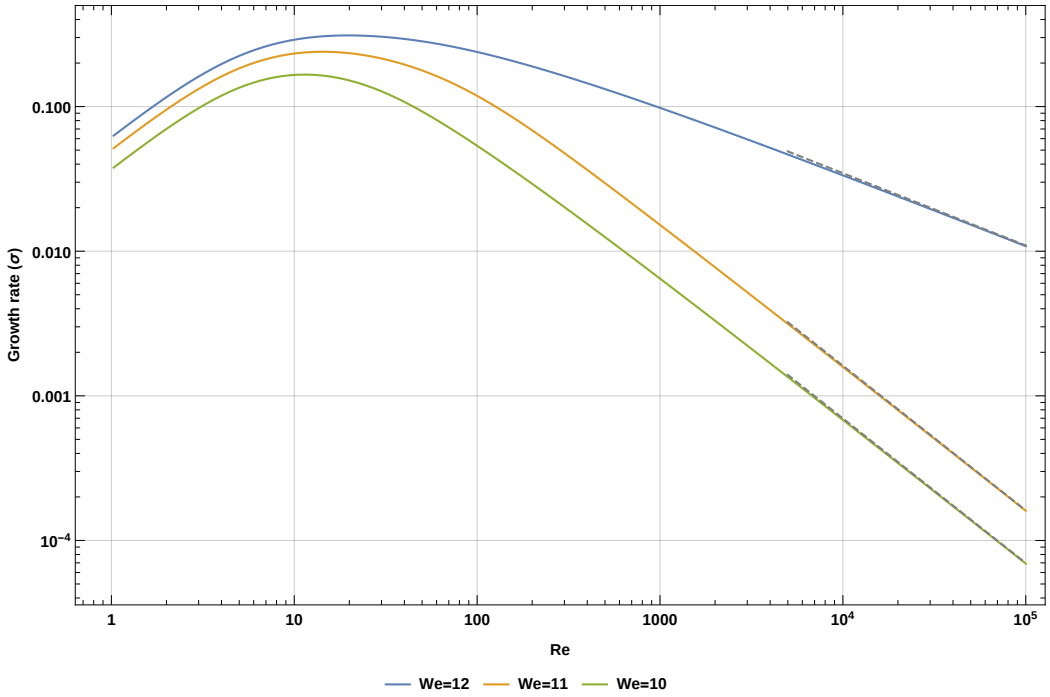

(a) $n = 3$

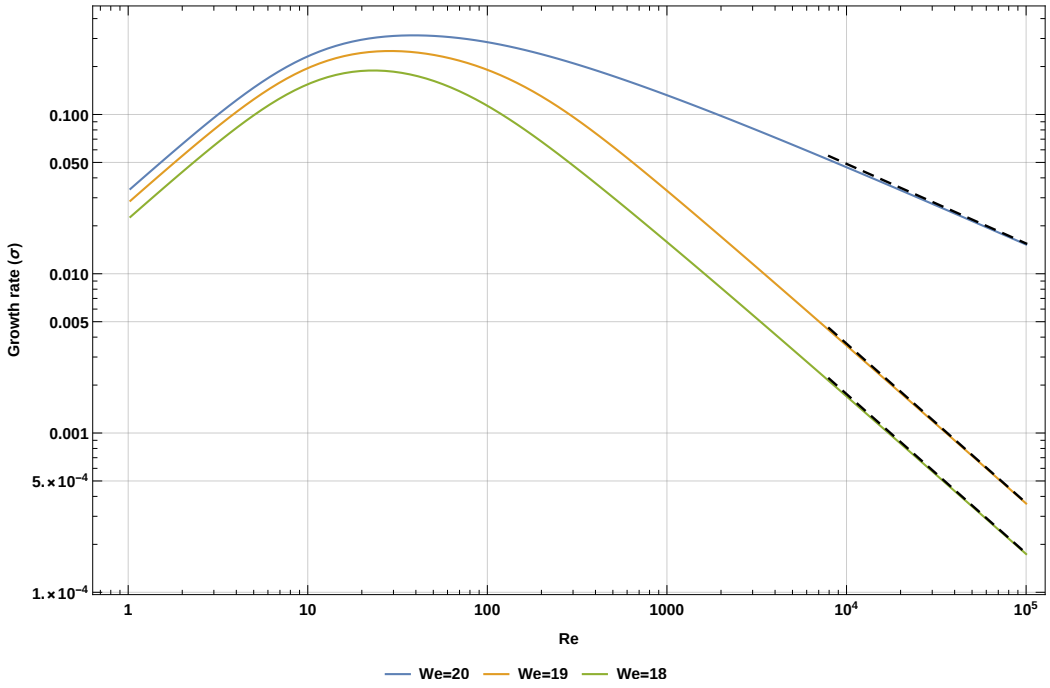

(b) $n = 4$

Fig. 1.7 Variation of growth rates with *Re*. The solid lines denote numerically obtained values from the dispersion relation. The dotted lines indicate the large *Re* asymptotes from eq. 1.19 and eq. 1.23

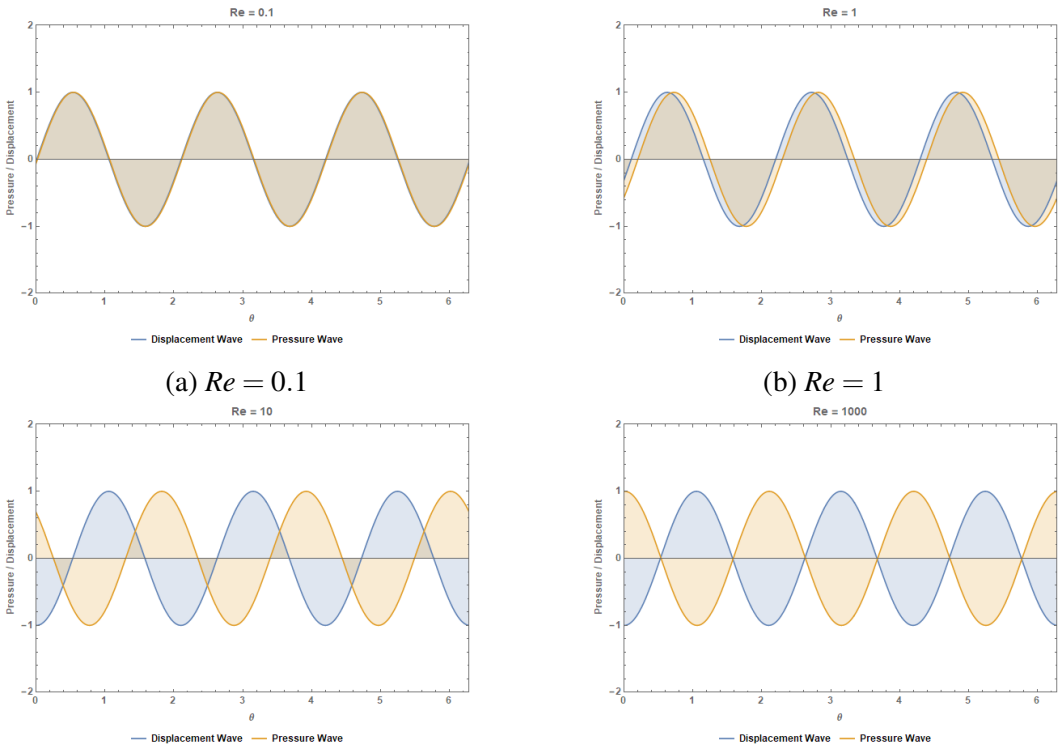

(a) $Re = 0.1$ (b) $Re = 1$

(c) $Re = 10$ (d) $Re = 1000$

Fig. 1.8 Variation of phase difference between displacement and perturbation pressure with Re. For large Re, the two are exactly out of phase, thus delaying the onset of instability.

where $\alpha = k\sqrt{\frac{4}{\hat{\sigma}^2} - 1}$. It can be verified that setting $n = 0$ leads us back to the axisymmetric relation by Hocking (eq.1.6). In eq. 1.26 $\hat{\sigma}$ is the Doppler frequency of the perturbation, i.e. it gives the angular velocity of the perturbation $(\hat{\sigma}/n)$ with respect to the column. It relates to the original frequency σ via the relation $\hat{\sigma} = \sigma - n$.

In order to analyze the solutions of 1.26, we fix We and use a root finding algorithm to search for the roots $(\hat{\sigma})$ while varying k. The character of dispersion curves thus generated varies based on the We. The figures that follow (fig. 1.9) delineate the We-intervals corresponding to differing nature of the dispersion curves. For the three-dimensional perturbations under consideration, the dispersion curves are functions of We, k and n, and the figures therefore show the dispersion curves as a function of k for a fixed We and n. There are four We-intervals, and an identification of the dispersion curve structure in each of these intervals is crucial to understanding the stability criterion for the rotating column.

The first regime, $We < n^2 - 1$, corresponds to the scenario where the rotating column is stable regardless of viscosity. Fig. 1.9a shows the two capillary modes (orange) and the first few of the infinite hierarchy of Coriolis modes. All of these modes are, of course, neutral owing to the column being stable (as mentioned above). There are no unstable modes in

this regime. As We is increased, the two capillary branches move toward $\sigma = n-1$ on the $k = 0$ axis (this can be verified from eq. 1.11). In particular, increasing We causes the upper capillary branch to move downward and therefore intersect the Coriolis modes.

The second regime, $n^2 - 1 < We < n(n+1)$, is where, as already seen, the column is unstable only in the presence of viscosity, but stable in the inviscid approximation. As shown in fig. 1.9b, the upper capillary branch has moved below the line corresponding to zero Doppler frequency ($\sigma = n$ or $\hat{\sigma} = 0$) leading to a coalescence of the capillary branch with a Coriolis branch at $k = k_1 = 0.6$. This coalescence is accompanied by the pair of eigenvalues becoming complex-valued for larger k, implying that the column transitions to instability. Thus, the interval of instability for this regime is given by $k_1 < k < \sqrt{We - n^2 + 1}$.

The third regime includes the interval $n(n+1) < We < We_{cusp}$ where We_{cusp} is the We corresponding to the tip of the shaded region - *the cusp*, in the $k - We$ plane (for $n = 3$, $We_{cusp} \approx 18$ as shown in fig. 1.12c). The shaded regions in fig. 1.12 represent regions where the system continues to be inviscidly stable but unstable in the presence of viscosity. The dispersion curves in this regime undergo two coalescences (at $k_1 = 0.97$ and $k_2 = 0.53$), such that the concerned branch of the dispersion curve now exhibits a fold for $k_2 < k < k_1$ (fig. 1.9c). This range of axial wavenumbers between the two coalescences is stable and the unstable intervals become $0 < k < k_2$ and $k_1 < k < \sqrt{We - n^2 + 1}$.

Finally, as We is increased beyond We_{cusp}, the dispersion curve gradually unfolds so that the unstable region is now given by $0 < k < \sqrt{We - n^2 + 1}$ (fig. 1.9d). This general pattern of the behaviour of dispersion curves holds for all azimuthal wavenumbers (n). Fig. 1.10 shows the aforementioned behavior repeating for $n = 4$.

The dispersion curves may be stacked upon one another, along the We-axis, so as to demarcate the regions of stability of the liquid column in the $(k - We)$ space for each n. Fig. (1.11) shows schematically how this may be achieved. Projection of the folding points of the dispersion curve onto the $k - We$ plane yields the cusp-shaped region in the $k - We$ plane. The top branch of the cusp is generated from the projection of the bifurcation point at higher k, while the bifurcation point at lower k gives the lower branch. The resulting regions for stability in the (k, We) parameter space for $n = 2, 3, 4$ and 10 are given below (fig. 1.12). For $n = 1$, however, the picture is different (fig. 1.12a) in that the stable island now extends to infinity along the We-axis; this singular behavior is not entirely unexpected owing to the degenerate character of the n =1 perturbation in the limit $k \to 0$. These results are consistent with the observations of Weidman et al [20], who obtained the growth rates for $n = 1, 2$ and 3 but only for $We = 10$, missing out on the effect of We on the modes and therefore also on the stability criteria. In this work, we have generalized their results for all n and We, identified a

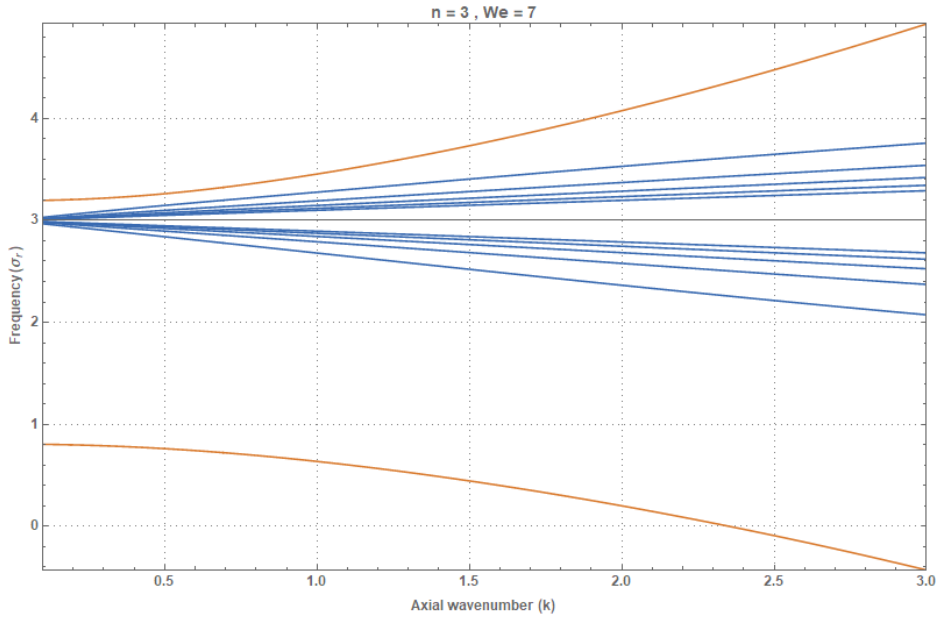

(a) Frequency(ω) vs Axial Wavenumber(k) for Regime-I: $We < n^2 - 1$. Only neutral modes exist for all k. Coriolis force driven modes shown in blue and surface tension driven capillary modes in orange.

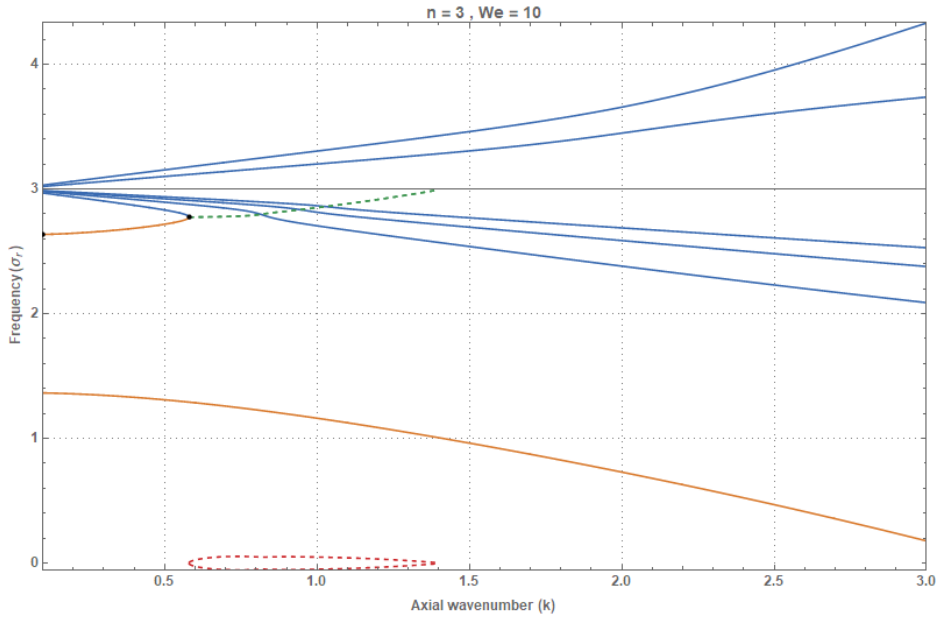

(b) Regime-II: $n^2 - 1 < We < n(n+1)$. System is stable for a range of axial wavenumbers starting from zero followed by an unstable region. It can be seen that a surface tension driven mode(orange) interacts with a Coriolis mode(blue) resulting in imaginary eigenvalues (green - real part, red - imaginary part) and hence unstable modes.

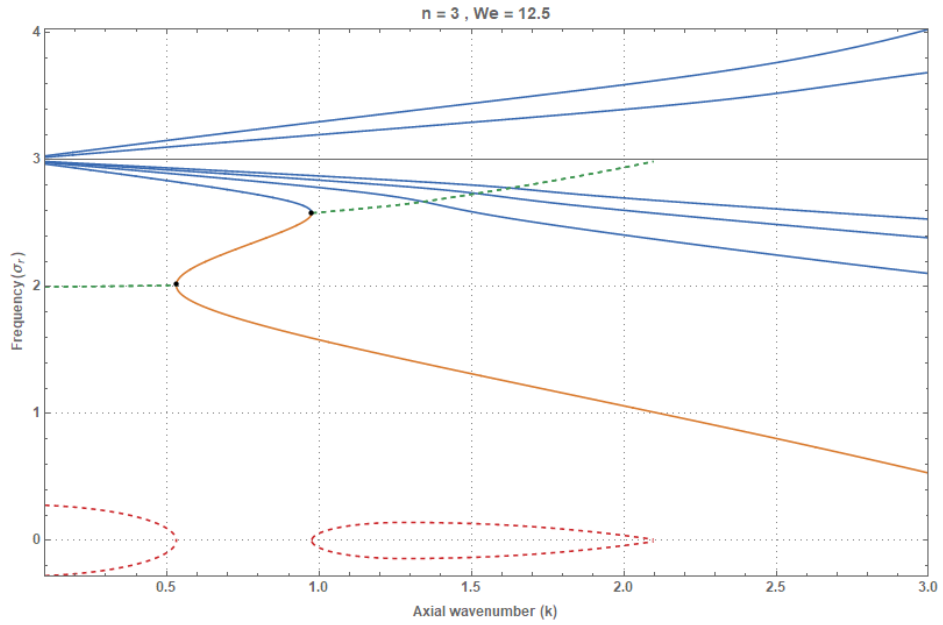

(c) Regime-III: $n(n+1) < We < We_{cusp}$. Here, two bifurcations can be seen - the first where two complex eigenvalues (unstable modes) coalesce resulting in two real eigenvalues and the second where one of the emerging eigenvalue interacts with another real eigenvalue to yield two complex eigenvalues.

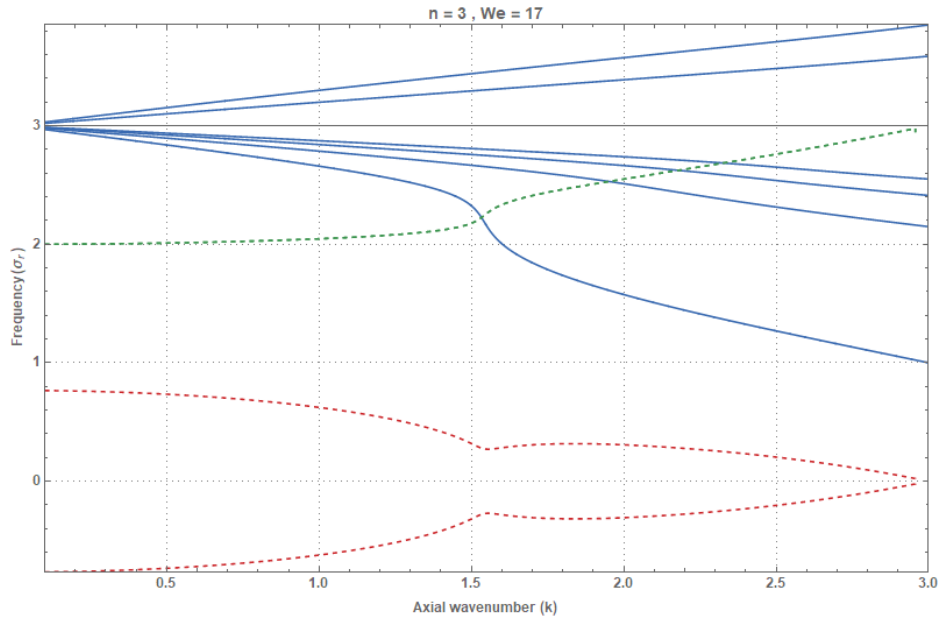

(d) Regime-IV: $We > We_{cusp}$. The 'S' shaped region straightens out and the associated bifurcations no longer occur.

Fig. 1.9 Variation of dispersion curves across the four stability regimes for $n = 3$.

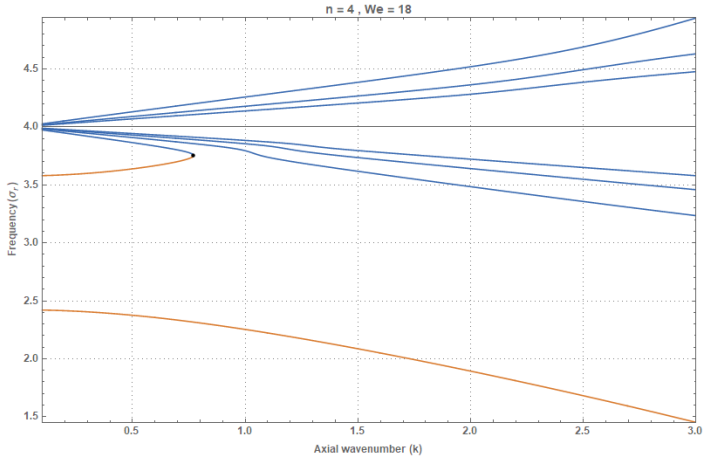

(a) $We = 18$

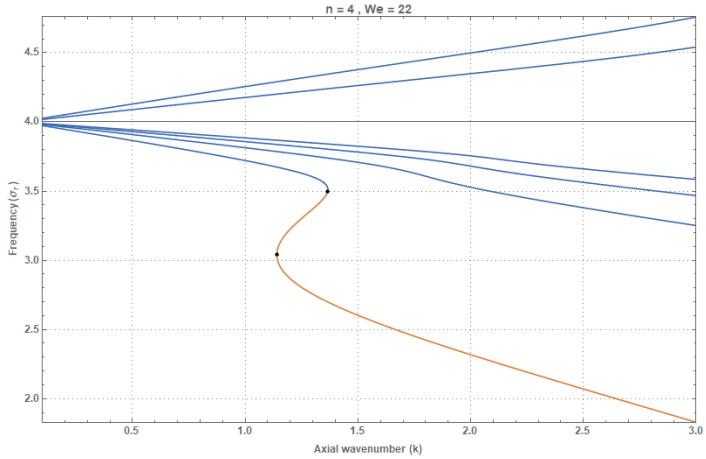

(b) $We = 22$

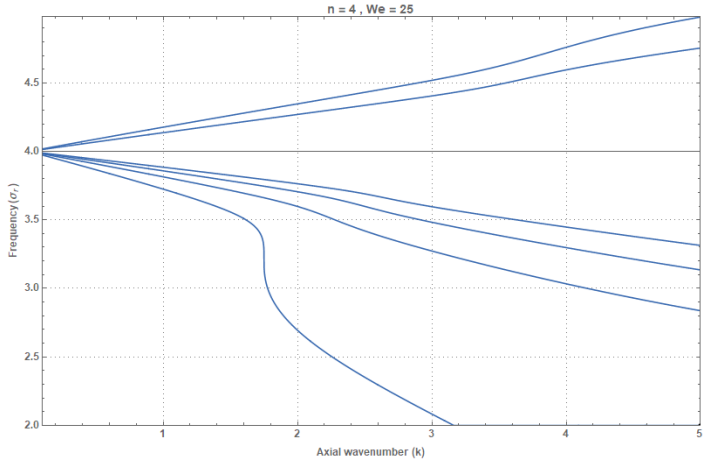

(c) $We = 25$

Fig. 1.10 Variation of dispersion curves (σ vs k) across different We regimes for $n = 4$. (a)$n^2 - 1 < We < n(n+1)$, (b) $n(n+1) < We < We_{cusp}$ and (c) $We > We_{cusp}$.

new mechanism of instability in inviscid rotating columns and provided the necessary and sufficient criteria for stability of such columns under three-dimensional perturbations.

If one further probes the region close to $We = n^2 - 1$, a curious property of the dispersion curves is observed. It turns out that other retrograde branches of the dispersion curves also result in cusps for We sufficiently close to $n^2 - 1$. Fig. 1.14 and Fig. 1.15 show this behaviour for $n = 3$. Thus, during the course of the upper capillary branch moving downward, it crosses an infinite number of Coriolis branches, for sufficiently small k, as We crosses $n^2 - 1$. Each of these crossings leads to a coalescence event between the capillary branch and one of the Coriolis branches, with a transition to instability. This then leads to a stable island generated, with there appearing to be a one-to-one correspondence between the island and the particular Coriolis branch that coalesces with the capillary one. The number of stable islands must rapidly increase as We approaches $n^2 - 1$ from above, and correspondingly, the coalescences occur at progressively smaller k. Thus, in the inviscid scenario, there appears to be an infinite hierarchy of stable islands, enclosed within the viscously unstable region given by $We > n^2 + k^2 - 1$, which decrease in spatial extent rapidly, eventually asymptoting to the limit point $(We, k) = (n^2 - 1, 0)$.

Studying a strictly inviscid system may seem artificial since any real system will have a finite viscosity and therefore these results for stability will not hold. However, the regions of stability obtained for the inviscid column continue to bear a significance for viscous columns as well. While it is true that a viscous column is unstable regardless of the state being inside or outside the island (as long as it satisfies $We > n^2 + k^2 - 1$), the growth rate within these islands is expected to be small. We recall from Fig. (1.6) and Fig. (1.7) that growth rate is $O(1)$ if $We > n(n+1)$ and proportional to $1/Re$ if $n^2 - 1 < We < n(n+1)$. These two regimes represent regions outside and inside the island, respectively, in the planar case. Therefore, even in the three-dimensional case, the growth-rate inside the island will vary as $1/Re$ and remain $O(1)$ outside it. For liquid columns with large Re, we will then have a growth rate variation as seen for the $Re = 1000$ case in Fig. (1.6). It then follows that, for We close to (but larger than) $n^2 - 1$, the long-time growth rate exhibited by a weakly viscous system will oscillate rapidly, as a function of k; the oscillations are between order unity growth rates attained between islands and the asymptotically small viscous growth rates attained within the islands.

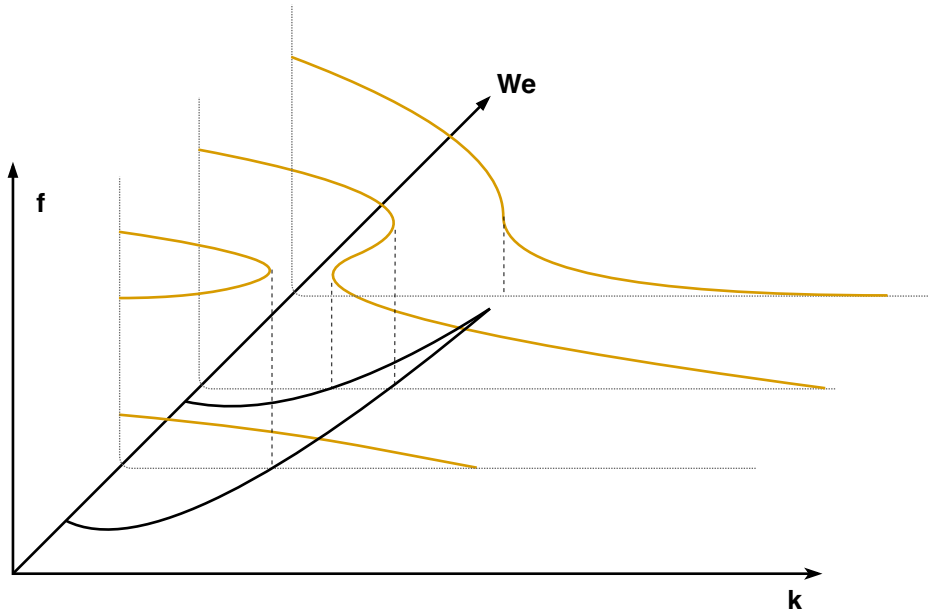

(a) A schematic showing that the projections of the folding points of the dispersion curve onto the $k - We$ plane yields the region of stability for the system.

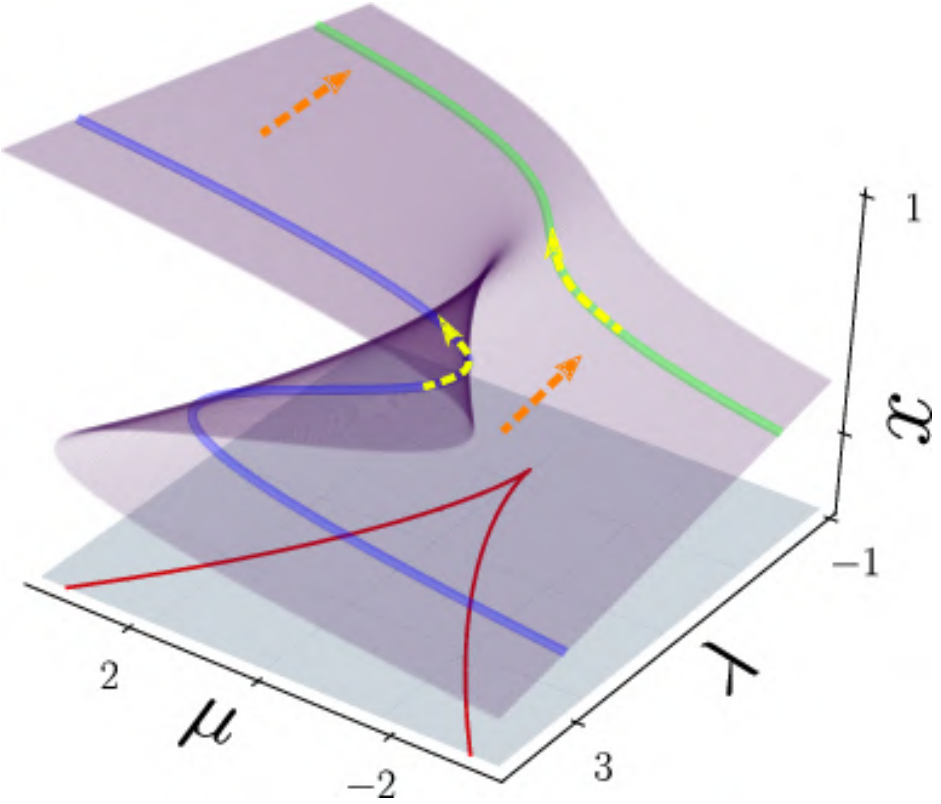

(b) An illustration of the cusp catastrophe. The purple and green curves represent two of the three orange curves shown in (a).

Fig. 1.11 Generation of the cusp from the dispersion curves.

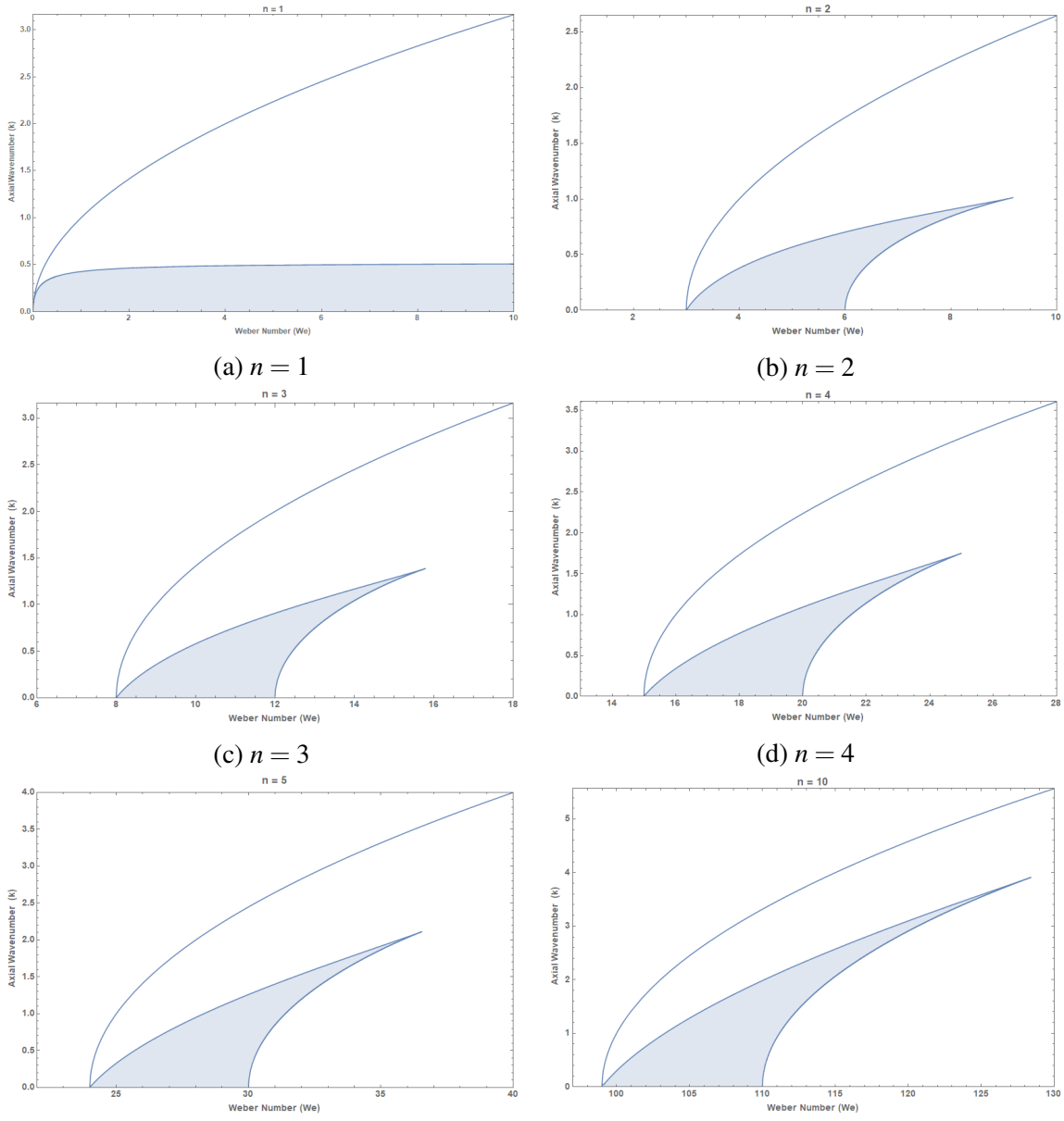

(a) $n = 1$ (b) $n = 2$

(c) $n = 3$ (d) $n = 4$

(e) $n = 5$ (f) $n = 10$

Fig. 1.12 Regions of stability for various n.

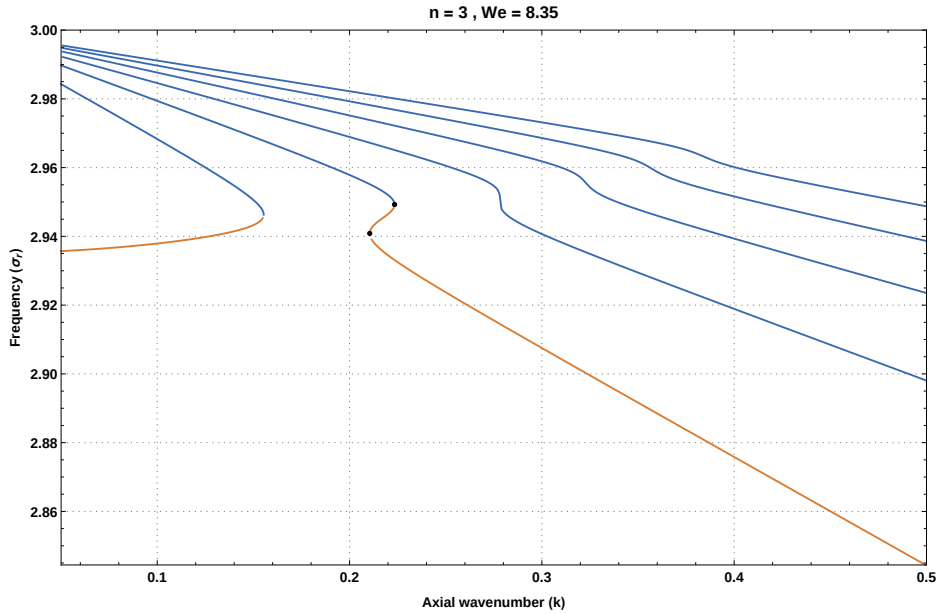

Fig. 1.13 The figure shows a second branch (besides the one illustrated earlier in Fig. 1.9) that can lead to a cusp formation in the (k, We) plane.

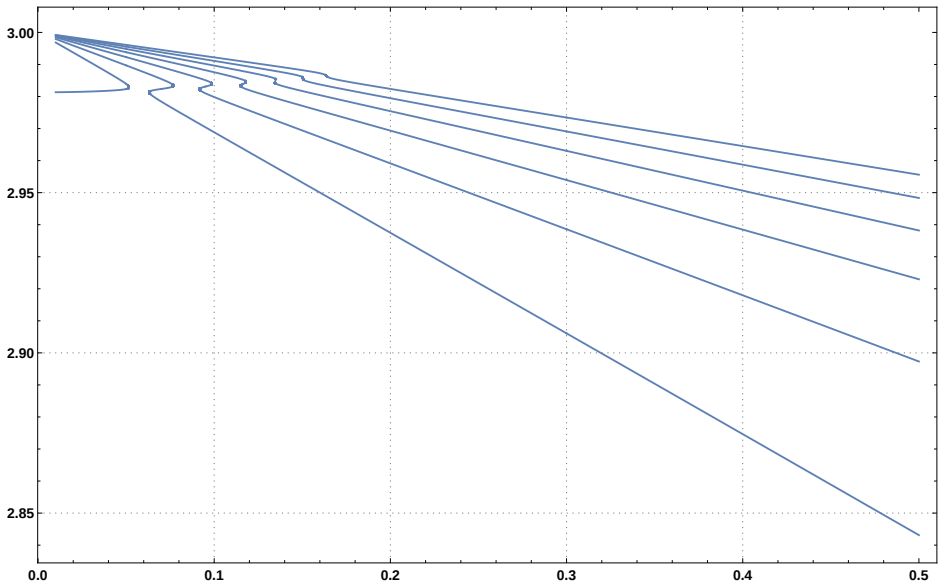

Fig. 1.14 For We sufficiently close to $n^2 - 1$, multiple dispersion curve branches lead to cusp formation causing alternate stable and unstable regions in the $(k - We)$ space. The associated $(k - We)$ space is shown in Fig. 1.15

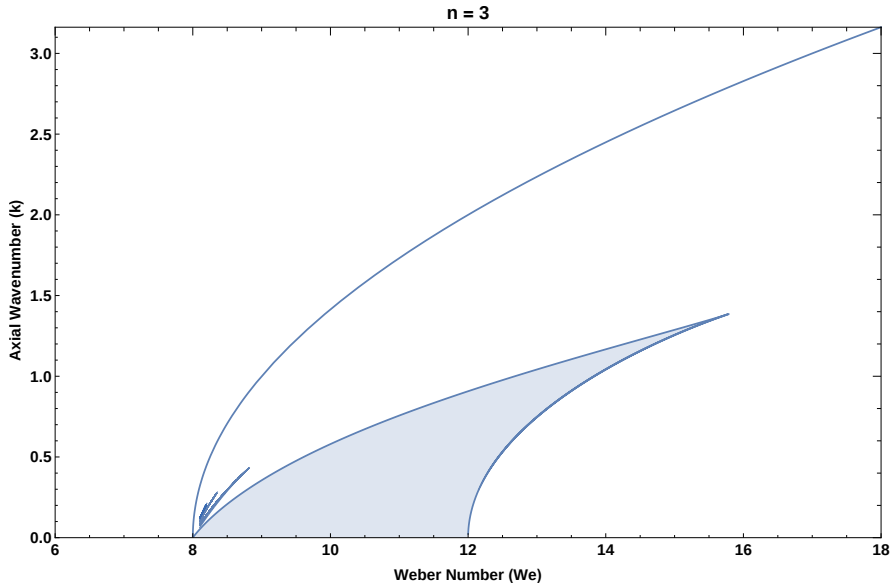

(a) Multiple cusps

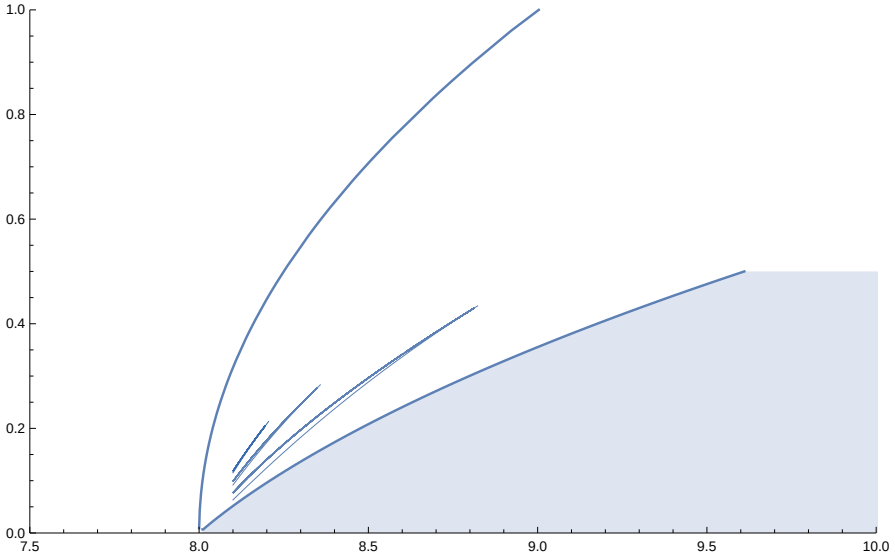

(b) Multiple cusps (close up view)

Fig. 1.15 Sufficiently close to $We = n^2 - 1$, there exist multiple (possibly infinite) number of alternating stable and unstable regions in the parameter space.

Chapter 2

Stability Of Rotating Liquid Columns With An Embedded Air Core

2.1 Introduction

In this chapter we discuss the stability of a vortex column with an embedded air core. This study is motivated by a series of experiments conducted bv Jha and Govardhan [6] which suggest the possibility of a new mechanism for instability in two phase vortex rings (2.1). Two phase vortex ring here refers to a vortex ring with an encapsulated air bubble. As mentioned by the authors, an understanding of the interactions of vortical structures with air bubbles is of fundamental importance to studying two phase turbulence and has industrial applications such as drag reduction in ships via bubble injection into the stream. In order to understand such an interaction the authors study an idealization of vortical-structure-air-bubble interaction and thus consider the interaction of the single air bubble with a vortex ring. They observe a sequence of events involving the entrainment of bubble into the ring, the elongation of the bubble to a nearly toroidal shape and finally the destabilization of the ring along with bubble break up, indicating a possible instability in the configuration. This work is aimed towards investigation of such an instability.

In order to address the involved scenario of a vortex-ring-bubble interaction, we begin first with a classical case, that of a non-rotating liquid annulus with an embedded air core, followed by the case where the liquid annulus is in rigid-body rotation. Next, we analyze the stability of a configuration with an additional irrotational (azimuthal) flow in the exterior, that is, of a Rankine vortex with a concentrically embedded air core, and finaly consider the effects of the self-induced straining field of the ring.

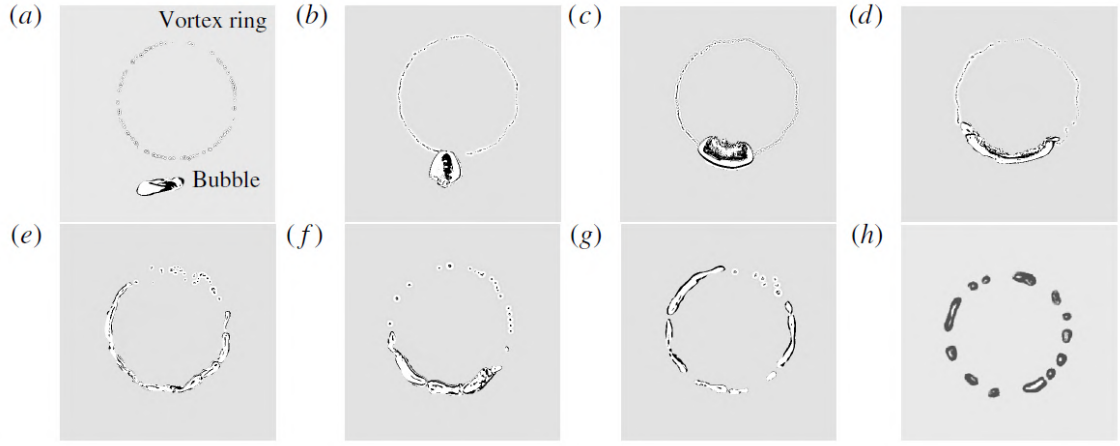

Fig. 2.1 Sequence of events as a bubble is entrained into the vortex ring and destabilizes the ring. Fig. (a) to Fig. (c) show the entrainment of the air bubble into the vortex core. Fig. (d) through (f) show the elongation of the air bubble within the ring. Note that the bubble elongates to a nearly toroidal shape and therefore allows us to model the system as a vortex *column* with an embedded air core. Fig. (g) and (h) demonstrate the breakup of the ring and the bubble due to a possible instability. Figure taken from Jha and Govardhan [6].

2.2 Air column in liquid

For the case of axisymmetric perturbations, the condition for stability of an air column surrounded by an infinite body of stationary inviscid liquid (termed the inverse Rayleigh-Plateau configuration herein) is the same as that for the regular RP instability, namely, $k < 1$. This is expected, since the stability criterion is still governed by the original quasi-static arguments of Plateau, which rely only on surface energy (area) considerations. The fact that perturbations with wavelengths longer than the circumference of the column decrease the surface area of the column is a geometric property and hence remains unaffected by which side of the interface the liquid is. However, the scaling of the growth rate of the unstable modes (σ) with k, for small wavenumbers, is in stark contrast with the linear scaling of the regular RP instability (eq. 1.3). For the inverse case, the growth rate for small k scales as $1/\log k$.

One may address the above difference in scaling behaviour by arguments involving the energy balance in the two configurations. Consider first the case of regular Rayleigh-Plateau configuration. Under axisymmetric perturbations, the average change in radius of the column is of the order $\Delta r = \varepsilon^2/a$, ε being the amplitude of the perturbation and a being the column radius. Therefore, corresponding change in the surface energy per unit wavelength is $\Delta SE = \gamma\varepsilon^2/ka$.

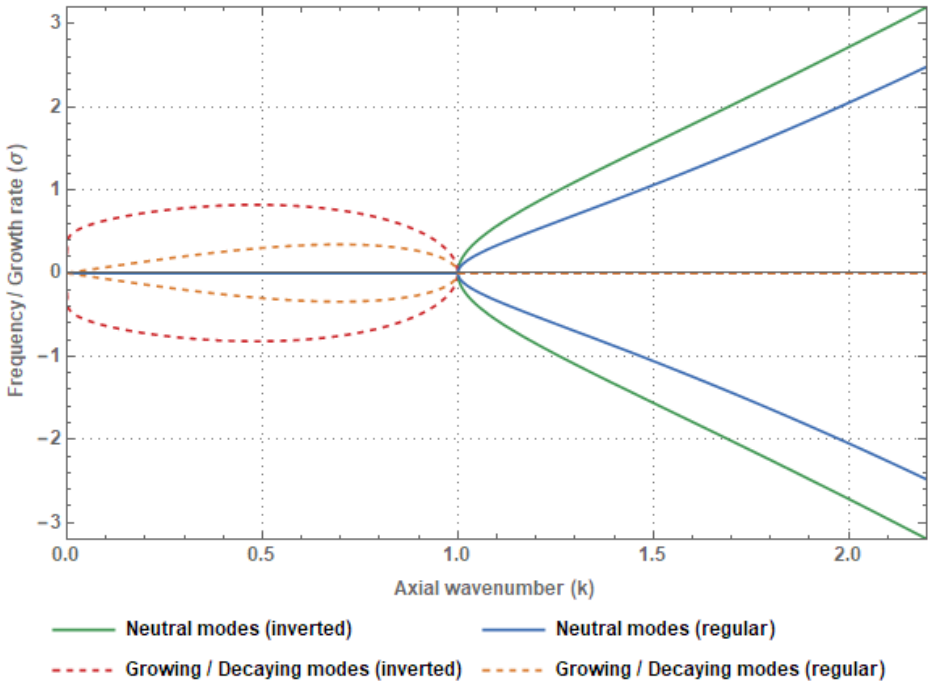

Fig. 2.2 Comparison of growing / decaying and neutral modes of liquid column in air (orange and blue) with air column in liquid (red and green).

This change in surface energy balances the perturbation kinetic energy. Assuming a long-wavelength perturbation ($k \to 0$), from the equation of continuity, one readily obtains $u_r/a \sim k\,u_z$, so that $u_r/u_z \sim O(ka) \ll 1$; that is, the radial velocity is much smaller than the axial velocity for long wavelength perturbations. Since the characteristic length scale of the perturbation (in both the radial and axial directions) is $O(k^{-1})$, and is therefore much greater than $O(a)$, the radial flow is a linear one at leading order. Since the characteristic time scale of this flow is of order the inverse growth rate, one may write

$$u_r \propto \frac{\sigma \varepsilon r}{a} \sim \sigma \varepsilon$$
$$\Rightarrow u_z \sim \frac{\sigma \varepsilon}{ka} \gg u_r$$

which are consistent with the equation of continuity and long wavelength considerations. The kinetic energy of the perturbation flow, being dominated by the axial velocity, is given by

$$KE \sim \frac{\rho a^2}{k} \frac{\sigma^2 \varepsilon^2}{k^2 a^2}$$

for a column length of order a unit wavelength. Equating this to the surface energy gives one the expression for the growth rate as

$$\begin{aligned}
&\frac{\rho a^2}{k}\frac{\sigma^2\varepsilon^2}{k^2a^2} \sim \frac{\gamma\varepsilon^2}{ka} \\
\Rightarrow &\frac{\sigma}{\sqrt{\gamma/\rho a^3}} \sim ka \\
\Rightarrow &\sigma^* \sim k^*
\end{aligned}$$

where σ^* and k^* are non-dimensionalized forms of σ and k respectively. We therefore recover the linear scaling of modes for small k for the Rayleigh-plateau instability seen in Chapter 1.

In considering the energy balance for an air column in liquid, note that the surface energy estimate of the perturbation remains the same as that for the previous case and we only need to obtain the new scaling for the perturbation kinetic energy. For the exterior flow, the radial and axial length scales are both given by the wavelength or k^{-1} (note that with the exterior liquid domain being unbounded, the linear-flow simplification for the perturbation flow is no longer valid). In the limit of long wavelengths, one may approximate the flow driven by an axisymmetric perturbation as the combination of the radial flow driven by the expanding or contracting column at a given axial station (this flow having the character of a 2D source/sink on length scales smaller than k^{-1}), and the compensatory axial flow arising from the equation of continuity. The radial flow varies as $1/r$, and since the velocity at the surface of the column is $O(\sigma.\varepsilon)$, one obtains the following estimate for radial velocity, on length scales smaller than k^{-1}

$$u_r \sim \frac{\sigma\varepsilon a}{r}$$

From the continuity equation, one has $u_z \sim u_r/ka$. The primary contribution to the perturbation kinetic energy is due to radial velocity and is given by

$$\begin{aligned}
KE &\sim \int_1^{ka} \rho\frac{\sigma^2\varepsilon^2a^2}{r^2} r\,dr\,d\theta \\
\Rightarrow KE &\sim \frac{\rho\sigma^2\varepsilon^2a^2}{k}\log(ka)
\end{aligned}$$

Finally, balancing the perturbation surface and kinetic energies yields

$$\frac{\rho\sigma^2\varepsilon^2a^2}{k}\log(ka) \sim \frac{\gamma\varepsilon^2}{ka}$$
$$\sigma^* \propto \frac{1}{\sqrt{\log(k^*)}}$$

which is the scaling for long wavelength axisymmetric perturbations of an air column surrounded by liquid. The variation of the eigenvalues with wavenumber, across the transition threshold, for both the original and inverse Rayleigh problems is shown in fig. 2.2 for both, regular and inverted configuration. The inverse logarithmic scaling above causes the dispersion curves (for the growing and decaying mode) to plummet to the origin $(\sigma,k) \equiv (0,0)$ much more precipitously than in the original Rayleigh-Plateau instability. Fig. 2.2 also shows that the growth rate of the unstable mode peaks at a longer wavelength (a smaller k, $k = 0.48$) for the inverse Rayleigh-Plateau configuration.

As for the original Rayleigh Plateau case, all perturbations other than axisymmetric ones $(n = 0)$ remain stable, with the corresponding dispersion relation being given by

$$\sigma^2 = k\frac{K_n'(k)}{K_n(k)}(k^2+n^2-1) \tag{2.1}$$

From 2.1, it is clear that σ^2 is always positive (and σ real) for $n \geq 1$.

2.3 Rotating liquid column with air-core

As a first step towards modeling the dynamics of the vortex-ring-bubble configuration in Jha and Govardhan [6], we consider the inviscid stability of an annulus of rigidly rotating liquid with a concentric air core surrounded by a rigid outer boundary (fig. 2.3).

2.3.1 Axisymmetric perturbations

Linear stability of this configuration to axisymmetric perturbations was first analyzed by Rosenthal [16]. He considered the densities of the inner and outer fluids to be ρ_1 and ρ_2 respectively, with the radii of the core and outer boundary taken to be a and b, respectively. We will denote the density ratio ρ_1/ρ_2 as ρ_r and the radius ratio a/b as ξ. Note that $\rho_r \to 0$ would represent an air column surrounded by liquid while $\rho_r \to \infty$ would indicate the liquid

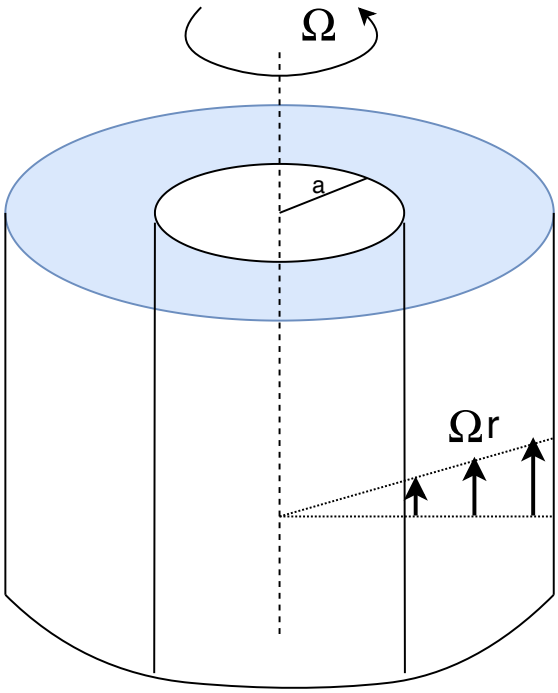

Fig. 2.3 Rotating liquid annulus with an embedded air core

column in ambient air analyzed in Chapter 1. The criterion for stability takes the form

$$k^2 + (1-\rho_r)We_2 \geq 1 \tag{2.2}$$

where k is scaled with $1/a$, $\rho_r = \rho_1/\rho_2$, and $We_2 = \frac{\rho_2 \Omega^2 a^3}{\gamma}$ is the Weber number based on the outer fluid density. The limit of no rotation ($We_2 = 0$) immediately gives $k > 1$ - the stability criterion for regular and inverted cases of the Rayleigh-Plateau instability.

Setting $\rho_r \to 0$ with finite We_2 gives the stability criterion for an annulus of liquid with an air core

$$k^2 + We \geq 1 \tag{2.3}$$

The range of unstable wavenumbers is now given by $0 < k < \sqrt{1-We}$, which is smaller than that for the case without rotation. Therefore, rotation stabilizes the system, as expected, since a stable centrifugal equilibrium would have the denser fluid at larger radial distances (as is the case with the base-state); note that this stabilization holds for any $\rho_r < 1$. Returning to the case $\rho_r = 0$, if $We > 1$, the wavenumber of the perturbation required for instability becomes imaginary and the system becomes stable to perturbations of all wavenumbers.

The dispersion relation for a system of two concentric fluids is given by

$$\frac{\left(k^2-1\right)}{We_2}+1-\rho_r=\frac{4\alpha}{k^2+\alpha^2}\frac{J_0(\alpha)}{J_1(\alpha)}\left(\rho_r+\Delta\right) \tag{2.4}$$

where

$$\Delta=\frac{\frac{Y_0(\alpha\xi)}{J_0(\alpha\xi)}-\frac{Y_1(\alpha)}{J_1(\alpha)}}{\frac{Y_1(\alpha)}{J_1(\alpha)}-\frac{Y_1(\alpha\xi)}{J_1(\alpha\xi)}} \tag{2.5}$$

$$\alpha=k\sqrt{\frac{4}{\sigma^2}-1} \tag{2.6}$$

The stability criterion derived from this dispersion relation has been metioned earlier (eq. 2.2). Several qualitative features of the neutral spectrum for this case remain identical to the single column case. For instance, the largest eigenvalues remain proportional to $k^{3/2}$ for large k indicating their being surface-tension-driven. On the other hand, the other primarily Coriolis-driven-modes are again restricted to the frequency interval $\sigma\in(-2\Omega,2\Omega)$.

2.3.2 Planar Perturbations

The case of planar perturbations was first explored by Ross [17] who obtained the dispersion relation

$$(\lambda-N)^2+\frac{Nn\left(n^2-1\right)}{(\rho_r-1)We_2}-N(n+N)=0 \tag{2.7}$$

where

$$\lambda=\sigma-n$$
$$N=\frac{1-\rho_r}{\coth\left(n\log\left(\frac{1}{\xi}\right)\right)+\rho_r}$$

As a check, we note that setting $\rho_r\to\infty$ yields the criterion for the single rotating fluid column obtained by Hocking [5].

The stability criterion arising from this dispersion relation is given by

$$We_2<\frac{1}{\rho_r-1}\left(\frac{n(n^2-1)}{n+N}\right) \tag{2.8}$$

If $\rho_r<1$, i.e. the inner fluid is lighter relative to the outer fluid, the system is stable to all perturbations. If $\rho_r>1$, the system is destabilized by rotation and the critical Weber number (We_2) for instability is as given in eq. 2.8. Specifically, we can retrieve the planar stability criteria for a column of liquid surrounded due to Hocking (eq. 1.12) if we consider the limit

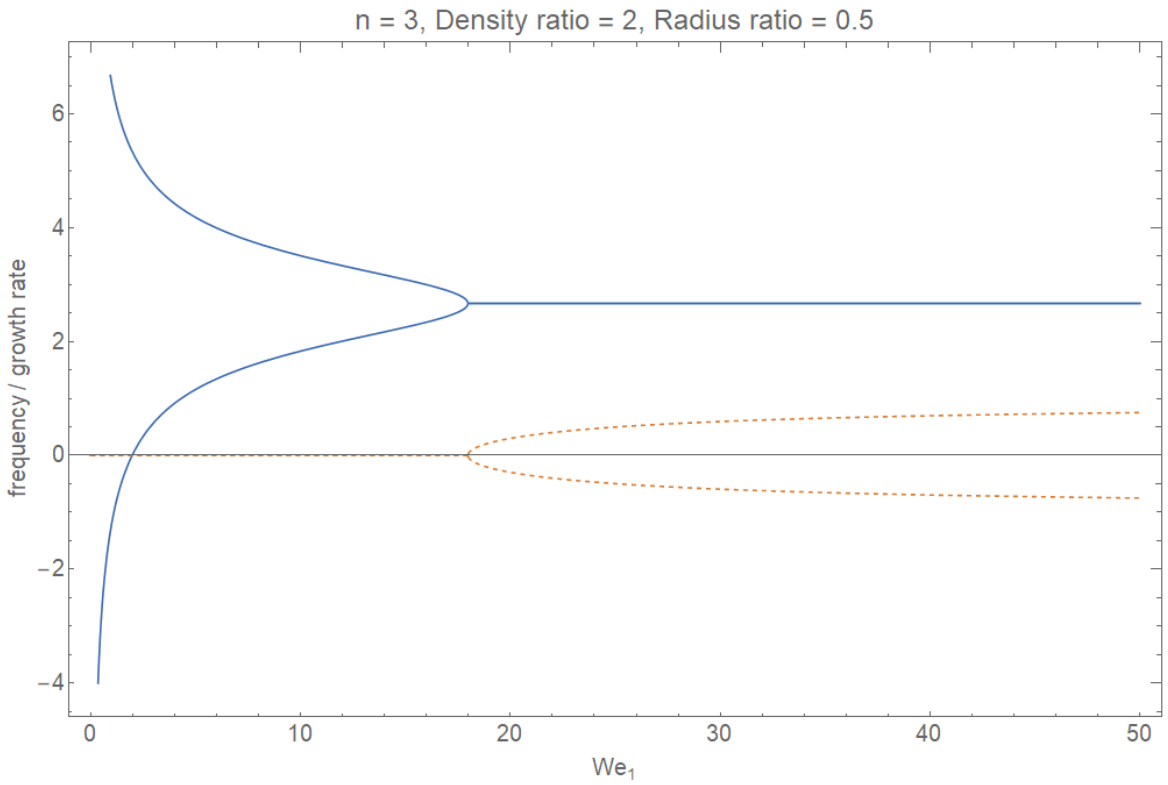

Fig. 2.4 Variation of the eigenvalues with We for planar perturbations of the rotating annulus with embedded air core. Here, $n = 3, \rho_r = 2$ and $\xi = 0.5$. The solid blue curves represent the real part and the dotted orange curves represent the imaginary parts of the two eigenvalues.

$\rho_r \to \infty$, $\xi \to \infty$ but a finite $We_2\rho_r$. In this case, $N = -1$ and eq. 2.8 reduces to

$$We_1 < n(n+1)$$

where $We_1 = \rho_1\Omega^2 a^3/\gamma$, which is the Hocking's criteria. Fig. 2.4 shows the behaviour of neutral and unstable modes of the system with We_1. Note that unstable modes would only exist if $\rho_r > 1$. In fig. 2.4, $\rho_r = 2$, indicating a heavy fluid in a lighter ambient. This is similar to the configuration analyzed in Chapter 1. Two neutral modes can be seen, one faster than the column rotation rate and the other slower. Beyond the critical We_1, one has two complex eigenvalues corresponding to a growing and a decaying mode. The real part of these modes determines the speed with which the disturbance travels along the column while the imaginary part indicates the growth / decay rate.

The two other parameters affecting the growth rate are the radius ratio ($\xi = a/b$) and the density ratio ($\rho_r = \rho_1/\rho_2$). We first look at the variation of growth rates with We_1 for different density ratios for a fixed radius ratio (fig. 2.5). If $\rho_r \to \infty$, We_1 reduces to the planar single column limit, $n(n+1)$. For any finite density ratio, the critical We_1 is greater than

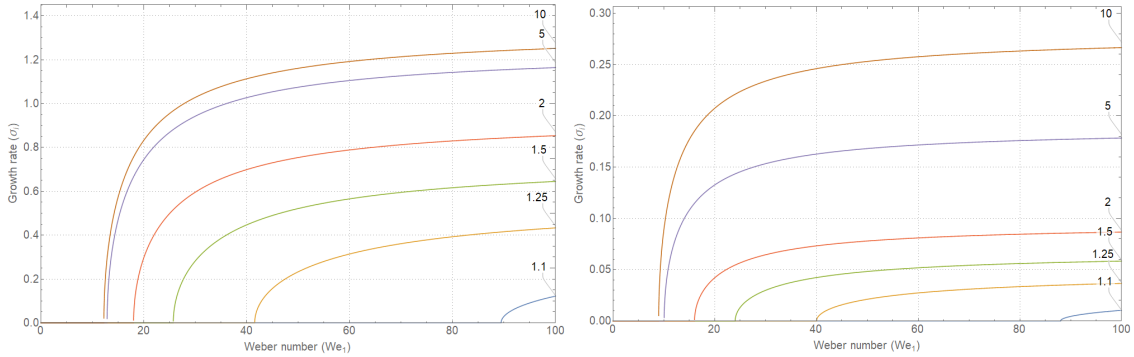

(a) Variation of growth rate with We for various density ratios at radius ratio equal to 0.1.

(b) Variation of growth rate with We for various density ratios at radius ratio equal to 0.999.

Fig. 2.5 The figures show the effect of an outer fluid on the instability of a rotating liquid column for $n = 3$. As the outer fluid gets heavier, the threshold We_1 for instability becomes larger. If $\rho_r \to 1$, the threshold We_1 tends towards infinity and the column remains stable for all perturbations.

$n(n+1)$. As expected, the critical We_1 required for instability increases as density ratio gets closer to 1. Besides the critical We_1, the growth rate is large if the density ratio is large, indicating that the instability is driven by the inertia of the rotating fluid. If the density ratio is large, the critical We_1 for stability varies between $n(n+1)$ (for $\xi \to 0$) and n^2-1 (for $\xi \to 1$).

We can also look at the variation of growth rates for various radius ratios at a fixed density ratio (2.6). The effect of wall in suppressing the growth rates (for a given density ratio) is clearly seen in these plots.

We now specialize the general case illustrated by Ross to model a rigidly rotating water column with an embedded air core, thus setting $\rho_r \to 0$ and $\xi \to 0$ with We_2 being finite. Physically, this represents the case for an annulus of liquid column with an embedded air core with the outer wall at infinity. In this case, the dispersion relation 2.7 reduces to

$$\hat{\sigma}^2 - \frac{n(n^2-1)}{We_2} - (n+1) = 0 \tag{2.9}$$

This relation, being a quadratic, yields two roots given by

$$\sigma = n+1 \pm \sqrt{1 + \frac{n\,(n^2-1+We_2)}{We_2}} \tag{2.10}$$

Clearly, the eigenvalues are always real indicating the absence of unstable modes (fig. 2.7). As the radius ratio gets close to one, the wall effects force the two modes to behave in a

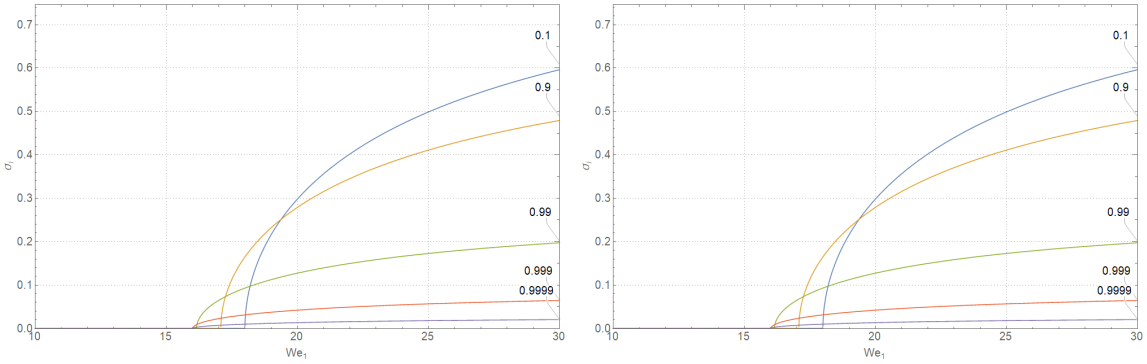

(a) $\rho_r = 10$ (b) $\rho_r = 2$

Fig. 2.6 Variation of growth rates with We (σ_i vs We_1) for various radius ratiosat fixed density ratios. As the heavy inner column approaches the wall ($\xi \to 1$), the threshold We decreases but the growth rates are suppressed.

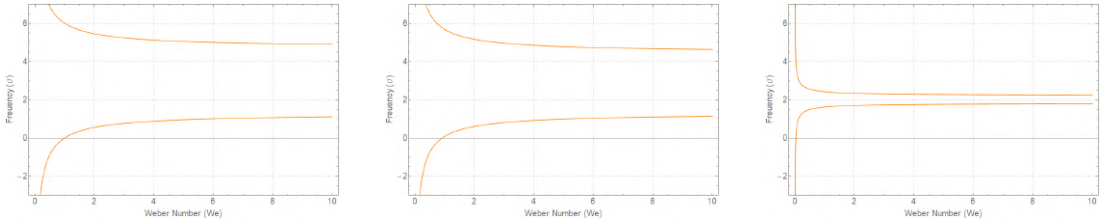

(a) $\xi = 0.1$ (b) $\xi = 0.5$ (c) $\xi = 0.999$

Fig. 2.7 Variation of the neutral modes (σ_r vs We_2) of the rotating annular liquid column with radius ratio. As $\xi \to 1$, the modal frequencies tend towards $n\Omega$ and the perturbation flows rotate rigidly along with the column.

rigidly rotating manner at large We. To summarize then, regardless of the nature of the perturbation considered, a rigidly rotating annular of liquid surrounding a central cylindrical air core does not admit any instability above a threshold Weber number.

Three-dimensional perturbations of a rotating annulus have been studied by Kubitschek and Weidman [7]. Owing to the stabilizing influence of the centrifugal force, this configuration does not show the peculiar behaviour seen for the three-dimensional perturbations of a rotating liquid column noted in Chapter 1.

2.4 Rankine Vortex With Air Core

As the next step towards modeling the interaction of a vortex ring with an air bubble, we add an irrotational flow to the exterior of the rigidly rotating liquid column. We therefore analyze the stability of a Rankine vortex with an embedded air core in this section.

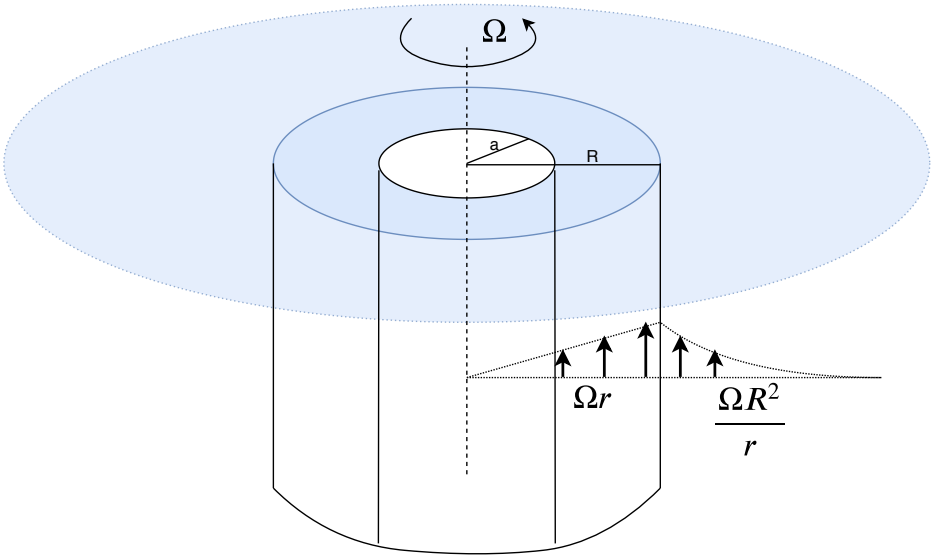

Fig. 2.8 The base state including a rigidly rotating annulus with an irrotational exterior flow. The relevant non dimensional parameters are the radius ratio ($\xi = a/R$) and the Weber number ($We = \rho\Omega^2 a^3/\gamma$) where ρ is the density of the ambient liquid. The inner fluid has been assumed inertialess.

2.4.1 Axisymmetric Perturbations

The dispersion relation for axisymmetric pertubations of a Rankine vortex with an embedded air core is given by

$$\frac{\sigma^2\alpha}{k^2}\Delta = \frac{\xi}{We}\left(1-k^2\xi^2-We\right) \tag{2.11}$$

where

$$\Delta = \frac{\alpha K_1(k)\left(Y_0(\alpha)J_0(\alpha\xi)-J_0(\alpha)Y_0(\alpha\xi)\right)+kK_0(k)\left(Y_1(\alpha)J_0(\alpha\xi)-J_1(\alpha)Y_0(\alpha\xi)\right))}{\alpha K_1(k)\left(Y_0(\alpha)J_1(\alpha\xi)-J_0(\alpha)Y_1(\alpha\xi)\right)+kK_0(k)\left(Y_1(\alpha)J_1(\alpha\xi)-J_1(\alpha)Y_1(\alpha\xi)\right)}$$

As in the earlier cases of axisymmetric perturbations, this dispersion relation leads to an infinite number of modes. As a check on 2.11, it is possible to recover Kelvin's dispersion relation for the Rankine vortex in the limit of vanishing air core radius ($a \to 0$). In terms of dimensionless parameters, this requires taking the limits $\xi \to 0$ and $We \to 0$. Note that $\frac{\xi}{We} = \frac{\gamma}{\rho\Omega^2 a^2 R} \to \infty$ in the limit $a \to 0$. It follows that

$$\alpha K_1(k)\left(Y_0(\alpha)J_1(\alpha\xi)-J_0(\alpha)Y_1(\alpha\xi)\right)+kK_0(k)\left(Y_1(\alpha)J_1(\alpha\xi)-J_1(\alpha)Y_1(\alpha\xi)\right)=0$$

Further considering $\xi \to 0$ gives

$$\alpha K_1(k)(-J_0(\alpha)) + kK_0(k)(-J_1(\alpha)) = 0 \tag{2.12}$$

$$\Rightarrow \frac{K_0(k)J_1(\alpha)}{K_1(k)J_0(\alpha)} + \frac{\alpha}{k} = 0 \tag{2.13}$$

which is the dispersion relation for Rankine vortex for axisymmetric perturbations. We now explore the effect of radius ratio (ξ) and the Weber number (We) on the eigenvalue spectrum of this system.

Effect of Weber Number and radius ratio

Fig. 2.9 shows an entire grid of dispersion curves; We varies for a fixed ξ along a column, and ξ varies for a fixed We along any given row. For $We < 1$, the system shows a clear change in behaviour across $k = \sqrt{1-We}/\xi$; in that, the modes are rotation-dominated for k smaller than this threshold, while the outer capillary modes recover the usual $k^{3/2}$ scaling for larger k, departing from the remaining Coriolis-driven modes. As We increases from 0 toward unity, the transition k shifts toward 0. For $We > 1$, the k required for such a transition becomes imaginary. The two outermost modes are then predominantly driven by surface tension, even in the regime $k \to 0$. This can be seen in the subplots of fig. 2.9 with $We > 1$, where the two outermost modes show a scaling behaviour different from other (Coriolis-force-driven) modes even for small k. If $\xi \to 1$, the Coriolis force driven modes vanish and only the two capillary modes remain finite. Fig. 2.10 shows a comparison of the axisymmetric dispersion curves to the two classical cases - the inverse Rayleigh-Plateau problem and the Rankine vortex. For the small We considered, one observes the dispersion curves transition from those of the Rankine vortex for small k, to those of the inverse Rayleigh-Plateau for large k.

2.4.2 Planar Perturbations

The key difference between the present case and the rotating annular liquid column is the presence of a vorticity interface for the Rankine vortex(the outer boundary of the rigidly rotating region) which can sustain one inertial wave for a given azimuthal wavenumber as was shown by Kelvin [18]. Taking this into account, we expect three waves (or modes) for this system as opposed to two for the rotating annulus (eq. 2.10) - two primarily surface tension driven modes (akin to those in fig. 2.7c) and one primarily inertial mode akin to the 2D Kelvin wave.

The dispersion relation for this case, therefore, takes the form of a cubic in $\hat{\sigma}(= \sigma - n)$

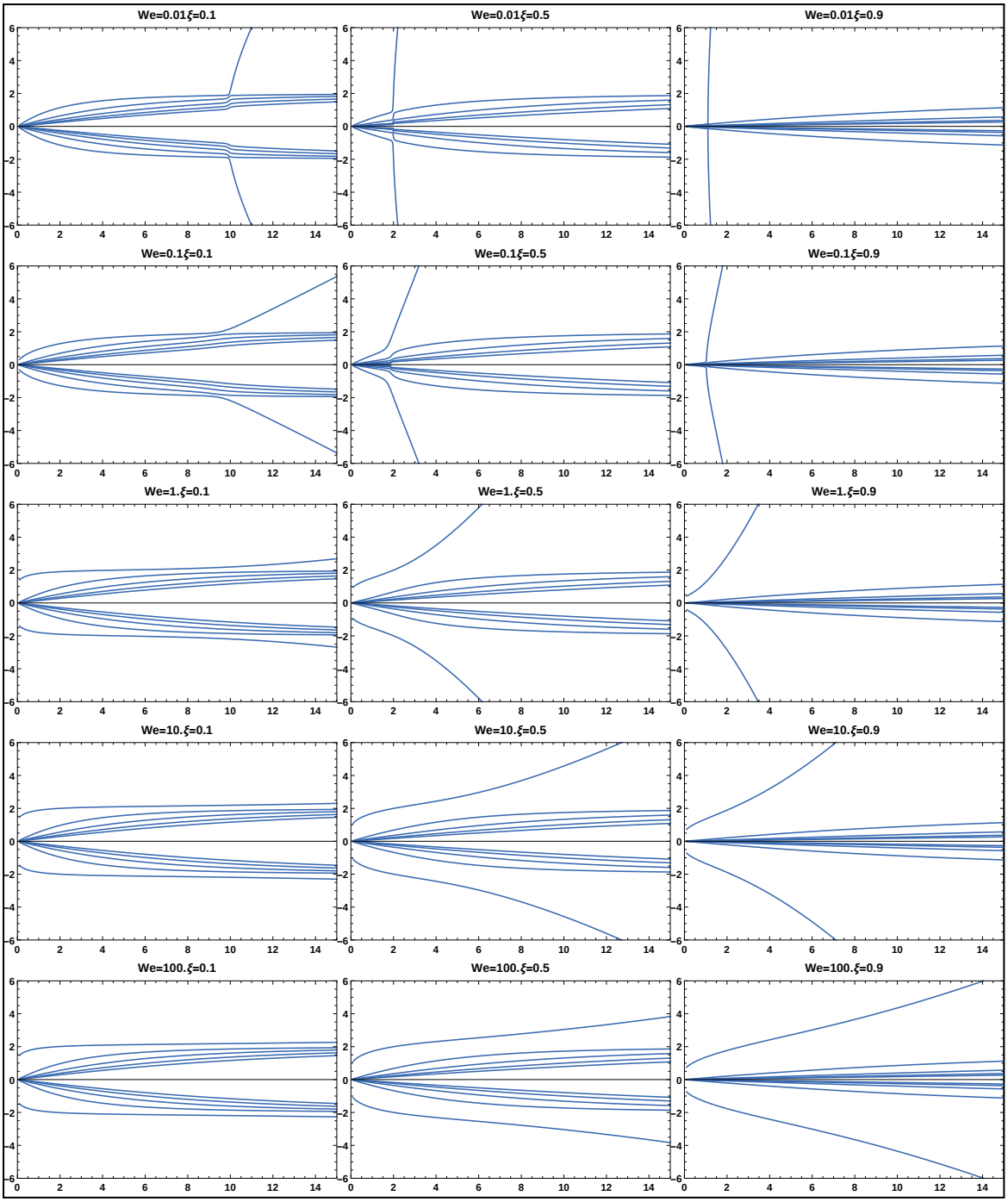

Fig. 2.9 Dispersion curves(σ vs k) for axisymmetric modes of a Rankine vortex with air core and their variation with We and ξ. We increases down the columns and ξ increases along a row.

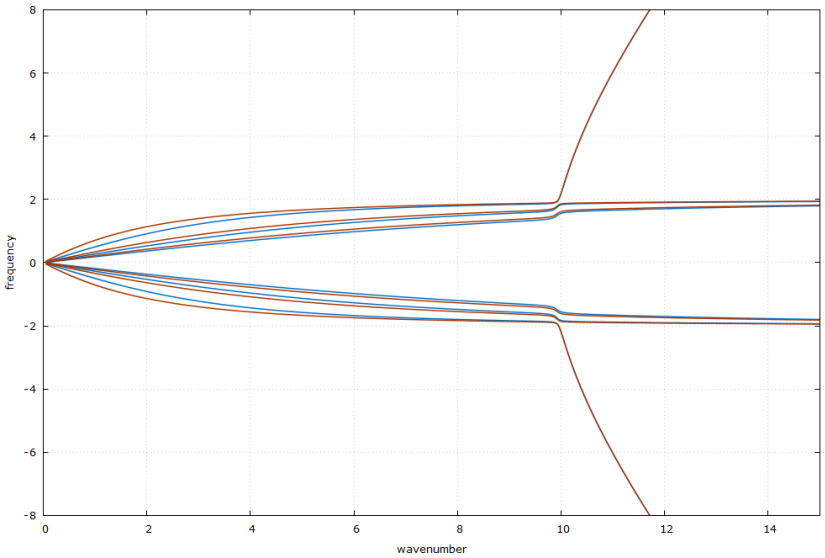

(a) Modes of the Inverted Rayleigh-Plateau configuration (blue) match well with those of Rankine vortex with air core(red) for large k.

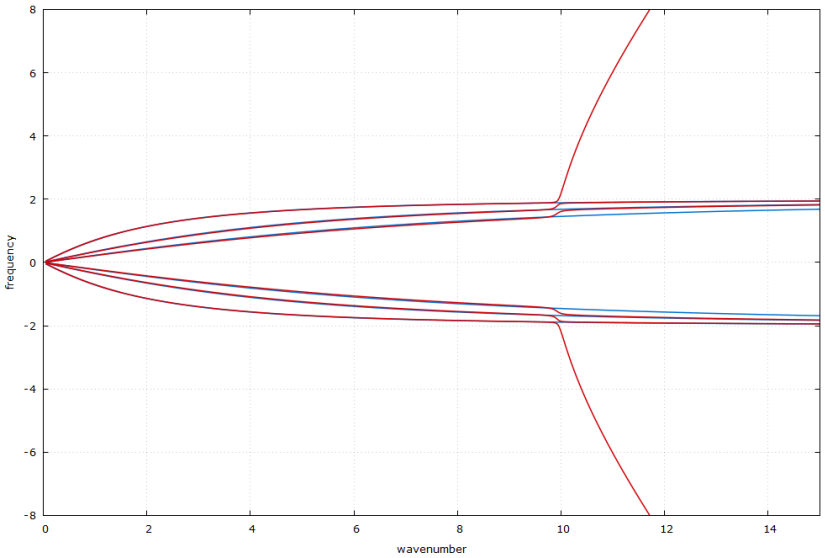

(b) Modes of the Rankine vortex (blue) match well with those of the Rankine vortex with air core (red) for small k.

Fig. 2.10 Comparison of modes of the Rankine vortex with air core with those of (a)the Inverted Rayleigh-Plateau and (b)the Rankine vortex. For small ξ, the modes of the Rankine vortex with air core can be mapped to those of the Rankine vortex for small k and to those of the inverted Rayleigh-Plateau configuration for large k. For the curves shown here, $We = 0.01$ and $\xi = 0.1$.

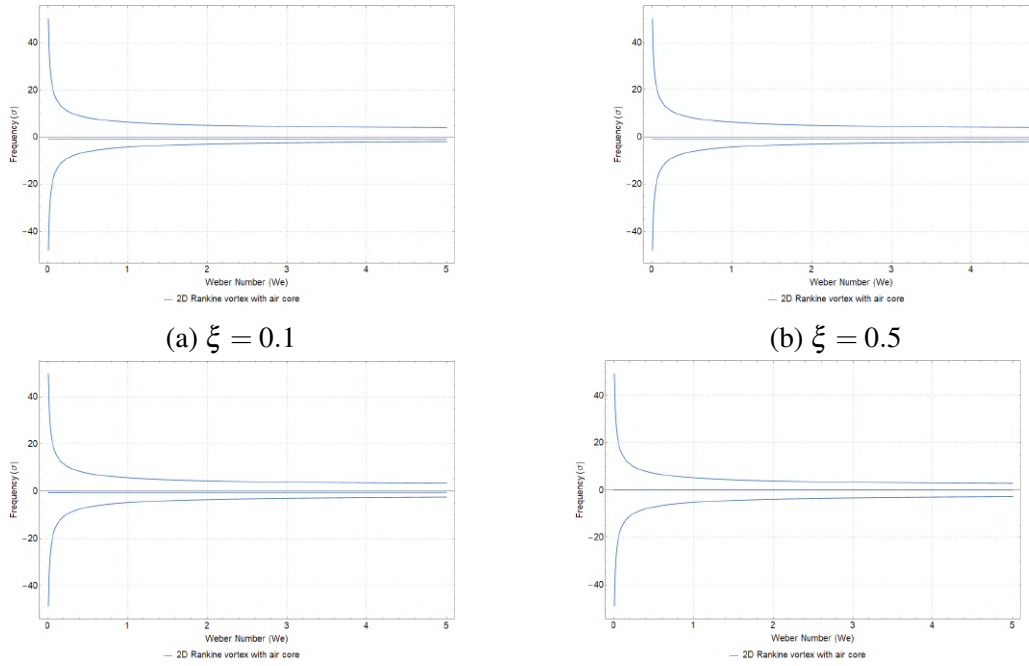

(a) $\xi = 0.1$ (b) $\xi = 0.5$

(c) $\xi = 0.9$ (d) $\xi = 0.999$

Fig. 2.11 Variation of the neutral modes with We for $n = 2$ (in the reference frame of the column). For $\xi \to 1$, the frequency of the inertial mode vanishes and the perturbation flow rotates rigidly with the column. Other two modes are symmetrically displaced about $\sigma = 0$ in this limit.

$$\hat{\sigma}^3 + \alpha\hat{\sigma}^2 + (2\alpha + \beta)\hat{\sigma} - \alpha\beta = 0 \tag{2.14}$$

where

$$\alpha = \xi^{2n} - 1$$
$$\beta = \left(1 - n^2 - We\right)\frac{n}{We}$$

Being a cubic, it yields three modes, as expected from our earlier arguments. The fact that two of these modes are modified capillary wave like modes while the third is a modified Kelvin wave mode becomes explicit if one considers the limit of a small air core relative to the vortex core i.e. $\xi \to 0$. In this limit, two eigenvalues reduce to

$$\sigma = n + 1 \pm \sqrt{1 + \frac{n\left(n^2 - 1 + We\right)}{We}} \tag{2.15}$$

which are the modes of the rotating column with an outer wall. The third mode reduces to $\sigma = n - 1$ which is the frequency of the $2D$ Kelvin mode for the Rankine vortex. Fig. 2.11 shows the behaviour of the three eigenvalues with We for varying radius ratios.

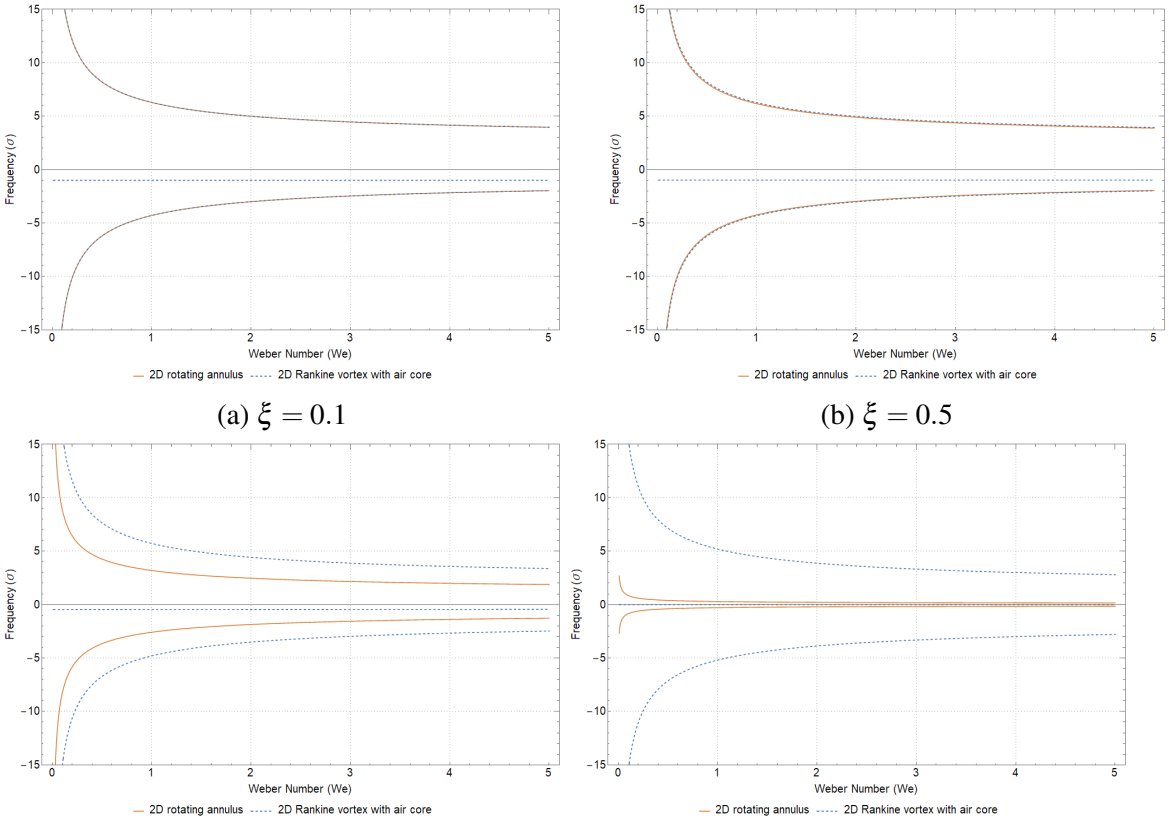

(a) $\xi = 0.1$ (b) $\xi = 0.5$

(c) $\xi = 0.9$ (d) $\xi = 0.999$

Fig. 2.12 Comparison of the neutral modes of the Rankine vortex with air-core with those of the rotation liquid column with air core. The ordinate represents the Doppler frequencies.

A comparison of the planar-wave dispersion relation for the Rankine vortex with an embedded air core, with the rigidly rotating liquid annulus examined earlier, has been shown in fig. 2.12. For small ξ, the effects of the outer wall are minimal and the capillary wave like modes of the hollow Rankine match well with the modes of the hollow solid vortex. The Kelvin mode doesn't vary with *We* at small ξ. For $\xi \to 1$, the azimuthal speed of propagation of the Kelvin wave (σ/n) becomes equal to the angular velocity of the column (Ω). The perturbation therefore remains stationary with respect to the column. For ξ close to 1, the capillary waves differ in the two cases. For the Rankine vortex with air core, these modes continue to propagate with finite non-zero velocities, but for the rotating annulus, the Doppler frequencies of the modes vanish for large *We* and the perturbations rotate rigidly with the core.

2.4.3 Three-dimensional perturbations

The dispersion relation for this case is given by

$$\begin{aligned}
&\left[J_m(\eta\xi)+\frac{\chi}{\hat{\omega}(4-\hat{\omega}^2)}\Big((\hat{\omega}-2)\frac{m}{\xi}J_m(\eta\xi)-\hat{\omega}\eta J_{m+1}(\eta\xi)\Big)\right]\\
&\left[Y_m(\eta)k_0K_m'(k_0)-\frac{\hat{\omega}K_m(k_0)}{4-\hat{\omega}^2}\Big((\hat{\omega}-2)mY_m(\eta)-\hat{\omega}\eta Y_{m+1}(\eta)\Big)\right]\\
&=\left[Y_m(\eta\xi)+\frac{\chi}{\hat{\omega}(4-\hat{\omega}^2)}\Big((\hat{\omega}-2)\frac{m}{\xi}Y_m(\eta\xi)-\hat{\omega}\eta Y_{m+1}(\eta\xi)\Big)\right]\\
&\left[J_m(\eta)k_0K_m'(k_0)-\frac{\hat{\omega}K_m(k_0)}{4-\hat{\omega}^2}\Big((\hat{\omega}-2)mJ_m(\eta)-\hat{\omega}\eta J_{m+1}(\eta)\Big)\right]
\end{aligned} \tag{2.16}$$

where $\chi=\frac{\xi}{We}(1-m^2-\xi^2k^2-We)$. The above relation reduces to the axisymmetric relation (eq. 2.11) upon setting $m=0$ and to the Rankine vortex dispersion relation for three-dimensional perturbations if one considers the limit of vanishing air core ($\xi, We\to 0$ such that $\frac{\xi}{We}\to\infty$). Fig. 2.13 and 2.14 show the effect of varying ξ and We on the dispersion curves for the three-dimensional perturbations for $n=1$ and 2 respectively. It is worth noting that, for all cases considered thus far, there is a trivial antisymmetry relation between the dispersion curves for positive and negative n (for the same k).

2.5 Hollow Rankine Vortex with external strain

The final step in our modeling of the interaction of an air-bubble with a vortex ring is to account for the self-induced straining flow of the vortex ring. Earlier works of Moore and Saffman [11] and Tsai and Widnall [19] on single phase vortex rings have considered the effect of a weak self-induced flow (in the limit of thin rings), and identified a parametric resonance-driven instability in vortex rings, now known as the MSTW instability. For the original single-phase vortex ring, and in the thin ring approximation (when the ring cross-section is much smaller than its radius), the self-straining flow may be approximated as a planar linear extensional flow acting on a columnar vortex. For the present case, therefore, we consider a weak planar extensional flow acting on a Rankine vortex but with a concentrically embedded air core within (fig. 2.15). The non-dimensional strength of the straining field is denoted by ε where the strain-rate has been scaled with the angular velocity of the rigidly rotating vortex core (Ω). Note that the parametric resonance above refers to the coupling induced by the linear straining flow between Kelvin modes, of identical frequencies, but with azimuthal wave numbers separated by 2 (that is to say, the resonating pair is $(n,n+2)$). While

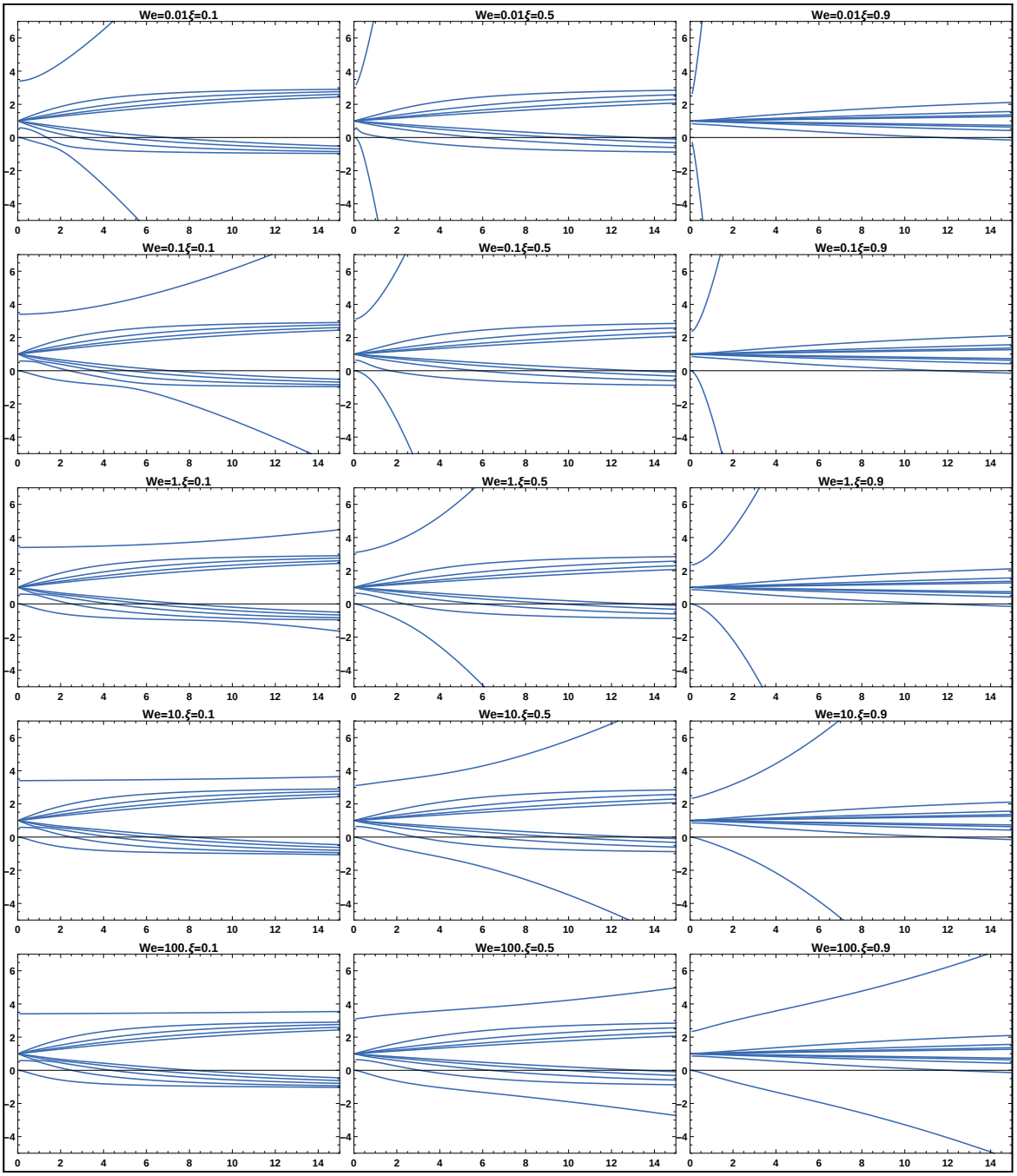

Fig. 2.13 Variation of the set of dispersion curves for $n = 1$ with ξ and We

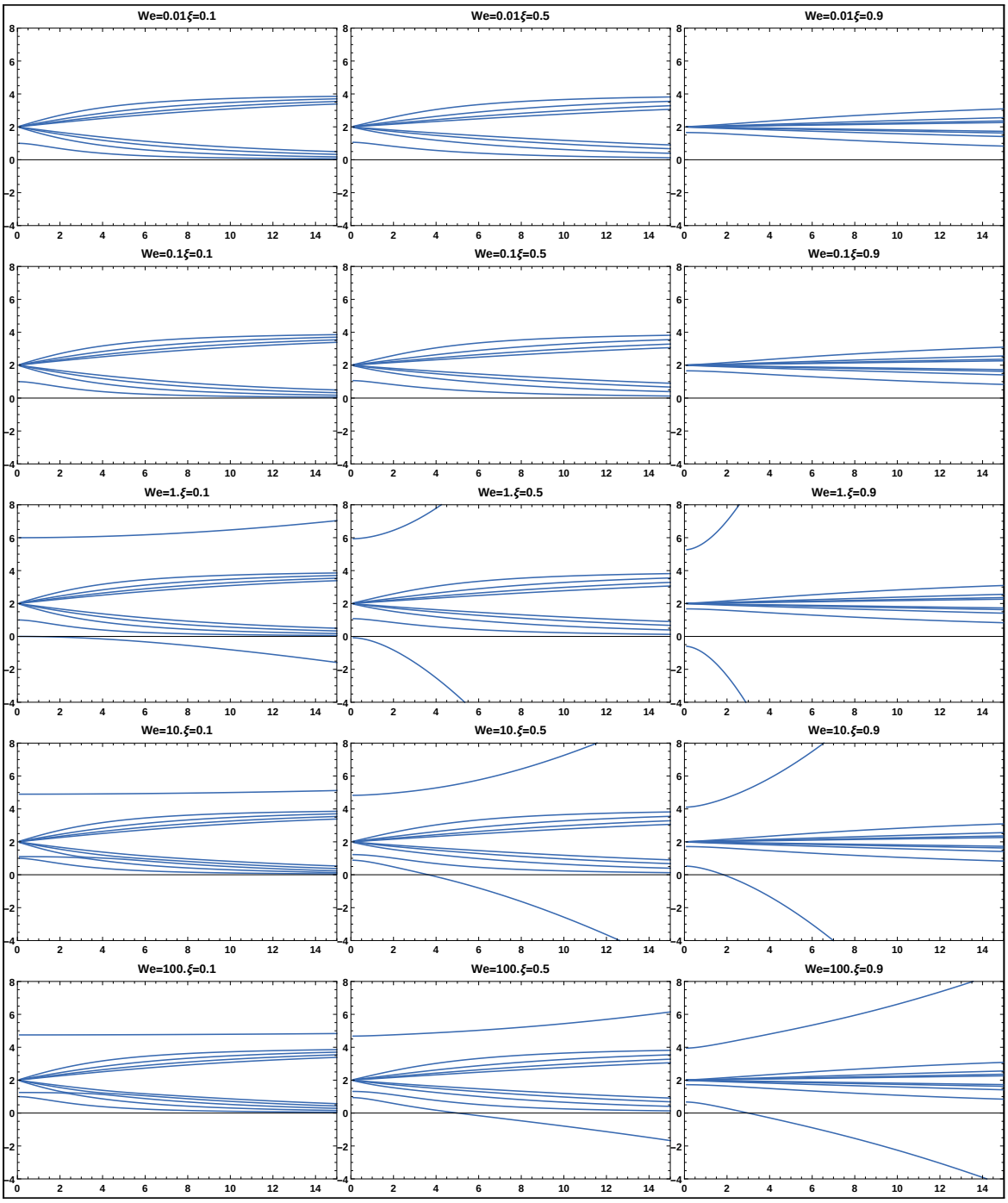

Fig. 2.14 Variation of the set of dispersion curves for $n = 2$ with ξ and We

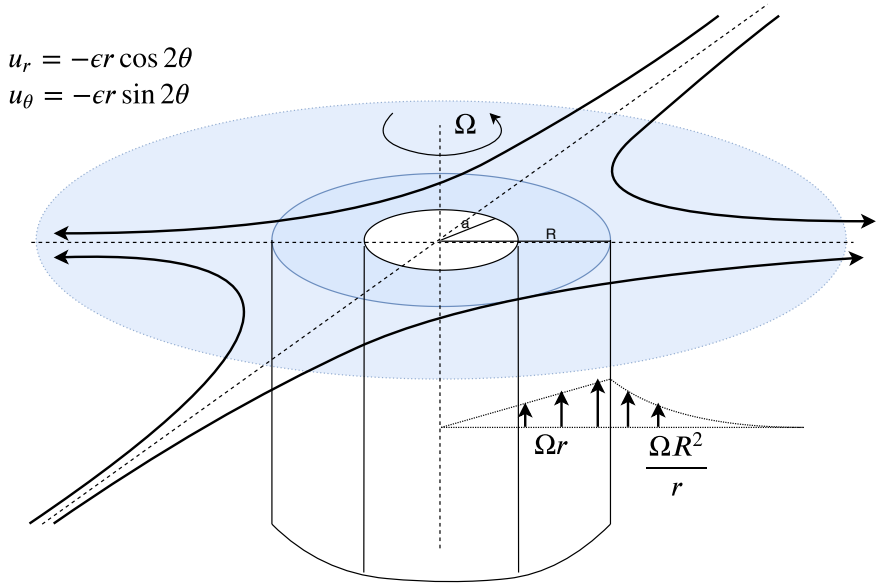

Fig. 2.15 Rankine vortex with air core under a weakly imposed planar-extensional flow. The relevant non-dimensional parameters are the Weber number ($We = \rho\Omega^2 a^3/\gamma$) and the radius ratio ($\xi = a/R$).

n is, in principal, arbitrary, the dominant pair of resonating Kelvin modes that contribute to the MSTW instability corresponds to $n = 1$ and -1. It is worth noting that assessing the possibility of a parametric resonance does not require one to do the actual stability problem with the straining flow present. As indicated above, the resonating modes are the original Kelvin modes of the unstrained Rankine vortex, and having identical frequencies. The existence of such pairs of modes, with azimuthal wavenumbers separated by two, and with the same axial wavenumber and frequency, is thus a necessary condition for parametric resonance. A sufficient condition for such modes to lead to an instability is more complicated, and related to the energy criterion - the appropriately defined perturbation energies associated with the resonating modes should have opposite signs. Nevertheless, herein, motivated by the aforementioned necessary condition for resonance, we will examine the nature of the dispersion curve intersections in what follows, but for the strained Rankine vortex with an embedded vortex core.

To begin with, we determine the base state flow fields for the aforementioned configuration. The shape of a vortex core deformed under the influence of an external linear straining flow is exactly known due to Saffman [10], but the deformation of the column in the presence of an air core has not yet been studied and must be determined as part of the base state. Note that the original analysis, without the vortex core, can, in fact, be carried out for arbitrary amplitudes of the straining flow since the deformed vortex core remains elliptic regardless of

amplitude (above a critical strain-to-core-vorticity ratio, the core deforms continuously, and there exists no steady state). In contrast, the existence of a central air core, and the action of surface tension at the air-water interface, implies that the deformation will not remain elliptic for finite amplitudes. Thus, the analysis that follows is necessarily restricted to a weak straining flow.

Let the deformed vortex core be given by $r = 1 + \alpha\varepsilon e^{2i\theta}$ and the deformed air core be $r = \xi + \beta\varepsilon e^{2i\theta}$, where the radii of the vortex core and the air-core have been scaled with R and α and β are the (constant) amplitudes to be determined. Owing to the irrotational nature of the perturbation velocity, the flow fields within the annular vortex core ($\xi < r < 1$) take the following general forms

$$\begin{aligned} u_r &= 2\varepsilon\left(Ar - B/r^3\right)e^{2i\theta} \\ u_\theta &= r + 2i\varepsilon\left(Ar + B/r^3\right)e^{2i\theta} \\ u_z &= 0 \\ p &= r^2/2 - 1 - 4i\varepsilon B e^{2i\theta}/r^2 \end{aligned} \tag{2.17}$$

The exterior flow ($r > 1$), being irrotational, can be specified using only a velocity potential given by

$$\phi = \theta + \varepsilon\left(Cr^2 + D/r^2\right)e^{2i\theta} \tag{2.18}$$

where the constants A, B, and D are to be determined from the boundary conditions. The constant C is known as it denotes the imposed straining field. We therefore require five boundary conditions for the determination of the constants, two of these arise at the air-liquid interface ($r = \xi$) (the kinematic boundary condition requiring the fluid element to move with the interface, and the normal stress balance) and three at the vortex-core interface ($r = 1$) (the kinematic boundary condition applied to each of the interior and exterior velocity fields, and the normal stress balance). This yields the following expressions for the constants

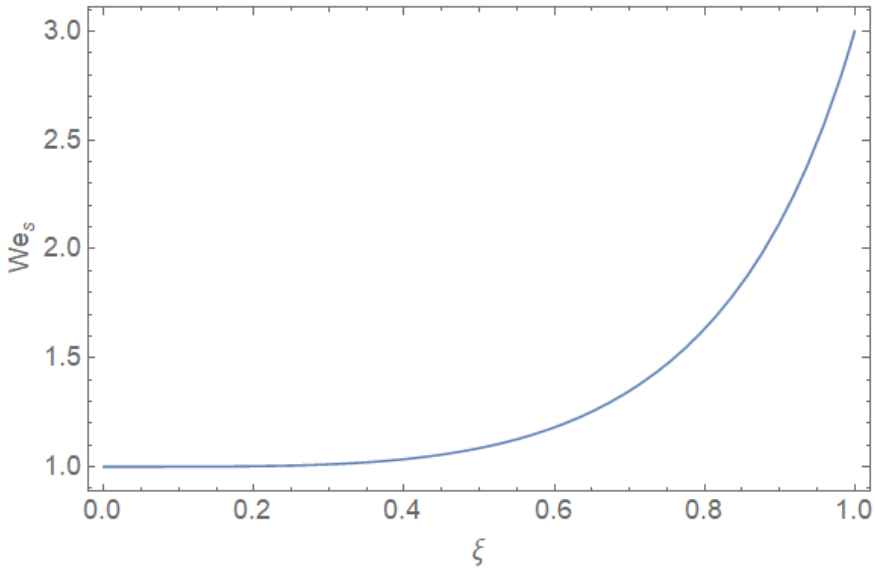

Fig. 2.16 Variation of the Weber number corresponding to the base state singularity(We_s) with radius ratio(ξ).

$$
\begin{aligned}
A &= \frac{i\lambda}{2(\lambda+\xi^4)} \\
B &= \frac{i\xi^4}{2(\lambda+\xi^4)} \\
C &= \frac{i}{4} \\
D &= \frac{i}{4}\left(\frac{3\xi^4-\lambda}{\xi^4+\lambda}\right) \\
\alpha &= \frac{\lambda-\xi^4}{2(\lambda+\xi^4)} \\
\beta &= \frac{-2We\xi}{(We+3)(\lambda+\xi^4)}
\end{aligned}
\tag{2.19}
$$

where λ is given by $\lambda = \frac{3-3We}{3+We}$. It can be shown that the flow fields thus obtained, reduce to the corresponding fields given by Widnall [19] under the limit $\xi \to 0$. However, for non-zero ξ, there exists a singularity in the flow fields at $\lambda = -\xi^4$ or, along the curve $We = We_s = \frac{1+\xi^4}{1-\frac{\xi^4}{3}}$. This variation of We_s with ξ is shown in fig. 2.16. We briefly address the origin of this singularity in the base state before proceeding with the stability analysis.

We first note that a (weak) linear straining flow with 2θ symmetry (the terms proportional to A in eq. 2.17) would deform the column in a manner similar to that of a planar perturbation

with azimuthal wavenumber $n = 2$. It therefore makes sense for us to investigate the case of a Rankine vortex with air core (without external strain) undergoing small-amplitude planar oscillations with $n = 2$. This case was studied in section 2.4.2. The dispersion curves corresponding to $n = 2$ have been reproduced in fig. 2.17. In this figure, it can be seen that We_s in fact denotes the We corresponding to a zero crossing of the lower capillary branch, as it transitions from a retrograde to a co-grade character. Note that the speed of a perturbation wave(with azimuthal wavenumber n) traveling along the azimuth is given by σ/n. It therefore follows that, at $We = We_s$, the said capillary mode is stationary in the lab frame and thereby allows the straining flow to deform it further. The continued action of the straining flow, for an infinite amount of time, leads to divergent amplitudes of deformation. Note, however, that this singularity is a consequence of our assumption of the deformation being linear in the strain rate and indicates that, in the vicinity of We_s, the deformation scales differently; that is to say, the deformation is more sensitive to the imposed straining flow in the neighborhood of $We = We_s$, with the amplitude of deformation being stronger than $O(\varepsilon)$, the exact scaling likely determined by a balance involving nonlinear terms. Although the singularity of the base-state found here is of interest, it may not be relevant to the experiments that have motivated the current study, since the We's corresponding to the singular response remain moderate regardless of the radius ratio ($We_{s\,max} = 3$). We therefore continue the linear stability analysis with the implicit focus on We's much greater than We_s (as in the experiments) for any given ξ with the base-state given by eq. 2.17 and 2.19 while ensuring that we do not consider We close to We_s for given ξ.

We now continue with the linear stability analysis of the strained Rankine vortex with air core along the lines of Tsai and Widnall [19]. As mentioned earlier, the MSTW instability involves a coupling of two individually neutral modes via an external straining flow. Owing to the the 2θ symmetry of the flow, a coupling of two perturbations of the form n and $n+2$ is made possible. Physically, we see that a superposition of two waves ($n = 1$ and -1 with identical value of k) leads to the formation of a standing wave on the column (fig. 2.18). Such a column is then deformed at an exponential rate by the straining flow. The possible parameter values where a resonance of two modes may lead to such an instability are obtained via intersections among the dispersion curves of the participating modes (fig. 2.19).

In order to investigate a parametric resonance in a strained Rankine vortex with air core, we now plot the set of dispersion curves for various values of ξ and We and look for the intersections i.e. possible sites for a parametric resonance. The two possibilities of parametric resonance presented here are $n = -1$ and 1 (fig. 2.20) and $n = 0$ and 2 (fig. 2.21). The original MSTW instability involves studying the dispersion curves of the Rankine vortex where all modes are driven by the Coriolis force. Consequently the instability arises

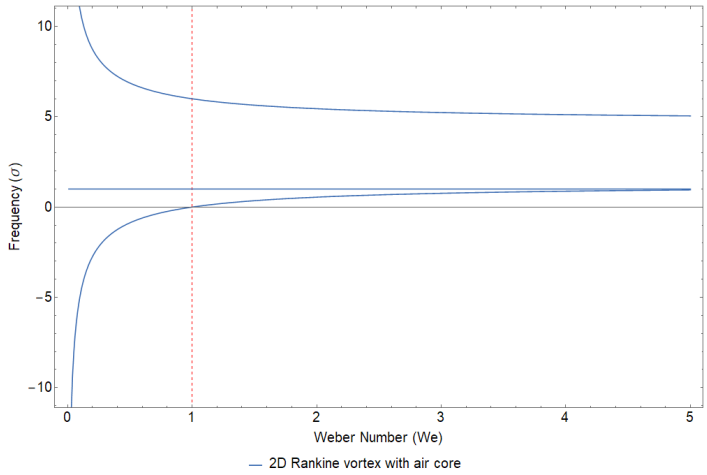

(a) $\xi = 0.1$

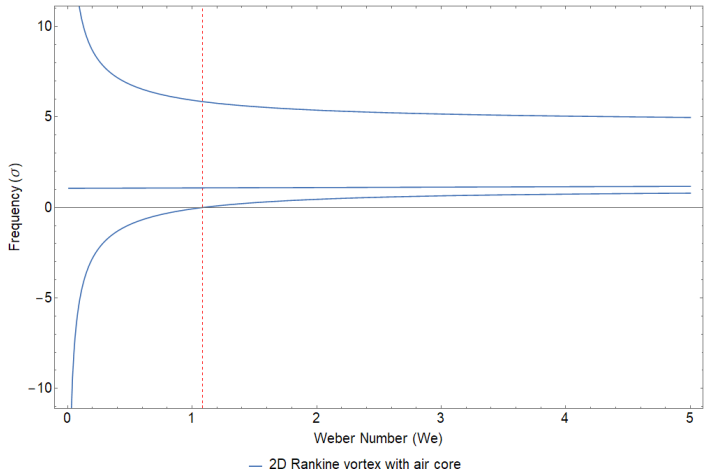

(b) $\xi = 0.5$

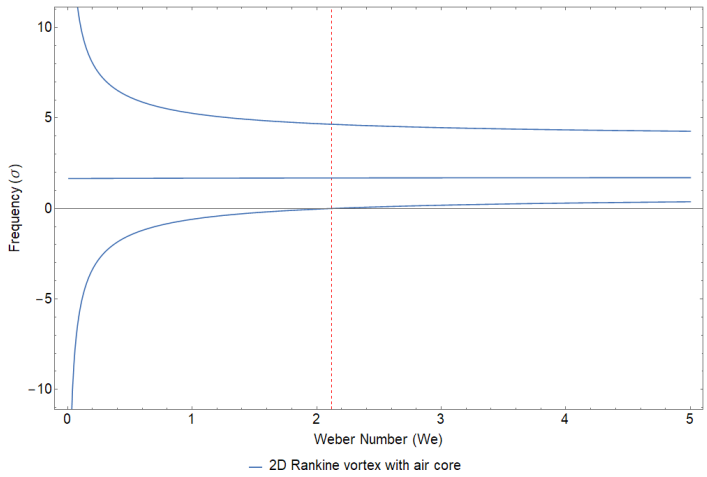

(c) $\xi = 0.9$

Fig. 2.17 Neutral modes of the Rankine vortex with air core under planar perturbation with $n = 2$. The singular Weber number (We_s - denoted by a vertical dashed line in the figure) is in fact the We corresponding to the zero-crossing of one of the neutral modes. It follows that the perturbation flow is stationary in the lab frame and therefore allows a large deformation by the straining flow.

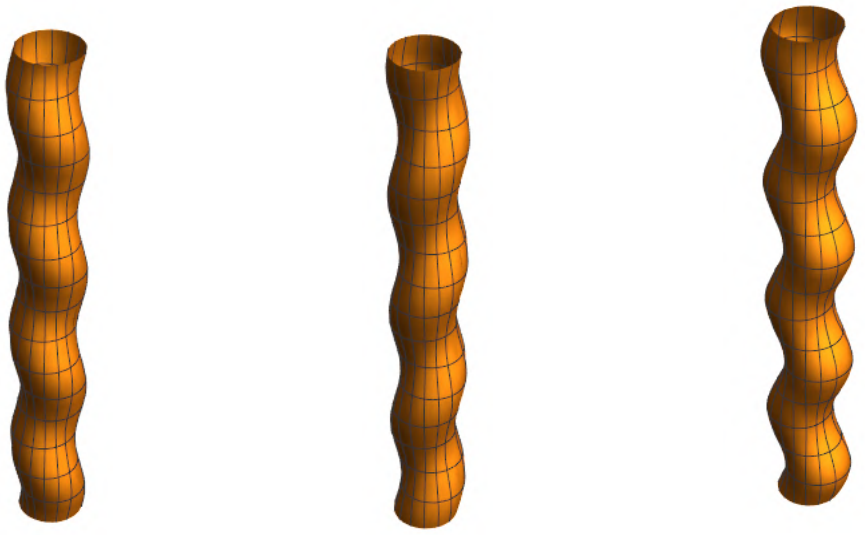

(a) $n = 1, k = 0.5$ (b) $n = 1, k = 0.5$ (c) Superposition of ($n = 1, k = 0.5$) and ($n = -1, k = 0.5$)

Fig. 2.18 Superposition of two modes with $n = 1$ and $n = -1$ results in a stationary wave that can be amplified by a straining flow.

due to the interaction of two Coriolis-force-driven modes. In the present case of Rankine vortex with air core, there exist two surface-tension-driven modes besides an infinity of Coriolis-force-driven modes. This leads to new classes of intersections between the two sets of dispersion curves shown in fig. 2.20 and 2.21. The first class of intersections correspond to the interaction between a surface-tension-driven and a Coriolis-driven mode and may be seen in fig. 2.20 and 2.21. The second class of intesections, which correspond to an interaction between two surface-tension-driven modes, appear only in 2.21. A magnified view of this intersection appears in fig. 2.22.

The intersections among two surface-tension-driven modes occur for large *We* and small k. Since the instability that might result from this intersection would involve long wavelength perturbations, it is expected that the effects of viscous damping may not be severe. Also, the *We* regime in which these intersections occur is comparable to the *We*'s in the experiments of Jha and Govardhan [6]. We therefore expect a parametric resonance, arising from these intersections, in the presence of a straining flow, leading to a new mechanism for instability in vortex rings with an entrained air-bubble, and serve as a possible explanation for the vortex-ring disruption and bubble breakup observed in the aforementioned experiments.

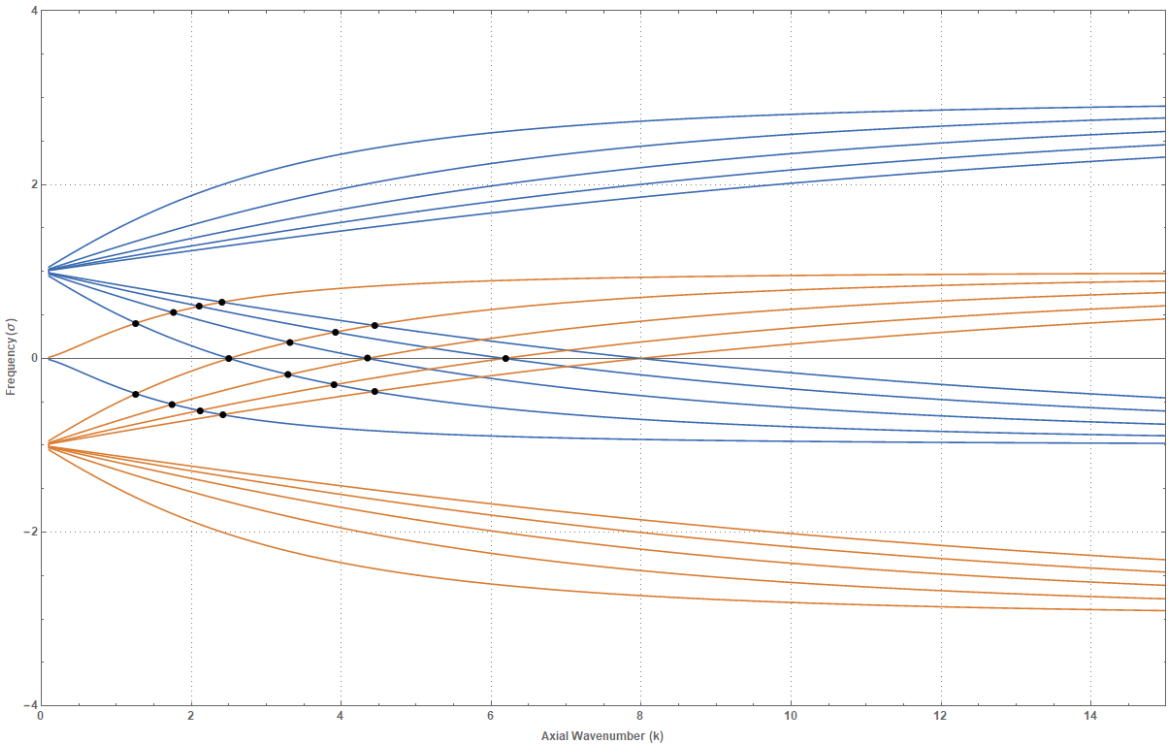

Fig. 2.19 Dispersion curves (frequency (σ) vs axial wavenumber(k)) for the Rankine vortex for $n = 1$(blue) and $n = -1$(orange). The intersections of the two curves denote possible parameter values for a parametric resonance leading to the MSTW instability.

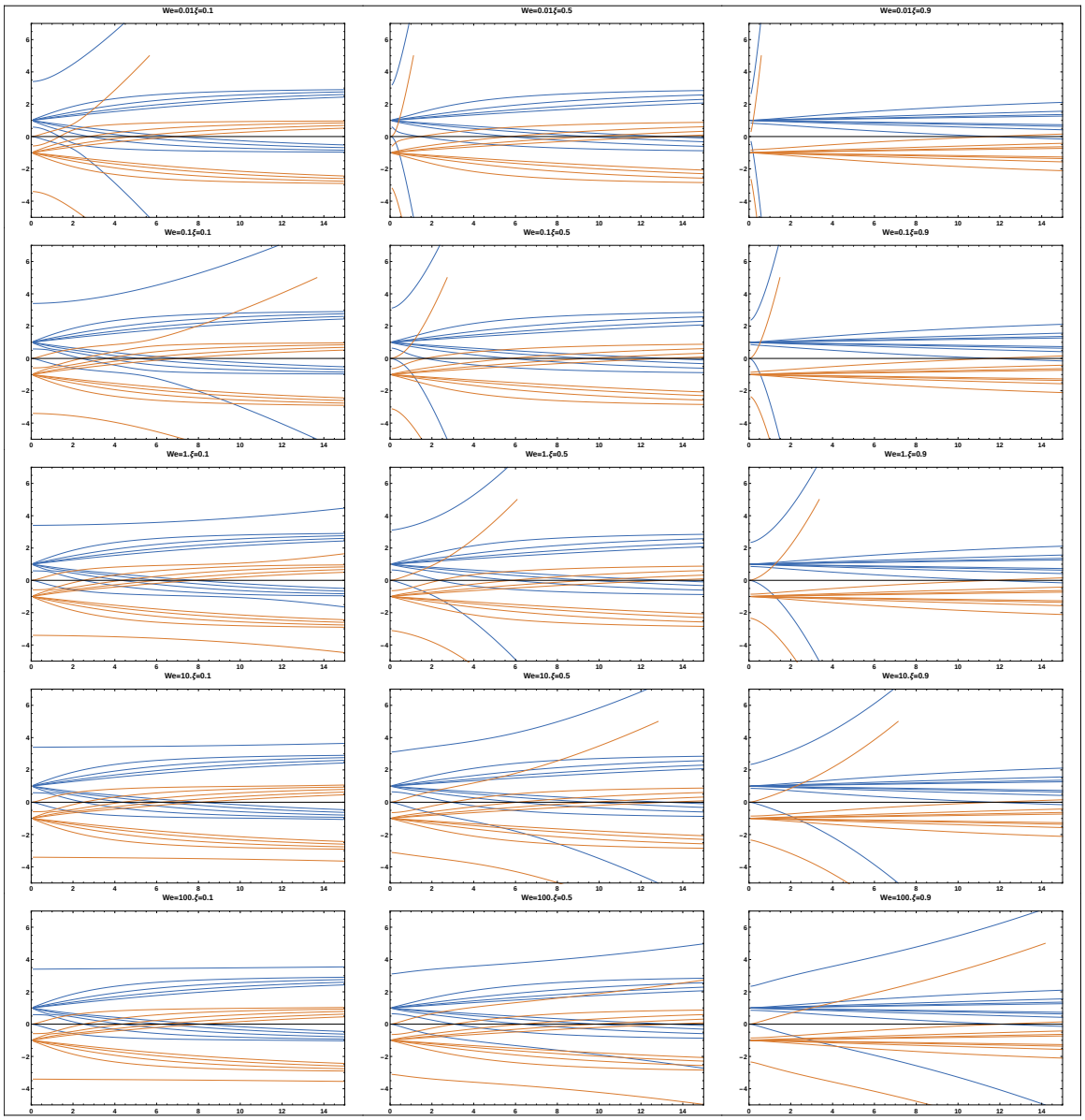

Fig. 2.20 Intersections among dispersion curves corresponding to $n = 1$ and $n = -1$. Besides the intersections of Coriolis-Coriolis modes, an intersection among a surface-tension-driven and a Coriolis-driven mode can also be seen. Intersections among two surface-tension-driven modes are absent here.

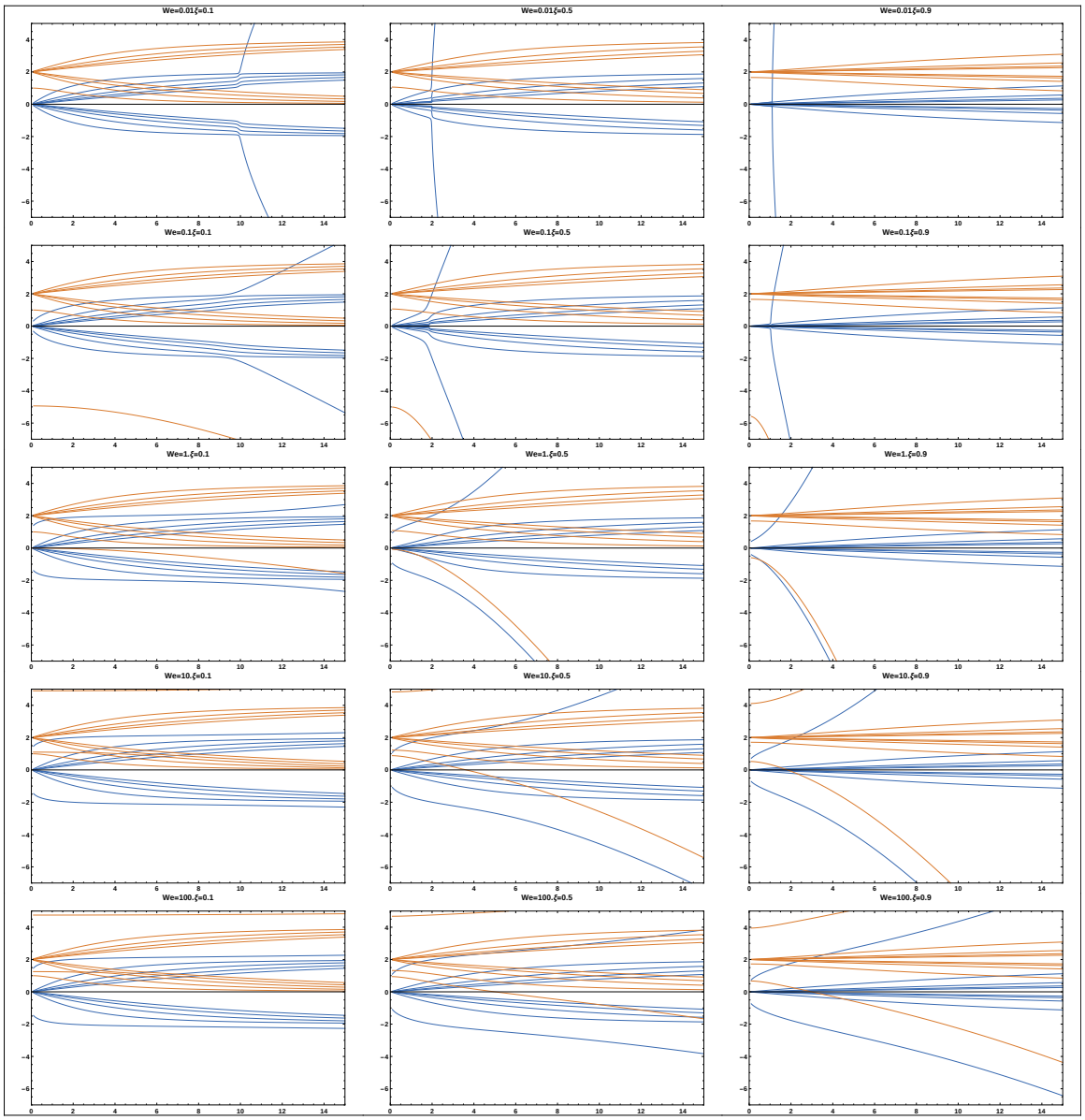

Fig. 2.21 Intersections among dispersion curves corresponding to $n = 0$ and $n = 2$. Besides the intersections of Coriolis-Coriolis modes, intersections among a surface-tension-driven and a Coriolis-driven mode as well as those between two surface-tension-driven modes (for $We \geq 1$) can be seen here.

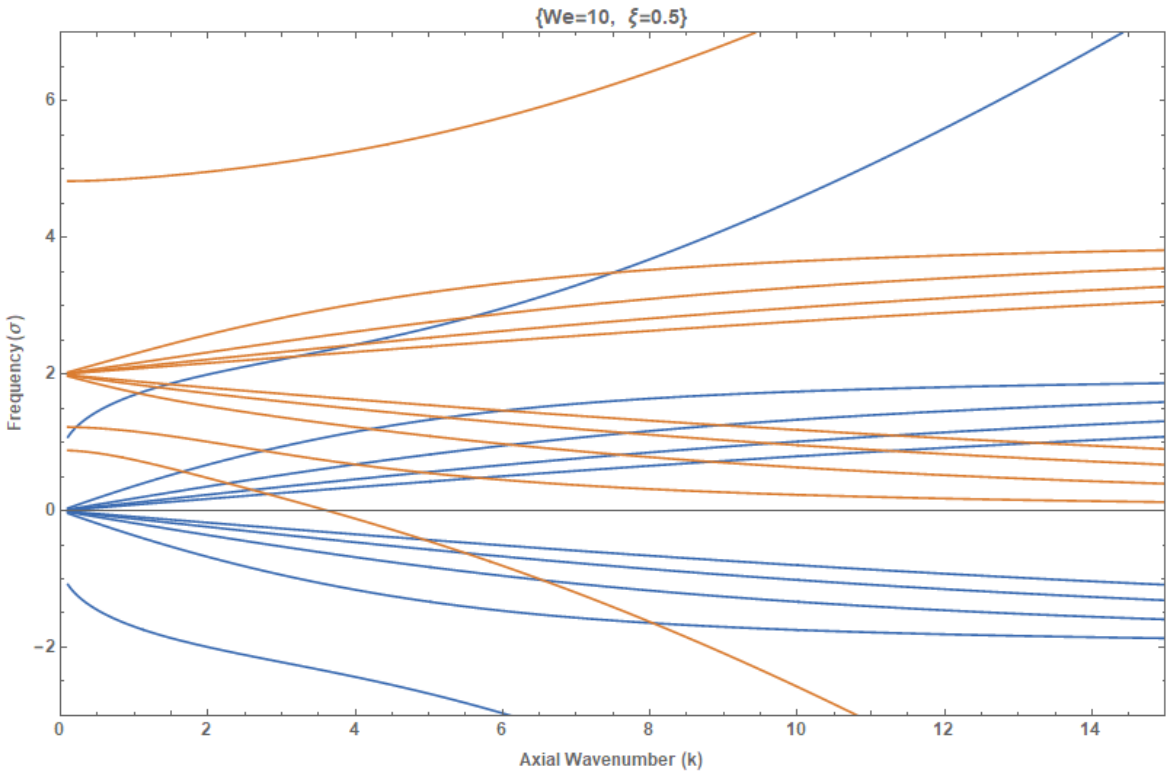

(a) Dispersion curves (frequency (σ) vs axial wavenumber (k)) for n=0 and 2, with $We = 10$ and $\xi = 0.5$. The figure indicates that the surface-tension-driven modes of n=0 and 2 can intersect for small k.

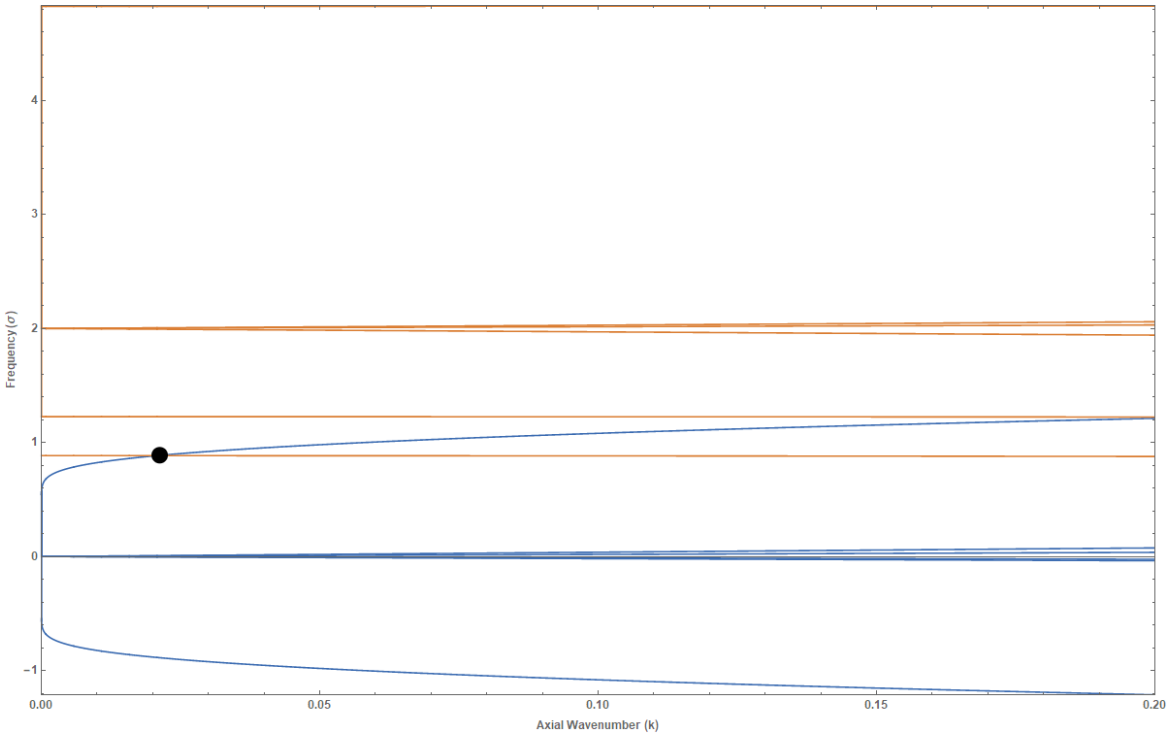

(b) A zoomed in view of (a) which clarifies the small k intersection of the two surface-tension-driven modes.

Fig. 2.22

Chapter 3

Inertial Orientation Dynamics of Spheroids in Planar Linear Flows

3.1 Introduction

Suspensions of anisotropic particles are ubiquitous in both natural and industrial scenarios, with the associated phenomena ranging in length scales from the microscopic (shape-sorting in microfluidic devices, for instance) to the geological (the influence of suspended anisotropic mineral crystals on magma motion, and the contribution of suspended ice crystals to cloud albedo). The bulk properties of such suspensions are crucially dependent on the orientation distribution of these particles subject to both external forces (for example, gravity) and shearing flows.

In this chapter, we will discuss the orientation dynamics of anisotropic particles in planar linear flows. Small anisotropic particles in any two-dimensional shearing flow see a planar linear flow on length scales comparable to their size; planar linear flows form a one-parameter family. The anisotropic particle is modeled as a spheroid with an arbitrary aspect ratio, and the focus of this chapter is on the effects of weak fluid inertia on the known nature of the orientation dynamics in the Stokesian realm. Thus, the relevant non-dimensional parameters are the spheroid aspect ratio (κ), the linear flow parameter (λ) and the particle Reynolds number (Re). The aspect ratio κ is defined as the ratio of the axial to equatorial diameter. Hence, $0 < \kappa < 1$ for oblate spheroids while $\kappa > 1$ for prolate spheroids; note that we also use the the eccentricity ($e = \sqrt{1 - 1/\kappa^2}$, for prolate spheroids and $e = \sqrt{1 - \kappa^2}$ for oblate spheroids), which always lies in the interval $(0, 1)$, as an alternative to the spheroid aspect ratio on occasion. The linear flow parameter (λ) measures the relative magnitudes of strain and vorticity for the linear flow under consideration, and ranges between -1 and 1; the three

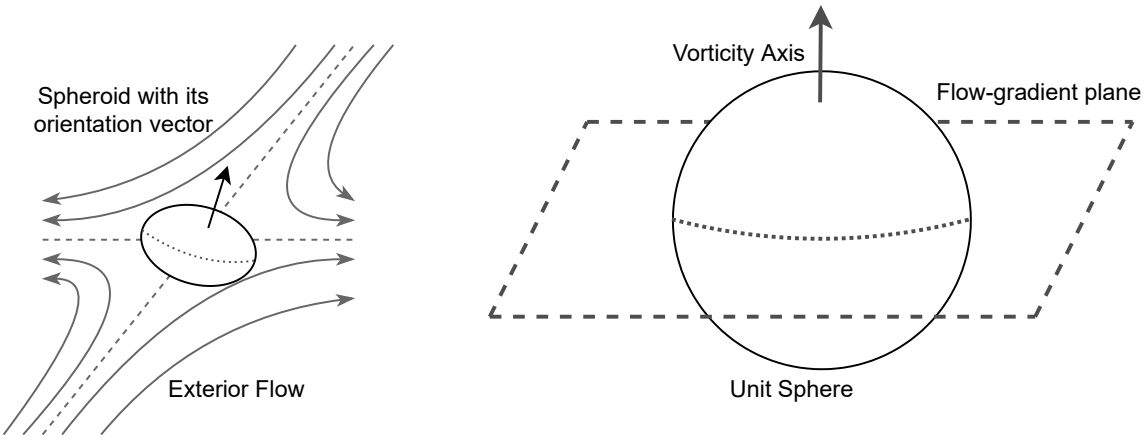

Fig. 3.1 A spheroid suspended in a planar linear flow. The figure to the left shows the physical picture while that to the right shows a unit sphere upon which trajectories traced by the orientation vector (a unit vector) of the rotating spheroid are plotted.

canonical cases being $\lambda = -1$ corresponding to solid body rotation, $\lambda = 0$ corresponding to simple shear flow, and $\lambda = 1$ corresponding to planar extension. $Re = \rho_f \dot{\gamma} L^2/\mu$ serves as a measure of fluid inertia on the scale of the suspended particle; here, L is the spheroid major axis, ρ_f is the density of the ambient fluid, $\dot{\gamma}$ is the strain rate and μ is the viscosity. The analysis in the chapter, as indicative above, is restricted to small but finite Re. The analysis does not include particle inertia and thus the Stokes number ($St = \rho_p \dot{\gamma} L^2/\mu$, ρ_p being the particle density) is taken to be zero.

The orientation dynamics of a spheroid in the Stokes limit ($Re = 0$), in simple shear flow, was first studied by Jeffery, who showed that a spheroid rotates along closed orbits (termed Jeffery orbits hereafter) in such a flow, with the particular orbit being determined by the spheroid initial orientation; the shape of the orbits is a function of κ. The orbits are characterized by an orbit constant C which ranges from 0 to ∞; the limiting orbits $C = 0$ and ∞ correspond, respectively, to a spinning motion of the spheroid with its symmetry axis along the ambient vorticity, and a tumbling motion in the flow-gradient plane with the symmetry axis orthogonal to the ambient vorticity; the general finite-C orbit corresponds to a three-dimensional precessing motion. Hinch and Leal [8] showed that spheroids continue to rotate along Jeffery orbits in planar linear flows provided λ is below a critical value (λ_c) that is a function of the spheroid aspect ratio; $\lambda_c = 1/\kappa^2$ for prolate spheroids and $\lambda_c = \kappa^2$ for oblate spheroids. As indicated in fig. 3.1, we interpret the spheroid orientation dynamics in terms of the trajectories traced by its orientation vector on the unit sphere. From a dynamical systems perspective, $\lambda = \lambda_c$ correspond to a qualitative change of the trajectory topology on the unit sphere. From symmetry considerations, and regardless of κ or λ, the

pair of intersections of the vorticity axis with this unit sphere are fixed points. For $\lambda < \lambda_c$, these fixed points are centers, with the closed orbits around them being the aforementioned Jeffery orbits, the largest of them corresponding to the great circle in which the flow-gradient plane intersects the unit sphere. For $\lambda > \lambda_c$, the closed orbits open up via a saddle-node bifurcation in the flow-gradient plane which leads to two pairs of (diametrically opposite) stable and unstable nodes, as required by symmetry of the linear flow; additionally, the vorticity-axis fixed points transform to saddles, as is also required from the conservation of the Euler characteristic (equal to two for the unit sphere). At $\lambda = \lambda_c$, one has a degenerate scenario with the trajectories having a meridional character, and there being a great circle of (parabolic) fixed points. The bifurcations on each side of λ_c have been shown in Fig. 3.2.

The orientation dynamics in the Stokesian realm for $\lambda < \lambda_c$, as described above, leads to a degenerate scenario owing to the Jeffery orbit of a given spheroid determined by its initial orientation, and the suspension bulk properties being therefore determined by its initial preparation. The Stokesian orientation dynamics therefore does not lead to a unique orientation distribution across the Jeffery orbits. In order to address this problem, Marath and Subramanian [9] considered the effect of weak fluid inertia on the orientation of spheroids and thus obtained the leading order inertial correction to Jeffery's Stokesian formulation (eq.3.15). The authors show that, as a consequence of fluid inertia, the original Jeffery orbits open up. For small but finite Re, a weakly inertial spheroid exhibits a slow drift across these orbits. Under the assumption that the time scale of this inertial drift is asymptotically long compared to the Jeffery period, the authors formulate a one-dimensional description with the only dynamical variable being the orbit constant (C). The sign of the orbital drift (dC/dt) dictates the stability of the spinning and tumbling modes. Thus, $dC/dt < 0 (> 0) \forall C$ corresponds to the spinning (tumbling) mode being stabilized for long times. The sign of dC/dt thereby allowed the authors to demarcate regions in the relevant parameter space (the $\lambda - \kappa$ plane) where the spheroids may undergo spinning or tumbling motions. The authors also identified regions in the $\lambda - \kappa$ plane where dC/dt changes sign across a critical C ($C = C^*$, say), so that the unit sphere is now divided into distinct basins of attraction corresponding to the spinning and tumbling modes, with the basins of attraction demarcated by a pair of unstable (repelling) limit cycles that, at leading order, are Jeffery orbits corresponding to $C = C^*$. Thus, initial orientations corresponding to $C < C^*$ asymptote to spinning motion for long times, while those for $C > C^*$ asymptote to a tumbling motion. Fig. 3.3 summarizes the spinning-tumbling transitions in the $\lambda - \kappa$ plane, based on the one-dimensional orbit constant analysis. The unit sphere trajectory topology pattern corresponding to these bifurcations is shown in fig. 3.4.

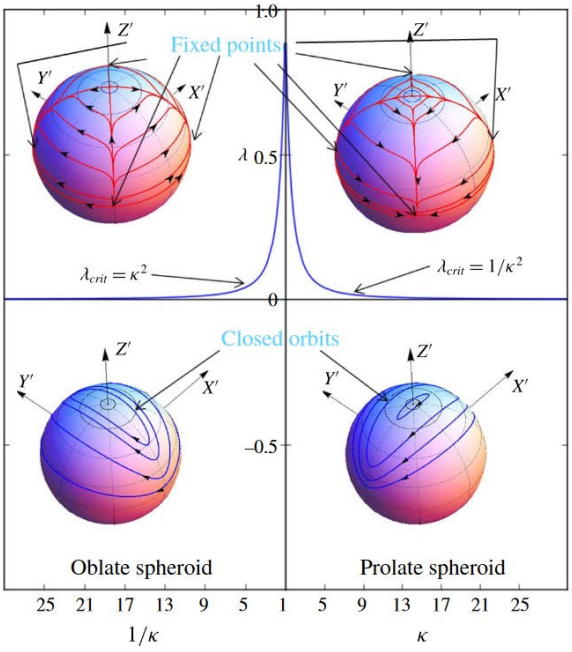

Fig. 3.2 The unit-sphere trajectory topology, for spheroids in a planar linear flow, for $Re = 0$: oblate spheroids (left) and prolate spheroids (right). The trajectories transition from closed orbits to open trajectories across λ_c ($= \kappa^2$ for oblate and $1/\kappa^2$ for prolate spheroids). Figure taken from [9].

This one-dimensional dynamical picture, however, relies on the assumption of the drift time being much longer than the Jeffery time - an assumption that invariably breaks down in the vicinity of λ_c owing to the divergence of the Jeffery period (this divergence is accompanied by the transition of the closed orbits to an increasingly meridional character). The one-dimensional formulation, therefore, cannot resolve the detailed bifurcation scenarios close to λ_c and one needs to consider the original two-dimensional system comprising the equations for the two Jeffery angles. These angles are θ, the polar angle of the spheroid axis with respect to the ambient vorticity, and ϕ, the angle between the spheroid axis projected onto the flow-gradient plane and the flow direction. The analysis of the sequence of bifurcations characterizing (θ, ϕ), that replaces the critical curves $\lambda = \kappa^2$ and $1/\kappa^2$ in the one-dimensional formulation, forms the subject of this chapter. In what follows, we present the fixed point analysis for Jeffery's equations (eq. 3.1) which govern the orientation dynamics of spheroids in inertialess flows. Next, we analyze the equations originally derived by Marath and Subramanian (2018) which account for the effect of weak fluid inertia. (eq. 3.15).

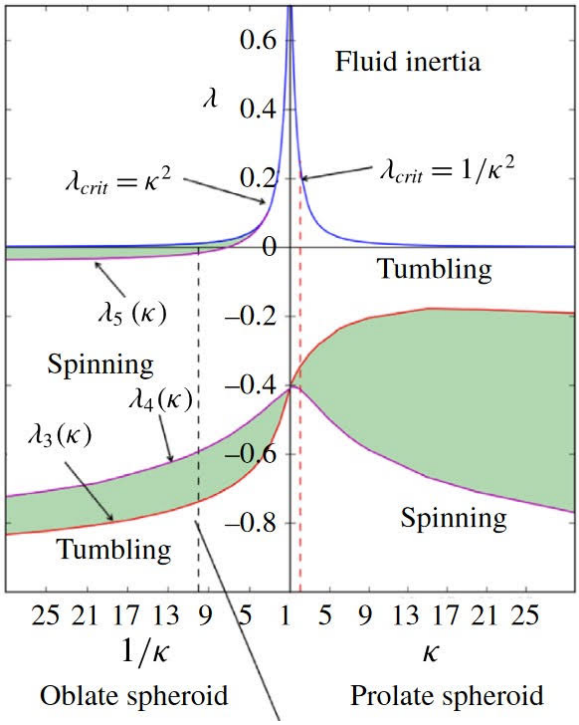

Fig. 3.3 The one-dimensional bifurcation scenario, for a spheroid in a planar linear flow, for small but finite *Re*. Figure taken from [9]. The global trajectory patterns corresponding to the different regimes are shown in fig. 3.4

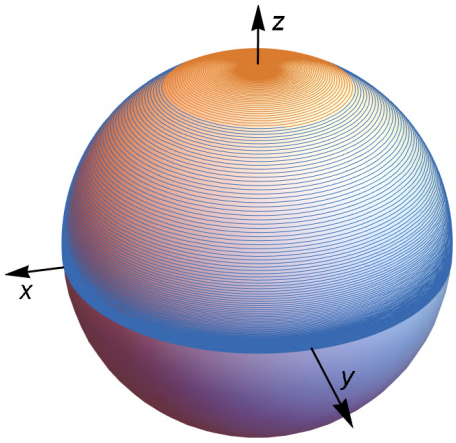

(a) $\lambda = -0.90$. All trajectories (only one shown) spiral towards the flow gradient plane - Tumbling

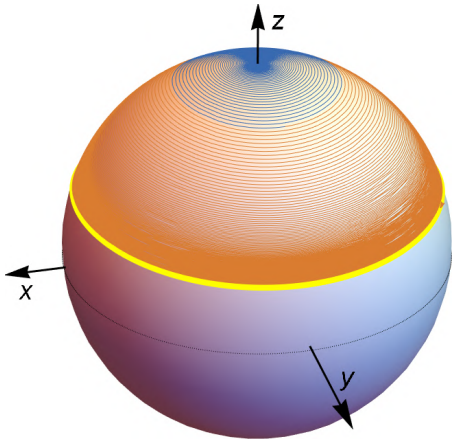

(b) $\lambda = -0.71$. A repeller (Jeffery orbit with C = ∞, shown in yellow) exists on the unit hemisphere.

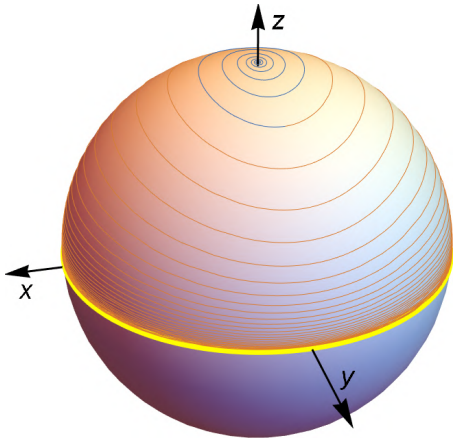

(c) $\lambda = -0.40$. All trajectories (only one shown) spiral towards the vorticity axis - Spinning

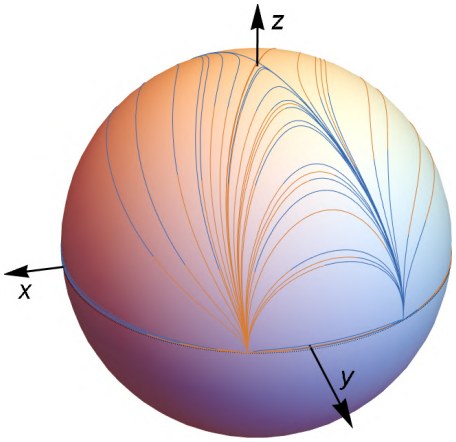

(d) $\lambda = 0.20$. A bifurcation in the flow gradient plane creates a pair of stable / unstable nodes while simultaneously, a saddle is generated at the vorticity axis.

Fig. 3.4 Bifurcation scenarios for an oblate spheroid obtained by Marath and Subramanian [9] discussed in fig. 3.3. Here $\kappa = 0.05$, the flow-gradient plane is the $x-y$ plane while z-axis is the vorticity axis. The figure depicts the trajectory topology on the unit sphere as one moves along a vertical line in the $\lambda - \kappa$ plane; λ increases from -1 towards 1, with $\kappa = 0.05$ (an oblate spheroid). The X, Y and Z axes in the plots above denote the flow, flow-gradient and vorticity directions, respectively. Each trajectory is composed of a blue and an orange section. The blue part represents evolution of the initial condition forward in time while the orange part denotes backward time evolution. The initial condition used for the trajectory lies therefore at the junction of blue and orange sections.

3.2 Trajectory topology for $Re = 0$ (the Stokes case)

The Jeffery equations, valid for spheroids in inertialess linear flows, may be written as

$$\begin{aligned}\dot{\theta} &= \left(\frac{1+\lambda}{4}\right)\frac{\kappa^2-1}{\kappa^2+1}\sin 2\theta \sin 2\phi \\ \dot{\phi} &= -\left(\frac{1-\lambda}{2}\right) + \left(\frac{1+\lambda}{2}\right)\frac{\kappa^2-1}{\kappa^2+1}\cos 2\phi\end{aligned} \tag{3.1}$$

Regardless of κ or λ, the fixed points of this system lie either on the vorticity axis or on the flow-gradient plane. We first look at the fixed points in the flow-gradient plane.

3.2.1 Oblate Spheroids

Fixed points in the flow-gradient plane

We begin with the flow-gradient plane analysis corresponding to $\theta = \pi/2$. As mentioned earlier, the Stokesian trajectory topology is qualitatively altered across $\lambda = \lambda_c$. The fixed points that appear in the flow-gradient plane do so first in the vicinity of $\phi = \pi/2$ (the gradient axis). Thus, we analyze the system 3.1 in the neighborhood of the flow axis, and towards this end, define:

$$\begin{aligned}\hat{\theta} &= \theta - \frac{\pi}{2} \\ \hat{\phi} &= \phi - \frac{\pi}{2}\end{aligned} \tag{3.2}$$

Using these expressions in 3.1, the dynamical system in terms of $\hat{\theta}$ and $\hat{\phi}$ takes the form

$$\begin{aligned}\Rightarrow\dot{\hat{\theta}} &= \alpha \sin 2\hat{\theta}\sin 2\hat{\phi} \\ \dot{\hat{\phi}} &= -\left(\frac{1-\lambda}{2}\right) - 2\alpha\cos 2\hat{\phi}\end{aligned} \tag{3.3}$$

where $\alpha = \frac{1+\lambda}{4}\left(\frac{\kappa^2-1}{\kappa^2+1}\right)$. Note that $\hat{\theta}$,$\hat{\phi} \ll 1$ in the neigbourhood of the flow axis. Setting $\dot{\hat{\theta}} = 0$ gives (trivially) $\hat{\theta} = 0$, whereas, using the small $\hat{\phi}$ form for $\cos 2\hat{\phi}$ in $\dot{\hat{\phi}} = 0$ gives

$$\hat{\phi} = \pm\left(\frac{4\alpha + 1 - \lambda}{8\alpha}\right)^{1/2}$$

Therefore, $\hat{\phi}$ is real if

$$\begin{aligned}
&\left(\frac{4\alpha+1-\lambda}{8\alpha}\right) > 0 \\
\Rightarrow &\frac{\kappa^2-\lambda}{(1+\lambda)(\kappa^2-1)} > 0 \qquad \text{(substituting for } \alpha\text{)} \\
&\Rightarrow \kappa^2-\lambda < 0 \qquad (\because \kappa < 1 \text{ for oblate spheroids}) \\
&\Rightarrow \lambda > \kappa^2
\end{aligned}$$

Therefore, there exists a critical value of λ given by $\lambda_c = \kappa^2$ beyond which there emerge a pair of fixed points in the flow-gradient plane via a saddle-node bifurcation. These are given by

$$\hat{\phi}_{1,2} = \pm\left(\frac{\kappa^2-\lambda}{(1+\lambda)(\kappa^2-1)}\right)^{1/2} \tag{3.4}$$

Since $\hat{\phi} = \phi - \pi/2$, the original ϕ coordinates are given by

$$\Rightarrow \phi_{1,2} = \frac{\pi}{2} \pm \left(\frac{\kappa^2-\lambda}{(1+\lambda)(\kappa^2-1)}\right)^{1/2} \tag{3.5}$$

The two fixed points, therefore, emerge on either side of $\phi = \pi/2$. In order to determine the nature of these fixed points, consider another transformation

$$\begin{aligned}
\tilde{\phi} &= \hat{\phi} - \hat{\phi}_0 \\
\tilde{\theta} &= \hat{\theta}
\end{aligned} \tag{3.6}$$

where $\hat{\phi}_0 = \hat{\phi}_{1,2}$ corresponds to either of the flow-gradient fixed points. In the neighbourhood of the fixed point, we have $\tilde{\theta} \ll 1$ and $\tilde{\phi} \ll \hat{\phi}_0 \ll 1$. Using eq. (3.6) in eq. (3.3), at linear order, we have

$$\begin{bmatrix} \dot{\tilde{\theta}} \\ \dot{\tilde{\phi}} \end{bmatrix} = \begin{bmatrix} 4\alpha\hat{\phi}_0 & 0 \\ 0 & 8\alpha\hat{\phi}_0 \end{bmatrix} \begin{bmatrix} \tilde{\theta} \\ \tilde{\phi} \end{bmatrix} \tag{3.7}$$

The eigenvalues of the matrix are simply the diagonal entries in this case. Since $\alpha = \frac{1+\lambda}{4}\left(\frac{\kappa^2-1}{\kappa^2+1}\right)$ is a negative quantity (owing to the fact that $\kappa < 1$ for oblate spheroids), the eigenvalues are either both negative when $\hat{\phi}_0 > 0$ or both positive if $\hat{\phi}_0 < 0$. It follows that $(\theta,\phi) \equiv (\frac{\pi}{2} + \frac{\kappa^2-\lambda}{(1+\lambda)(\kappa^2-1)})$ is a stable node and $(\theta,\phi) \equiv (\frac{\pi}{2} - \frac{\kappa^2-\lambda}{(1+\lambda)(\kappa^2-1)})$ is an unstable node. Owing to the symmetry of the linear flow configuration, there must exist another stable/unstable node pair on the diametrically opposite end of the great circle in which the unit sphere intersects the flow-gradient plane, yielding a total of four fixed-points in this

plane. In summary, no fixed points exist in the flow gradient plane below critical λ ($\lambda_c = \kappa^2$) while beyond it, there exists two pairs of stable and unstable nodes diametrically opposite to each other.

Fixed points on the vorticity axis

In a similar manner, we can characterize the behaviour of the fixed points on the vorticity axis. We begin with the system of equations 3.1 and proceed to linearize in the neighbourhood of the vorticity axis fixed point, $\theta = 0$. In the neighbourhood, one has $\theta \ll 1$ but $0 \leq \phi < 2\pi$ prohibiting a linearization in ϕ. The governing equations, in the limit of small θ then become

$$\begin{aligned} \dot{\theta} &= \left(\frac{1+\lambda}{4}\right)\frac{\kappa^2-1}{\kappa^2+1} 4\theta \sin\phi\cos\phi \\ \dot{\phi} &= -\left(\frac{1-\lambda}{2}\right) + \left(\frac{1+\lambda}{2}\right)\frac{\kappa^2-1}{\kappa^2+1}\cos 2\phi \end{aligned} \tag{3.8}$$

Using the Cartesian relations for small θ

$$\begin{aligned} x &= \theta\cos\phi \\ y &= \theta\sin\phi \end{aligned} \tag{3.9}$$

transforms eq. (3.8) to

$$\begin{bmatrix} \dot{x} \\ \dot{y} \end{bmatrix} = \begin{bmatrix} 0 & \left(\frac{\kappa^2-\lambda}{\kappa^2+1}\right) \\ \left(\frac{\lambda\kappa^2-1}{\kappa^2+1}\right) & 0 \end{bmatrix} \begin{bmatrix} x \\ y \end{bmatrix} \tag{3.10}$$

In Cartesian terms, the vorticity-axis fixed point is given by $(0,0)$ and the associated eigenvalues are

$$E_{1,2} = \pm\left[\left(\frac{\kappa^2-\lambda}{\kappa^2+1}\right)\left(\frac{\lambda\kappa^2-1}{\kappa^2+1}\right)\right]^{1/2} \tag{3.11}$$

For $\lambda < \kappa^2$, the eigenvalues are imaginary and the fixed point is a center, whereas, for $\lambda > \kappa^2$, the eigenvalues are real with opposite signs and the fixed point is therefore a saddle. Owing to the symmetry of the configuration, an identical fixed point exists at the diametrically opposite end of the unit sphere.

One may now summarize the bifurcation scenario for an oblate spheroid in the Stokes limit. For $\lambda < \kappa^2$, there exist only the two vorticity-axis fixed points, both of which are centers, with Jeffery orbits occupying the remainder of the unit sphere. As λ increases beyond κ^2, the vorticity axis centers transform to saddles while four fixed points (two pairs of stable/unstable nodes) emerge simultaneously in the flow gradient plane via saddle-node

bifurcations at $\phi = \pi/2$ and $3\pi/2$. Note that, when $\lambda < \lambda_c$, the two centers have a fixed point index of 1 each. For $\lambda > \lambda_c$, the two saddles have a fixed point index of -1 each while the index is unity for each of the four nodes in the flow-gradient plane, thereby adding up to 2. The Euler characteristic of the sphere, which is the sum of the indices of all fixed points on the sphere, is thereby preserved on either side of the bifurcation, as must be the case, being a topological invariant.

3.2.2 Prolate Spheroid

Fixed points in the flow-gradient plane

In a manner similar to the oblate spheroid, we can obtain the bifurcation scenario for the prolate case. We begin with eq. 3.1 and again restrict ourselves to the flow-gradient plane ($\theta = \pi/2$) to begin with. Then, $\dot{\theta} = 0$ is immediately satisfied and imposing $\dot{\phi} = 0$ yields

$$\phi_0 = \pm \left(\frac{\lambda \kappa^2 - 1}{(1+\lambda)(\kappa^2 - 1)} \right)^{1/2} \tag{3.12}$$

which is real if $\lambda > 1/\kappa^2$. Therefore, two critical points emerge on the flow-gradient plane, in the vicinity of the flow axis, as λ exceeds the critical lambda $\lambda_c = 1/\kappa^2$. In order to analyze the fixed points, we linearize the system after using the transformation

$$\begin{aligned} \hat{\theta} &= \theta - \pi/2 \\ \hat{\phi} &= \phi - \phi_0 \end{aligned} \tag{3.13}$$

where $\hat{\theta}, \hat{\phi} \ll 1$. As for the oblate spheroids, note that the linearization requires $\hat{\phi} \ll \phi_0 \ll 1$, which becomes increasingly restrictive in the vicinity of the bifurcation ($\lambda = 1/\kappa^2$). In the transformed coordinates, one obtains the system of equations as

$$\Rightarrow \begin{bmatrix} \dot{\hat{\theta}} \\ \dot{\hat{\phi}} \end{bmatrix} = \begin{bmatrix} -(1+\lambda)\frac{\kappa^2-1}{\kappa^2+1}\phi_0 & 0 \\ 0 & -2(1+\lambda)\frac{\kappa^2-1}{\kappa^2+1}\phi_0 \end{bmatrix} \begin{bmatrix} \hat{\theta} \\ \hat{\phi} \end{bmatrix} \tag{3.14}$$

The eigenvalues, being simply the diagonal entries, indicate that the fixed point with negative ϕ value in 3.12 acts as an unstable node while that with positive ϕ value is a stable node. Symmetry considerations imply that identical fixed points must exist at diametrically opposite points on the sphere. Therefore, the saddle-node bifurcation results in four fixed points in the flow gradient plane - two pairs of stable and unstable nodes.

Fixed points on the vorticity axis

The vorticity axis analysis for the prolate case remains identical to that of oblate, allowing us to describe the complete bifurcation scenario. If $\lambda < 1/\kappa^2$, two centers exist on the vorticity axis which transform to saddles as λ increases beyond $1/\kappa^2$. Simultaneously, a saddle-node bifurcation in the flow-gradient plane gives rise to two pairs of stable/unstable nodes. The difference being, that the fixed points emerge on either side of $\phi = 0$ and $\phi = \pi$ as opposed to $\phi = \pi/2$ and $3\pi/2$ for the oblate spheroid.

This completes the analysis of the orientation dynamics of spheroids in planar linear flows, in the Stokes limit, where the trajectory topology on the unit sphere is seen to be qualitatively altered across $\lambda = \kappa^2$ and $1/\kappa^2$ for oblate and prolate spheroids, respectively.

3.3 Trajectory topology for small but finite *Re*

Equations governing the orientation of a spheroid, in planar linear flow with weak fluid inertial effects (small but finite *Re*), as first obtained by Marath and Subramanian [9] are

$$\begin{aligned}
\dot{\theta} =& \left(\frac{1+\lambda}{4}\right)\frac{\kappa^2-1}{\kappa^2+1}\sin 2\theta \sin 2\phi \quad + \\
& Re \sin\theta\cos\theta\Big[F_1^f(\xi_0,\lambda) + F_2^f(\xi_0,\lambda)\cos 2\phi + F_3^f(\xi_0,\lambda)\cos 2\theta + \\
& F_4^f(\xi_0,\lambda)\cos 4\phi + F_5^f(\xi_0,\lambda)\cos(2\theta - 4\phi) + F_6^f(\xi_0,\lambda)\cos(2\theta + 4\phi)\Big] \\
\dot{\phi} =& -\left(\frac{1-\lambda}{2}\right) + \left(\frac{1+\lambda}{2}\right)\frac{\kappa^2-1}{\kappa^2+1}\cos 2\phi \quad + \\
& Re \sin\phi\cos\phi\Big[G_1^f(\xi_0,\lambda) + G_2^f(\xi_0,\lambda)\cos 2\theta + G_3^f(\xi_0,\lambda)\cos 2\phi + \\
& G_4^f(\xi_0,\lambda)\cos(2\theta)\cos(2\phi)\Big]
\end{aligned} \tag{3.15}$$

where $F_i^f(\xi_0,\lambda)$'s and $G_i^f(\xi_0,\lambda)$'s are as defined in [9].

3.3.1 Oblate Spheroid

Fixed-points in the flow-gradient plane

To begin with, our focus is on fixed points in the flow-gradient plane, and towards this end, we assume $(\theta,\phi) \equiv (\pi/2, \phi_0)$. Using this leads to the following transcendental equation governing ϕ_0

$$-\left(\frac{1-\lambda}{2}\right)+2\alpha\cos 2\phi_0+Re\sin\phi_0\cos\phi_0\left[G_1^f-G_2^f+G_3^f\cos 2\phi_0-G_4^f\cos 2\phi_0\right]=0$$

Keeping in mind that the saddle-node bifurcation in the Stokesian case occurs at $\phi_0=\pi/2$ (when $\lambda=\kappa^2$), one expects the solution of the transcendental equation to be close to $\pi/2$ for small Re. Thus, we set $\phi_0=\pi/2+\hat{\phi}_0$, with $\hat{\phi}_0\ll 1$, whence one obtains

$$\Rightarrow-\left(\frac{1-\lambda}{2}\right)-2\alpha(1-2\hat{\phi}_0^2)-Re\hat{\phi}_0\left[G_1^f-G_2^f-G_3^f\cos 2\hat{\phi}_0+G_4^f\cos 2\hat{\phi}_0\right]=0$$
$$\Rightarrow-\left(\frac{1-\lambda}{2}\right)-2\alpha(1-2\hat{\phi}_0^2)-Re\hat{\phi}_0\left[G_1^f-G_2^f-G_3^f+G_4^f\right]=0$$

using the small $\hat{\phi}$ form for $\cos 2\hat{\phi}$. The above quadratic equation is readily solved, and yields the following roots

$$\hat{\phi}_{01,02}=\frac{Re\mathscr{G}\pm\left(Re^2\mathscr{G}^2+4(1+\lambda)\frac{\kappa^2-1}{\kappa^2+1}\frac{\kappa^2-\lambda}{\kappa^2+1}\right)^{1/2}}{2(1+\lambda)\frac{\kappa^2-1}{\kappa^2+1}} \tag{3.16}$$

where $\mathscr{G}(\xi_0,\lambda)=G_1^f(\xi_0,\lambda)-G_2^f(\xi_0,\lambda)-G_3^f(\xi_0,\lambda)+G_4^f(\xi_0,\lambda)$. We thus obtain the azimuthal coordinates of the fixed points in the flow gradient plane. Note that the point of emergence of the fixed points is no longer at $\phi=\pi/2$, as was the case without fluid inertia. The fixed points now emerge at

$$\phi_{01}=\phi_{02}=\frac{\pi}{2}+\frac{Re\mathscr{G}}{2(1+\lambda)\frac{\kappa^2-1}{\kappa^2+1}}$$

The final coordinates of the fixed points are therefore

$$\phi_{01,02}=\frac{\pi}{2}+\frac{Re\mathscr{G}}{2(1+\lambda)\frac{\kappa^2-1}{\kappa^2+1}}\pm\frac{\left(Re^2\mathscr{G}^2+4(1+\lambda)\frac{\kappa^2-1}{\kappa^2+1}\frac{\kappa^2-\lambda}{\kappa^2+1}\right)^{1/2}}{2(1+\lambda)\frac{\kappa^2-1}{\kappa^2+1}} \tag{3.17}$$

Fluid inertia, therefore, shifts the points of emergence away from the gradient axis by an amount of $O(Re\mathscr{G})$. Furthermore, the coordinates of the fixed points are real when

$$Re^2\mathscr{G}^2 + 4(1+\lambda)\frac{\kappa^2-1}{\kappa^2+1}\frac{\kappa^2-\lambda}{\kappa^2+1} \geq 0$$

This gives us a criterion for the flow-gradient bifurcation leading to the emergence of $\phi_{01,02}$. Let's say that the critical value of λ required for this bifurcation is λ_{FG1}, then it's given by the equation

$$Re^2\mathscr{G}^2(\xi_0,\lambda_{FG1}) + 4\frac{(1+\lambda_{FG1})(\kappa^2-1)(\kappa^2-\lambda_{FG1})}{(\kappa^2+1)^2} = 0 \tag{3.18}$$

Knowing the coordinates of the fixed points ($\hat{\phi}_{01,02}$), we can now linearize the system (about $(\hat{\theta},\hat{\phi}) \equiv (0,0)$) and determine their character. The linearized system becomes

$$\Rightarrow \begin{bmatrix}\dot{\hat{\theta}}\\ \dot{\hat{\phi}}\end{bmatrix} = \begin{bmatrix}(1+\lambda)\frac{\kappa^2-1}{\kappa^2+1}\hat{\phi}_0 - Re\,\mathscr{F} & 0\\ 0 & 2(1+\lambda)\frac{\kappa^2-1}{\kappa^2+1}\hat{\phi}_0 - Re\,\mathscr{G}\end{bmatrix}\begin{bmatrix}\hat{\theta}\\ \hat{\phi}\end{bmatrix} \tag{3.19}$$

where $\mathscr{F} = F_1^f - F_2^f - F_3^f + F_4^f - 2F_5^f$ and $\mathscr{G} = G_1^f - G_2^f - G_3^f + G_4^f$. Setting $Re = 0$ gives back the Stokes case equations (eq. 3.7). Let $E_{1,2}$ be the eigenvalues of the matrix in eq. 3.19. Then

$$E_1 = (1+\lambda)\frac{\kappa^2-1}{\kappa^2+1}\hat{\phi}_0 - Re\,\mathscr{F}(\xi_0,\lambda) \tag{3.20}$$

$$E_2 = 2(1+\lambda)\frac{\kappa^2-1}{\kappa^2+1}\hat{\phi}_0 - Re\,\mathscr{G}(\xi_0,\lambda) \tag{3.21}$$

Here, $\hat{\phi}_0$ is the coordinate of a flow gradient fixed point in the rotated frame (eq. 3.16). Depending on the sign of the eigenvalues either of the two fixed points (corresponding to $\hat{\phi} = \hat{\phi}_{01,02}$), may either be a node or a saddle. Substituting $\phi_{01,02}$ in E_2 and equating it to zero gives back the criterion for λ_{FG1}. Therefore E_2 does not change sign for either of the fixed points. Substituting $\phi_{01,02}$ in E_1 and equating it to zero, yields the following criterion

$$Re^2(\mathscr{G}-2\mathscr{F})^2 - Re^2\mathscr{G}^2 - 4\frac{(1+\lambda_{FG2})(\kappa^2-1)(\kappa^2-\lambda_{FG2})}{(\kappa^2+1)^2} = 0 \tag{3.22}$$

where λ_{FG2} is the critical λ required for the second bifurcation in flow-gradient plane. It can be seen that, $\lambda_{FG2} > \lambda_{FG1}$. Note that the criterion remains the same regardless of whether one substitutes ϕ_{01} or ϕ_{02}. Therefore, depending on the aspect ratio (κ), E_1 may change sign

for either one of the fixed points, and thereby, the fixed point transforms its character. This change of sign occurs for mutually exclusive values of κ i.e. there exists a critical aspect ratio κ_c (≈ 0.328) such that the transformation involves a bifurcation of ϕ_{01} for $\kappa < \kappa_c$ and a bifurcation of ϕ_{02} otherwise.

Based on the fixed point analyses, one may now summarize the fixed point bifurcations in the flow-gradient plane for small but finite *Re*. If $\kappa > 0.328$ and $\lambda < \lambda_{FG1}$, no fixed points exist in the flow gradient plane. As λ increases beyond λ_{FG1}, two fixed points emerge and move apart from each other along the equator. One of these has two positive eigenvalues whereas the other has a positive and a negative eigenvalue. Therefore, a saddle-node (unstable) pair is generated after the first bifurcation. As λ increases beyond λ_{FG2}, both eigenvalues of the saddle become negative and the saddle transforms to a stable node. The flow-gradient plane thus goes from a saddle-node (unstable) pair to a stable-unstable node pair. If $\kappa < 0.328$, a limit cycle exists in each hemisphere. In this case, the first bifurcation in the flow gradient plane results in a saddle-node (stable) pair while the second bifurcation transforms the saddle to an unstable node. The flow-gradient plane thus goes from a saddle-node (unstable) pair to a stable-unstable node pair.

Fixed points on the vorticity axis

We now proceed to analyze the bifurcations on the vorticity axis in a similar manner. Linearizing about $\theta = 0$ yields the system of equations

$$\Rightarrow \begin{bmatrix} \dot{x} \\ \dot{y} \end{bmatrix} = \begin{bmatrix} Re(F_1^f + F_2^f + F_3^f) & \left(\frac{\kappa^2-\lambda}{\kappa^2+1}\right) \\ \left(\frac{\lambda\kappa^2-1}{\kappa^2+1}\right) & Re(F_1^f - F_2^f + F_3^f) \end{bmatrix} \begin{bmatrix} x \\ y \end{bmatrix} \tag{3.23}$$

The eigenvalues ($E_{1,2}$) for this system of equations are given by

$$E_{1,2} = Re(F_1^f + F_3^f) \pm \sqrt{\left(Re^2(F_2^f)^2 + \frac{\kappa^2-\lambda}{\kappa^2+1}\frac{\lambda\kappa^2-1}{\kappa^2+1}\right)} \tag{3.24}$$

which immediately yields two bifurcation scenarios. For λ's less than a critical value (say λ_{V1}), the argument of the square root remains negative and thus the eigenvalues complex. Since $F_1^f(\kappa,\lambda) + F_3^f(\kappa,\lambda)$ remains negative for $0 < \kappa < 1$, the fixed point is a stable spiral for $\lambda < \lambda_{V1}$.

As λ is increased beyond λ_{V1}, one obtains a pair of real and negative eigenvalues. The fixed point therefore transitions from a stable spiral to a stable node. Increasing lambda further (say beyond λ_{V2}) causes one of the eigenvalues to become positive and the fixed point

therefore transitions to a saddle. The criteria for the first bifurcation, therefore, becomes

$$Re^2(F_2^f)^2 + \left(\frac{\kappa^2-\lambda_1}{\kappa^2+1}\right)\left(\frac{\lambda_1\kappa^2-1}{\kappa^2+1}\right) = 0 \tag{3.25}$$

and that for the second bifurcation becomes

$$Re(F_1^f + F_3^f) + \sqrt{Re^2(F_2^f)^2 + \left(\frac{\kappa^2-\lambda_2}{\kappa^2+1}\right)\left(\frac{\lambda_2\kappa^2-1}{\kappa^2+1}\right)} = 0 \tag{3.26}$$

We have thus characterized four bifurcations for the oblate spheroid - two on the flow-gradient plane and two on the vorticity axis (eqs. 3.18 , 3.22, 3.25, 3.26). Fig. 3.5 shows a plot of the threshold flow parameters ($\lambda_{V1}, \lambda_{V2}, \lambda_{FG1}, \lambda_{FG2}$), for the aforementioned bifurcations, as a function of the aspect ratio (κ) for a fixed *Re*. This figure also shows the limit cycle emergence and annihilation curves which are (seemingly) unrelated to the analysis above. The bifurcation thresholds as a function of *Re*, for an oblate spheroid with $\kappa = 0.1$, are shown in fig. 3.6. The sequence of finite-*Re* bifurcations obtained thus far have been schematically illustrated in fig. 3.7 which shows the character of the fixed points generated due to each bifurcation.

Interior fixed points

We now invoke an argument based on the Euler characteristic of the unit sphere (which is a topological invariant, and therefore, conserved regardless of bifurcations in the trajectory topology), to show that between the second flow-gradient plane bifurcation (λ_{FG2}- red curve in fig. 3.7) and the second vorticity axis bifurcation (λ_2- orange curve in fig. 3.7) the fixed points in the flow-gradient plane and those on the vorticity axis cannot by themselves represent a consistent set of fixed points on the unit sphere. It is known that Euler characteristic for a sphere must be 2 and hence the fixed point indices for all fixed points on the unit sphere must add up to two. The fixed point index is 1 for a spiral, 1 for the nodes and -1 for a saddle. Consider the case without a limit cycle. Starting from the first (lowermost) regime in fig. 3.7, the unit sphere consists only of two spirals and the Euler characteristic requirement is immediately satisfied. As λ is increased beyond λ_{V1}, two fixed points appear on the flow gradient plane - a saddle and a node. Due to the symmetry of the configuration, an identical saddle-node pair exists on the diametrically opposite point on the unit sphere. The sum of fixed point indices is therefore 2 (due to spirals) + 2 (due to nodes) - 2 (due to saddles) which adds up to 2. If λ is now increased beyond λ_{FG2}, the Euler characteristic requirement breaks down, as the sum now becomes 2(due to spirals) + 4(due to nodes) which is 6. For

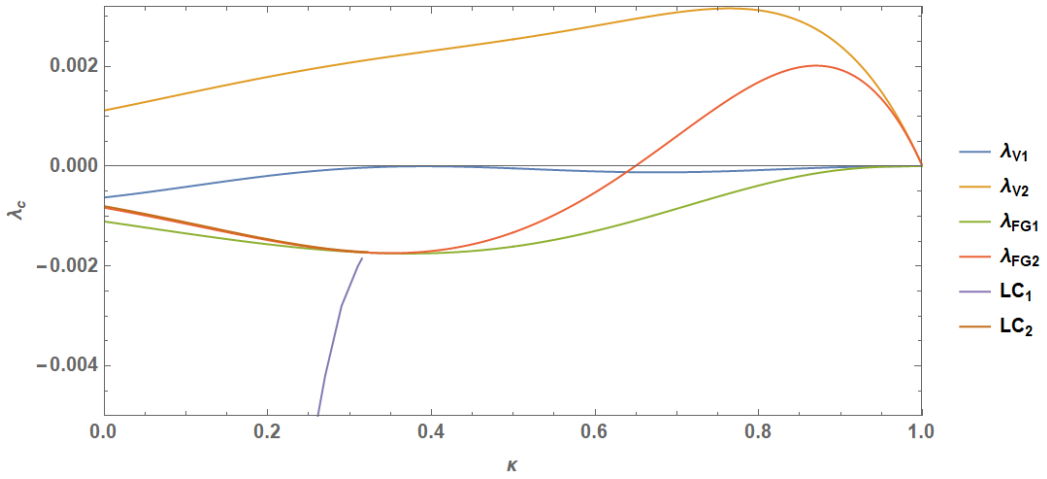

(a) The general sequence of the bifurcation curves.

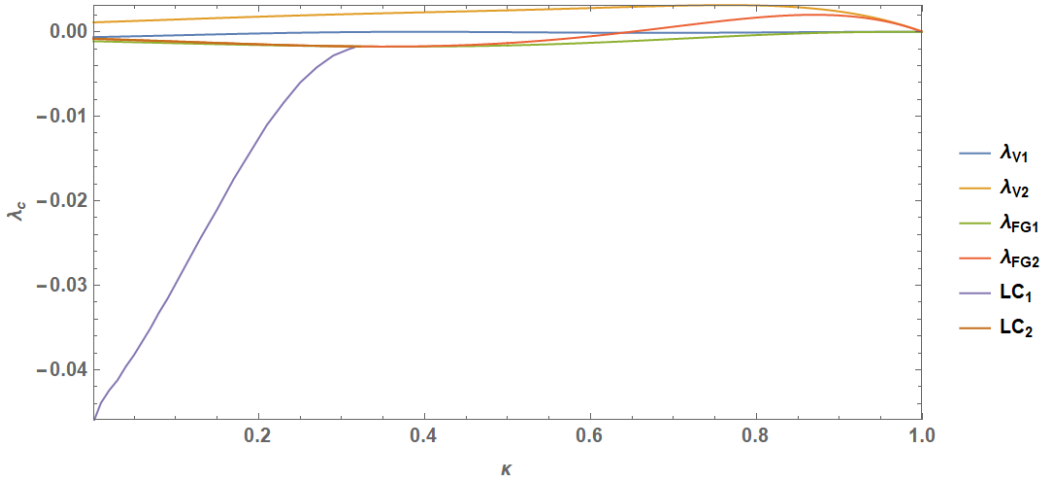

(b) A zoomed out version of 3.5a highlighting the bifurcation corresponding to emergence of the limit cycle ($LC1$).

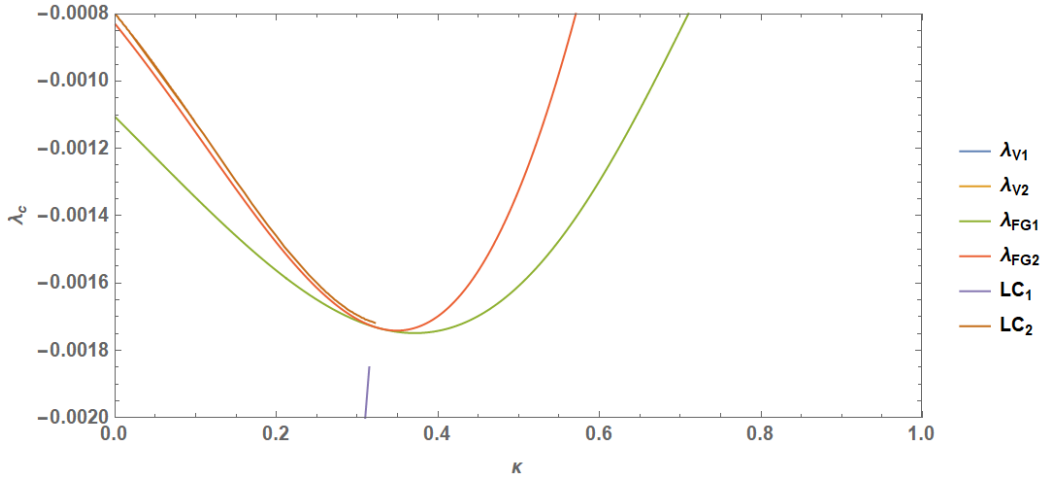

(c) A zoomed in version of 3.5a which focuses on the curve corresponding to the vanishing of the limit cycle ($LC2$).

Fig. 3.5 The variation of the inertial bifurcation thresholds (relative to the Stokesian threshold $\lambda_c = \kappa^2$) of an oblate spheroid with $\kappa = 0.1$, for $Re = 0.5$. The figures show both the bifurcation curves obtained from the fixed point analysis detailed earlier, and the two thresholds corresponding to the emergence and annihilation of the limit cycle.

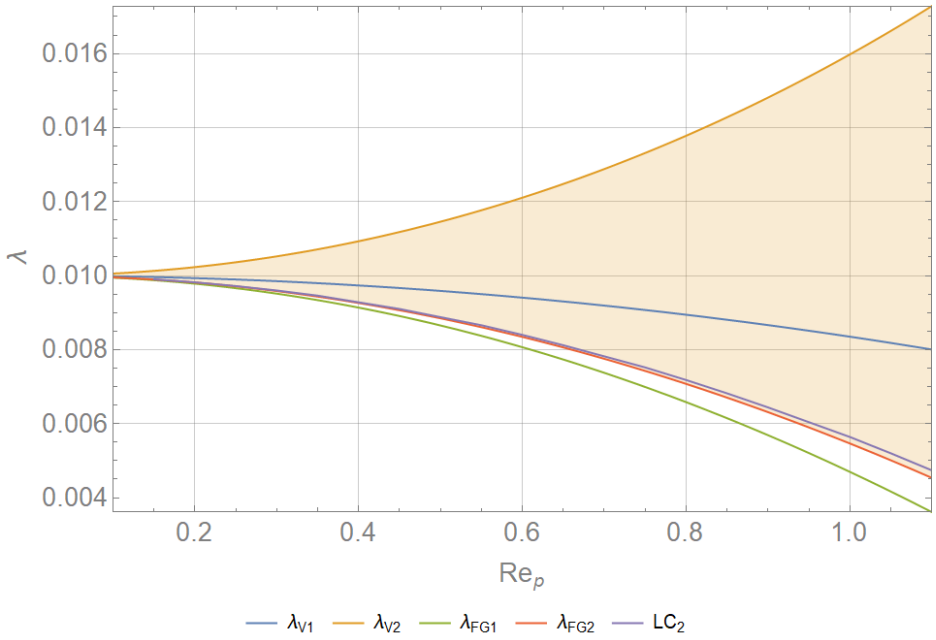

Fig. 3.6 Effect of fluid inertia on the bifurcation thresholds for $\kappa = 0.1$. The Y-axis here denotes the actual value of λ. It can be seen that the four bifurcations merge onto the lone Stokesian threshold ($= \kappa^2$) as $Re \to 0$. With increasing Re, the bifurcation thresholds move farther apart and the bifurcations appear distinct.

$\lambda > \lambda_{FG2}$, one has 4 nodes and 2 saddles and thereby again satisfying the Euler characteristic requirement. A similar argument can also be made regarding the scenario involving a limit cycle (keeping in mind that the fixed point index for a limit cycle is 0). This indicates that, for $\lambda_{FG2} < \lambda < \lambda_{V2}$, the current picture does not encapsulate all fixed points on the unit sphere. There must then exist other fixed points, besides the ones on the flow-gradient plane and the vorticity axis, that our analysis has not yet addressed. We will refer to these as *interior fixed points*. In line with the Euler characteristic requirement, the simplest resolution would be to have a set of four symmetrically located interior saddle points in the parameter space between λ_{FG2} and λ_{V2}. As we will see, this indeed turns out to be the case.

In order to investigate the interior fixed points, the presence of which is implied by the above arguments, we now go beyond fixed point analyses and plot the global trajectory patterns for a fixed Re and aspect ratio (κ), and with varying flow parameter λ. These plots will allows us to validate the bifurcation scenarios predicted from the fixed point analysis and examine additional features that arise due to the presence of the aforementioned interior fixed points. Fig. 3.8 shows a sequence of unit-sphere trajectory topologies for an oblate spheroid with $\kappa = 0.1$, with increasing λ. For illustration purposes, Re has been taken to be 1. The inset on the left shows the four bifurcation regimes determined from the fixed-point

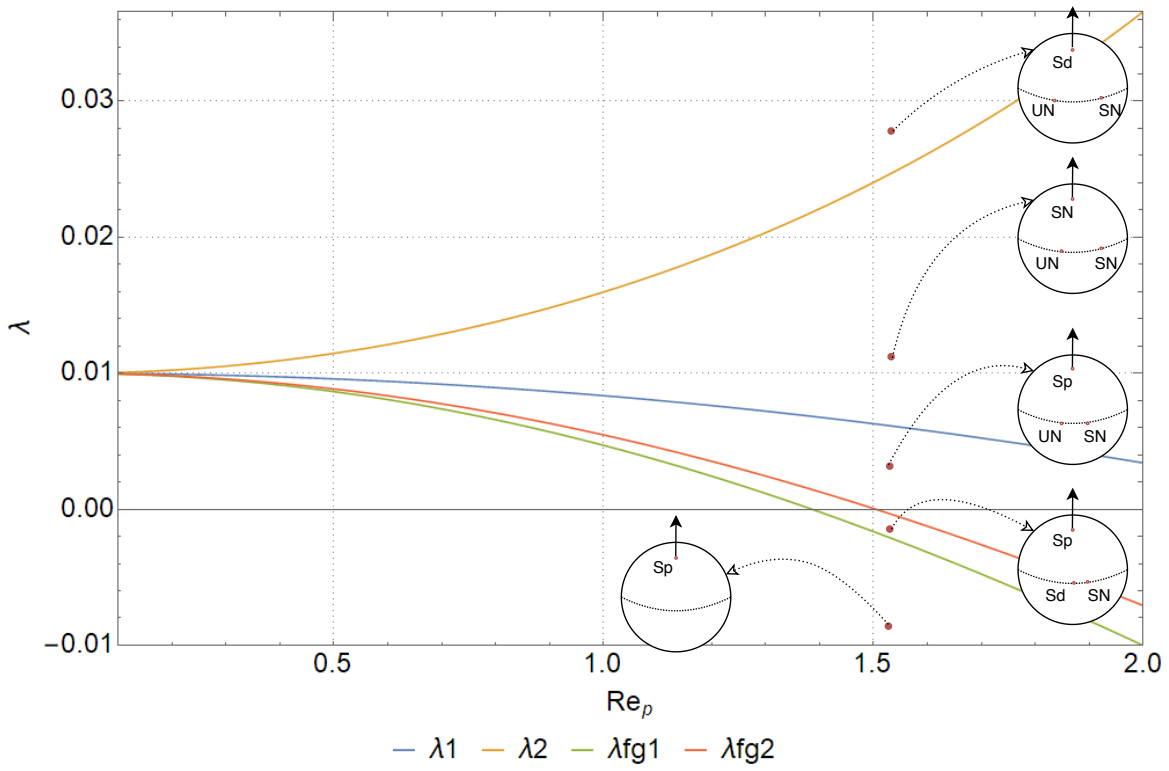

Fig. 3.7 A schematic of the fixed points, on the flow-gradient plane and on the vorticity axis, obtained from the analysis of eq. 3.15 for an oblate spheroid with $\kappa = 0.1$ ($< \kappa_c$). The abbreviations used are as follows: Sp - Spiral, SN - Stable Node, UN - Unstable Node and Sd - Saddle. The fixed point configurations corresponding to the regions between the curves for λ_{FG2} and λ_{V2}, do not have the indices of the fixed points adding up to the sphere Euler characteristic (2). There must therefore exist other interior fixed points besides the ones shown on the vorticity axis and the flow-gradient plane. Note that the fixed point index of a limit cycle is zero. For the sake of clarity, therefore, the curves corresponding to the limit cycle origin and annihilation have not been shown in the above figure.

analysis above, and an additional curve corresponding to the annihilation of the limit cycle. A black point within the inset denotes the current state of the system in the parameter space, and thereby, indicates the bifurcation regime corresponding to each global trajectory plot. The shaded region in the inset indicates the regime where an interior fixed point exists. The figures on the right show the trajectory topology in the neighborhood of the visible fixed points. Beginning with a state already described in [9], we introduce new bifurcations not captured earlier by the one-dimensional model of Marath and Subramanian. The captions emphasize the key features for each plot.

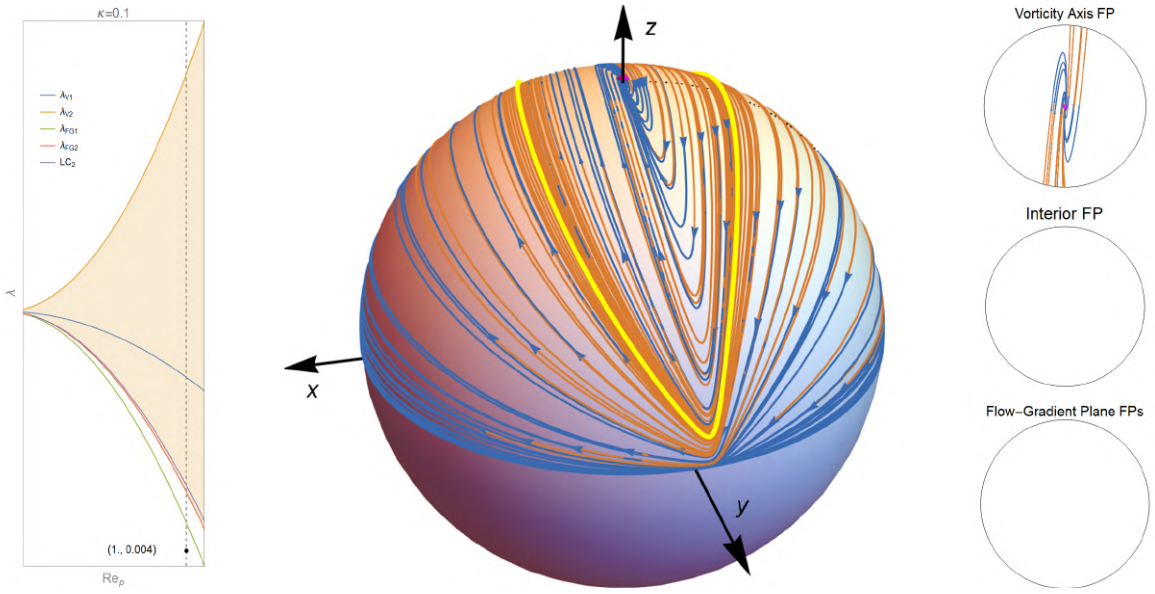

(a) $\lambda = 0.004$. In the current configuration, the system has a stable spiral at the vorticity axis and a repelling limit cycle surrounding it. No fixed points exist in the flow-gradient plane.

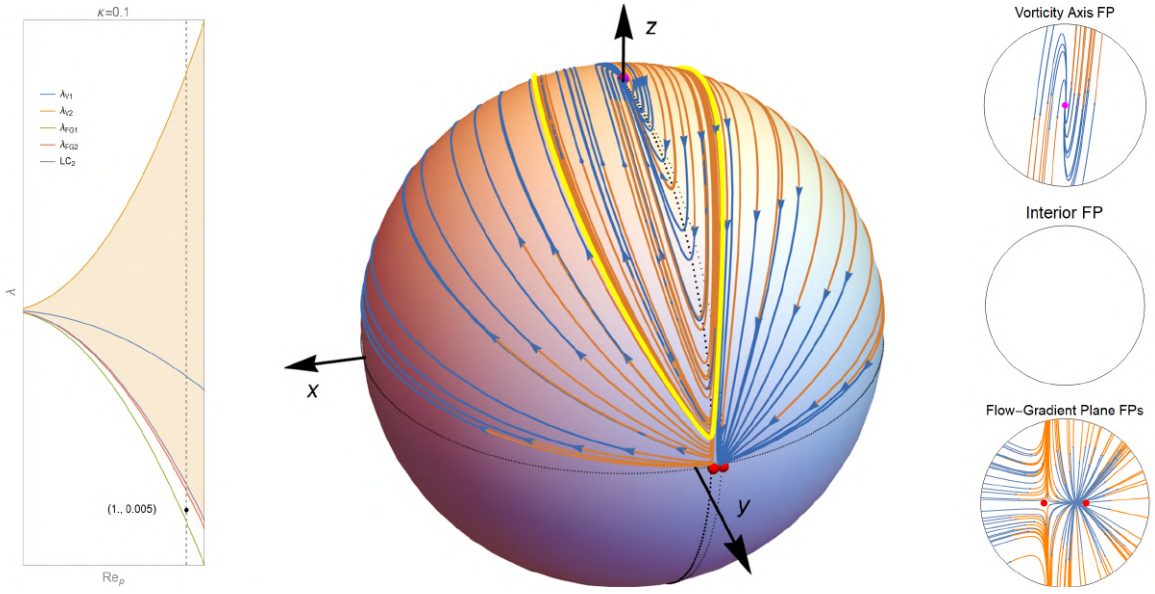

(b) $\lambda = 0.005$. Two fixed points - a stable node and a saddle - marked with red dots emerge in the flow gradient plane as λ is increased beyond λ_{FG1}.

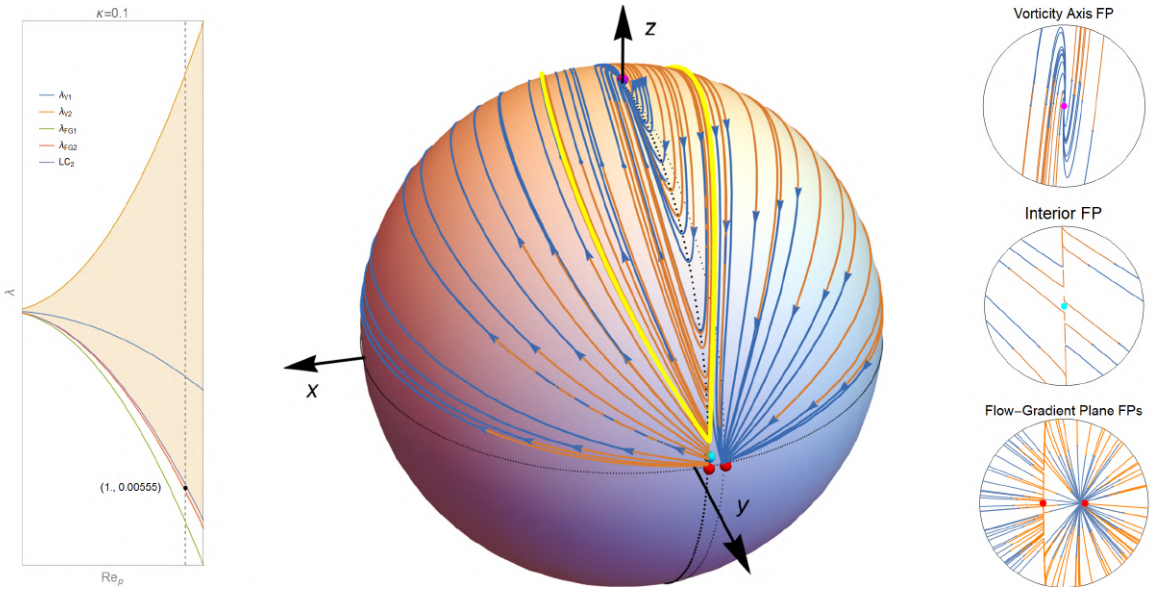

(c) $\lambda = 0.00555$. As λ increases beyond λ_{FG2}, a second flow-gradient bifurcation transforms the saddle (of the original saddle-node pair) into an unstable node, and a new interior fixed point (together with its mirror image as required by symmetry - not visible) emerges along with the above transformation of the fixed point. This interior fixed point is a saddle, as expected, due to the Euler characteristic requirement.

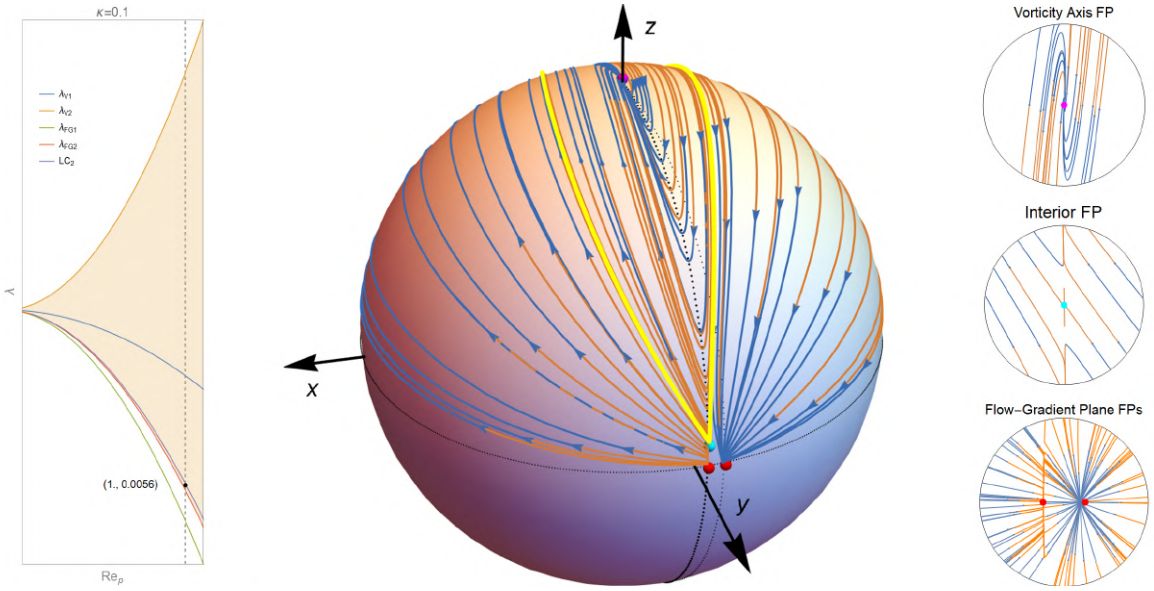

(d) $\lambda = 0.0056$. The interior saddle moves and collides with the repelling limit cycle. Note that an identical collision also occurs on the opposite side of the hemisphere and the repelling limit cycle therefore collides simultaneously with two saddles in a Heteroclinic Bifurcation.

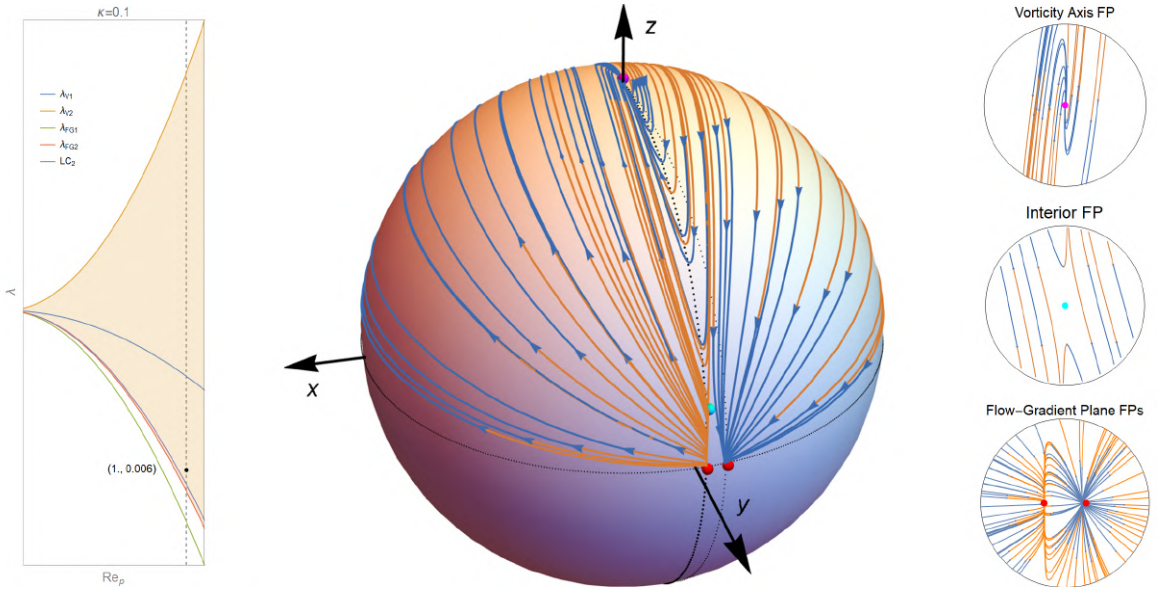

(e) $\lambda = 0.006$. The repellers on both hemispheres are annihilated due to a heteroclinic bifurcation. The interior fixed point remains a saddle. The bifurcation does, however, deviates the interior saddle away from its original meridional trajectory.

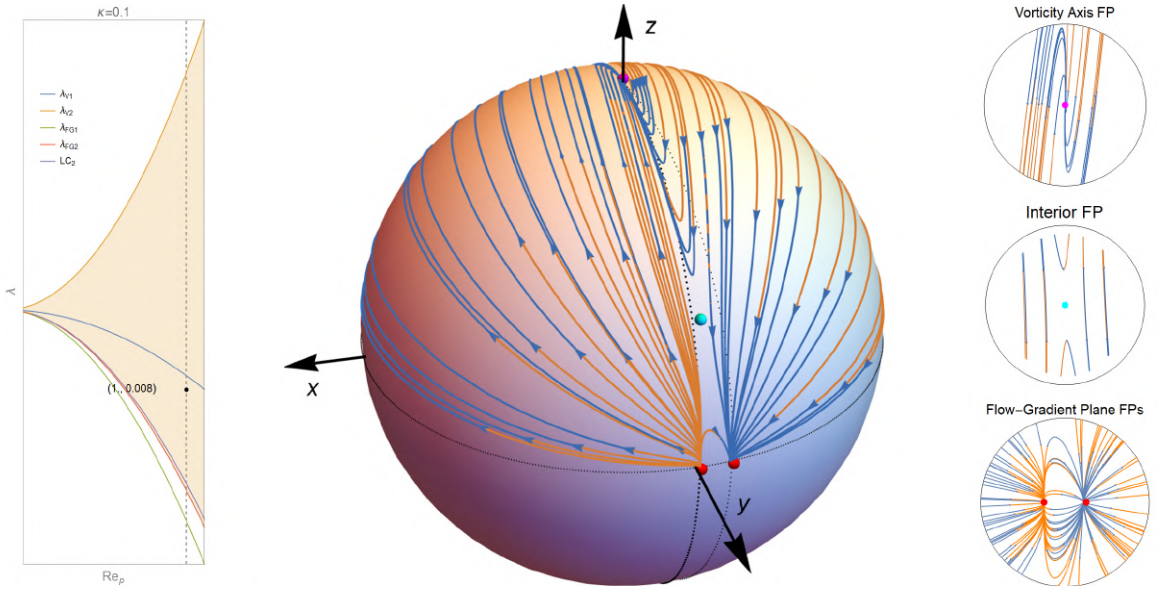

(f) $\lambda = 0.008$. With increasing λ, the fixed points in the flow-gradient plane continue to move apart, while the interior fixed point moves towards the vorticity axis.

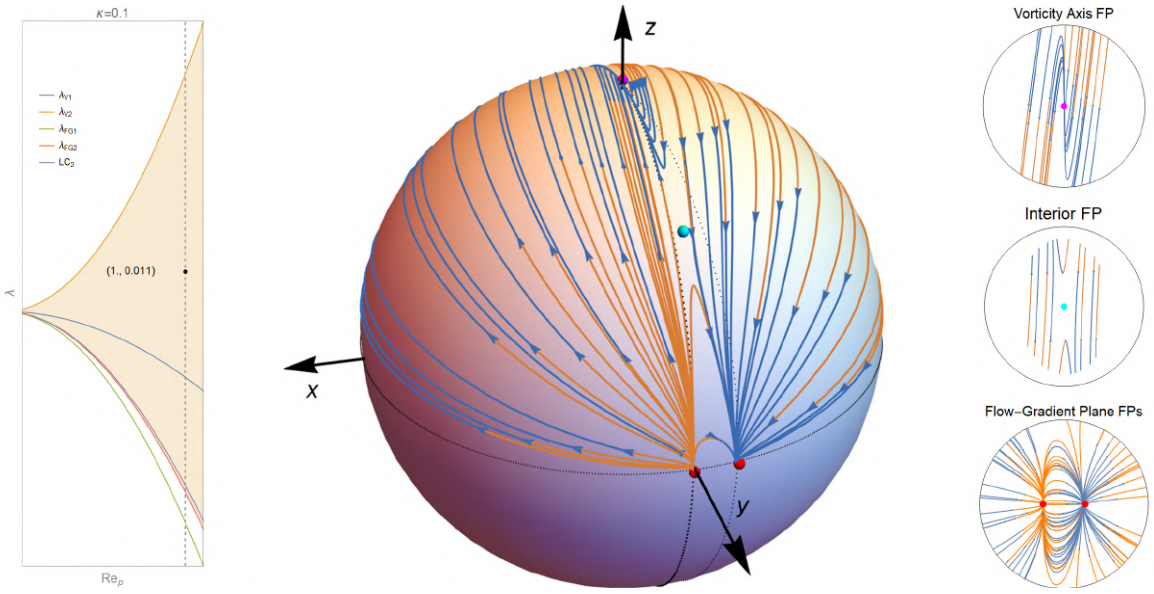

(g) $\lambda = 0.011$. As λ is increased beyond λ_1, the vorticity axis fixed point transitions from a spiral to a node. For small *Re*, this bifurcation is difficult to clarify via the trajectory plots.

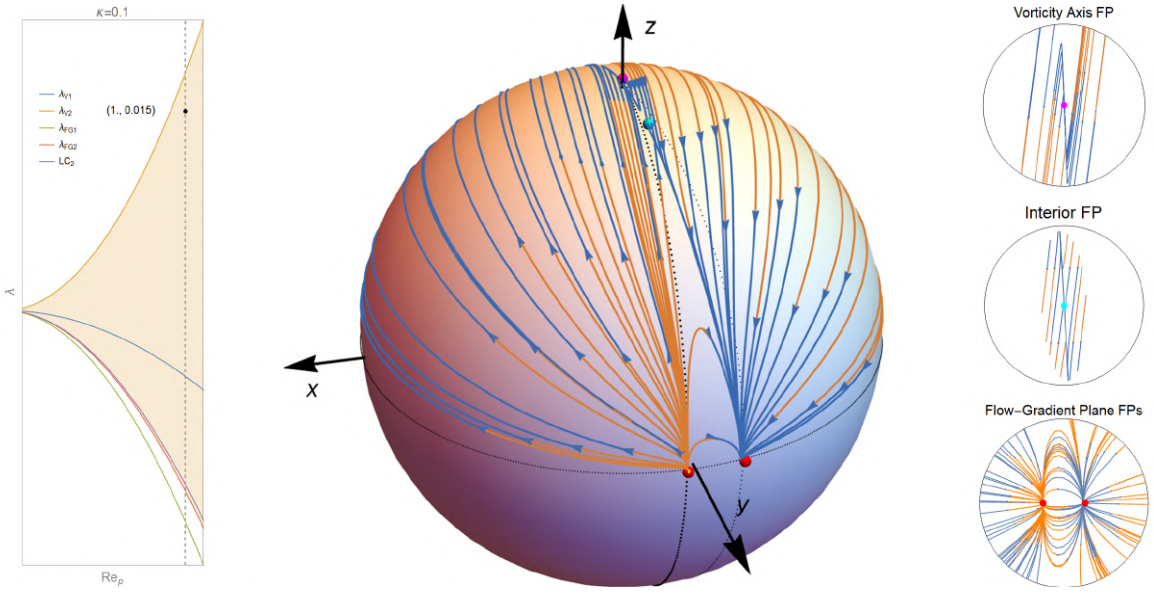

(h) $\lambda = 0.015$. The interior fixed point (a saddle) continues to move toward the vorticity axis. Note, however, that this movement is not along a meridian (drawn as dotted black lines for reference.)

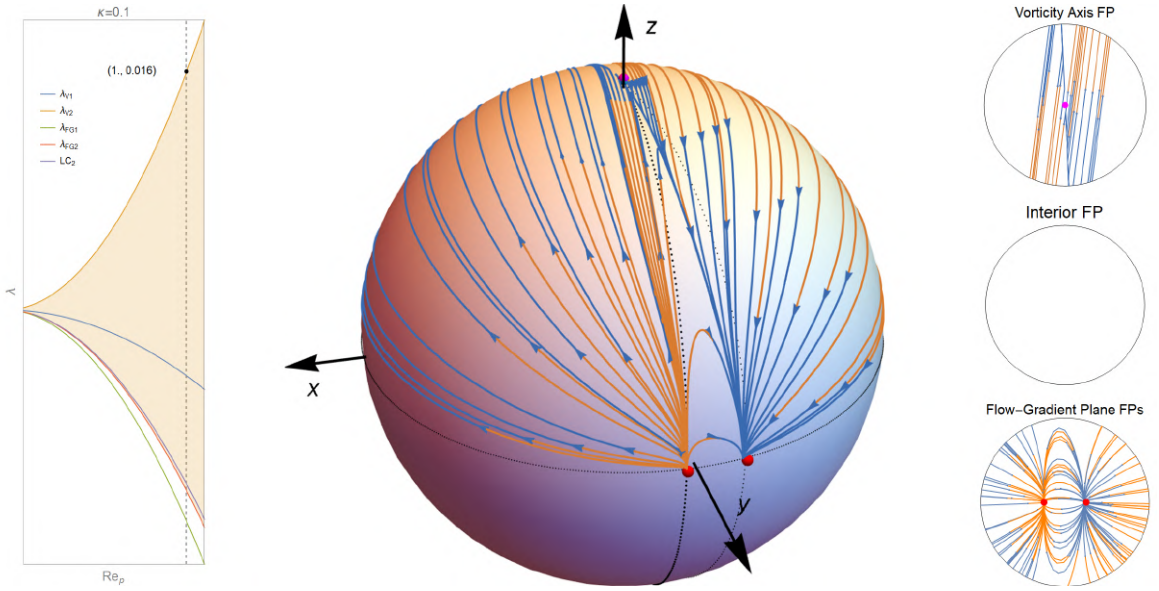

(i) $\lambda = 0.016$. The interior saddle reaches the vorticity axis and the vorticity axis fixed point transitions from a stable node to a saddle, as predicted from the fixed-point analysis.

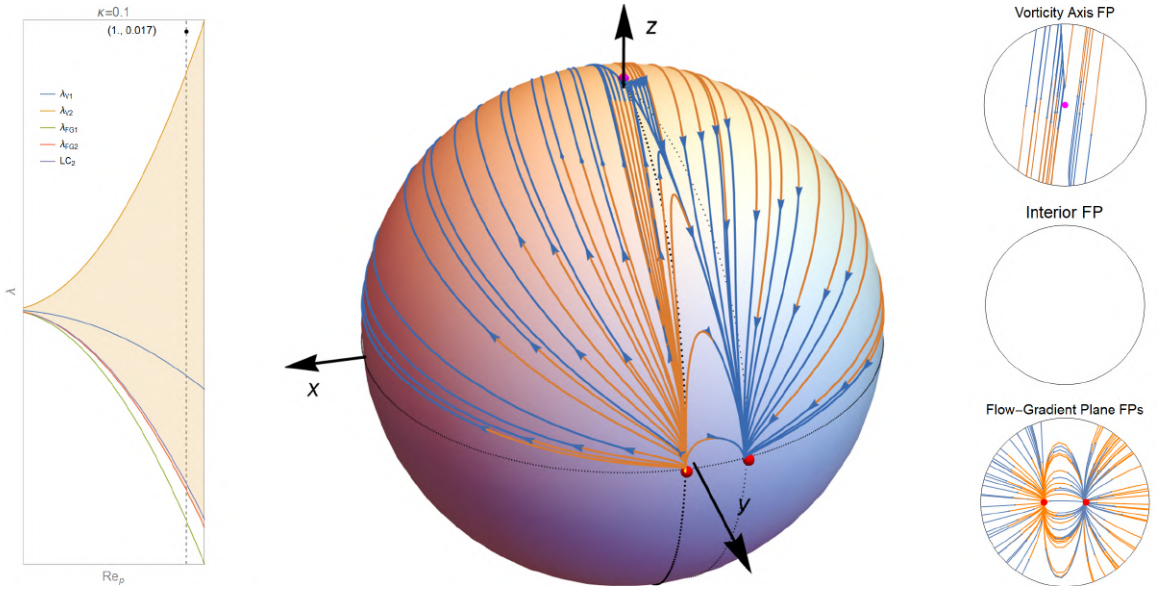

(j) $\lambda = 0.017$. No new bifurcations occur henceforth for increasing λ. The one-dimensional model in [9] predicts this state as λ is increased beyond κ^2.

Fig. 3.8 Global trajectory patterns for the oblate spheroid, with $\kappa = 0.1$, with increasing λ. For illustration purposes, *Re* has been taken to be 1. The inset on the left shows the four bifurcation regimes determined from the fixed-point analysis and an additional curve corresponding to the annihilation of the limit cycle. A black point within the inset denotes the current state of the system in the state space and indicates the bifurcation regime corresponding to each global trajectory plot. The shaded region in the inset indicates the regime where an interior fixed point exists. The figures on the right show the trajectory topology close to the visible fixed points.

The bifurcation scenario for the case without the limit cycle (and thence without the heteroclinic bifurcation) has been briefly discussed in Fig. 3.9

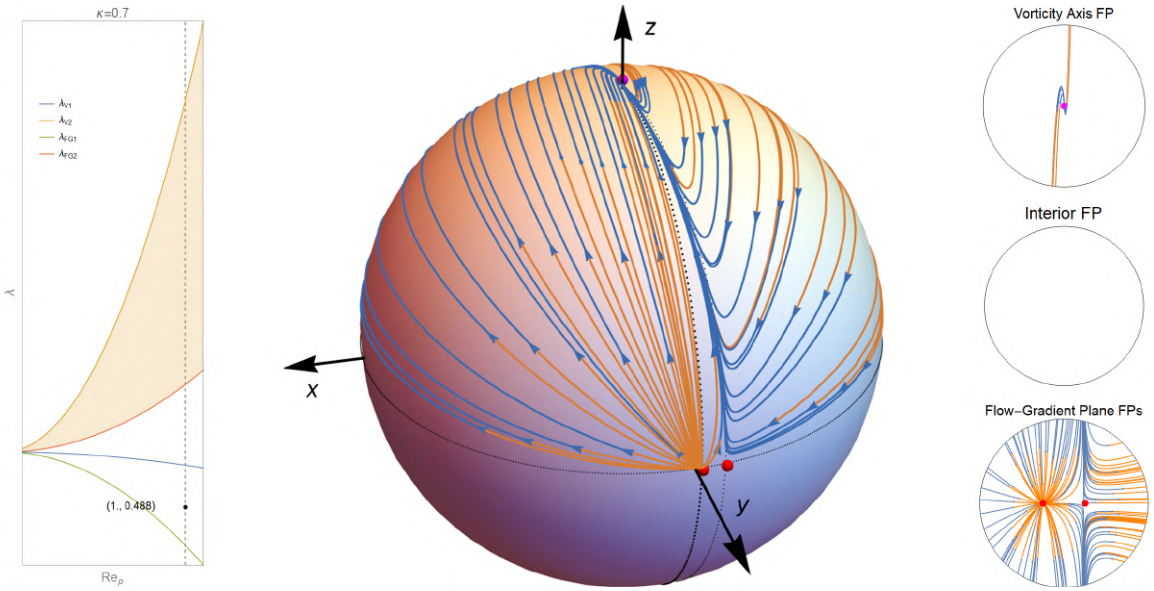

(a) $\lambda = 0.488$. λ_{FG1} now generates two unstable node - saddle pairs (only one pair visible) in the flow-gradient plane as opposed to the saddle - stable node pairs in the case with $\kappa < 0.328$ (fig. 3.8b).

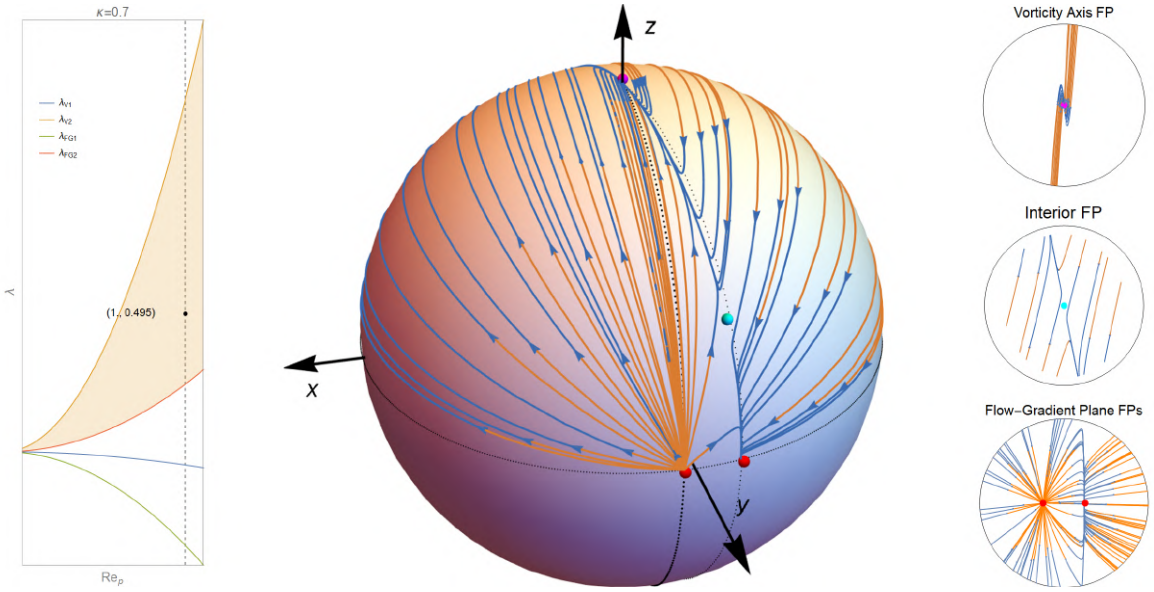

(b) $\lambda = 0.495$. λ_{FG2} now causes the saddle in the flow-gradient plane to bifurcate into a stable node and two saddles (only one visible) which emerge as interior fixed points. The interior saddle point retains its meridional trajectory in this case.

Fig. 3.9 Global trajectory patterns for the oblate spheroid, with $\kappa = 0.7$, $Re = 1$, with increasing λ.

3.3.2 Prolate Spheroid

Fixed points in the flow-gradient plane

The analysis for the prolate case proceeds along the same lines as that of the oblate spheroids. We therefore mention here only the key components of the analysis, starting with the bifurcations in the flow-gradient plane.

To begin with, assume that a fixed point exists in the flow gradient plane so that its coordinates are given by $(\theta,\phi) \equiv (\pi/2,\phi_0)$ such that $\phi_0 \ll 1$, that is the fixed point lies close to its value for the inertialess case. Substituting this in the equation for $\dot{\phi}$ (eq. 3.15), we obtain

$$-(\frac{1-\lambda}{2}) + 2\alpha(1-2\phi_0^2) + Re\ \phi_0\ \mathscr{G} = 0 \tag{3.27}$$

where $\alpha = \frac{1+\lambda}{4}\frac{\kappa^2-1}{\kappa^2+1}$ and $\mathscr{G} = G_1^f(\xi,\lambda) - G_2^f(\xi,\lambda) + G_3^f(\xi,\lambda) - G_4^f(\xi,\lambda)$. The solution to the quadratic is given by

$$\phi_0 = \frac{Re\,\mathscr{G} \pm \sqrt{Re^2\mathscr{G}^2 - \frac{4(1+\lambda)(\kappa^2-1)(1-\lambda\kappa^2)}{(\kappa^2+1)^2}}}{2(1+\lambda)\frac{\kappa^2-1}{\kappa^2+1}} \tag{3.28}$$

which is real only if

$$Re^2\mathscr{G}^2 - \frac{4(1+\lambda)(\kappa^2-1)(1-\lambda\kappa^2)}{(\kappa^2+1)^2} = 0 \tag{3.29}$$

The condition for the first bifurcation in the flow-gradient plane which results in two fixed points is then given by

$$Re^2\mathscr{G}^2 - \frac{4(1+\lambda_{FG1})(\kappa^2-1)(1-\lambda_{FG1}\kappa^2)}{(\kappa^2+1)^2} = 0 \tag{3.30}$$

In order to obtain the next bifurcation, we must determine the character of the generated fixed points. To this end, we linearize the system about $(\theta,\phi) \equiv (\pi/2,\phi_0)$. Consider the transformation

$$\hat{\theta} = \theta - \pi/2$$
$$\hat{\phi} = \phi - \phi_0$$

so that $\hat{\theta},\hat{\phi} \ll 1$. Linearization about $(\hat{\theta},\hat{\phi}) \equiv (0,0)$ yields the system of equations

$$\Rightarrow \begin{bmatrix} \dot{\hat{\theta}} \\ \dot{\hat{\phi}} \end{bmatrix} = \begin{bmatrix} -(1+\lambda)\frac{\kappa^2-1}{\kappa^2+1}\phi_0 - Re\mathscr{F} & 0 \\ 0 & -2(1+\lambda)\frac{\kappa^2-1}{\kappa^2+1}\phi_0 + Re\mathscr{G} \end{bmatrix} \begin{bmatrix} \hat{\theta} \\ \hat{\phi} \end{bmatrix} \tag{3.31}$$

where $\mathscr{F} = F_1^f(\xi,\lambda) + F_2^f(\xi,\lambda) - F_3^f(\xi,\lambda) + F_4^f(\xi,\lambda) - 2F_5^f(\xi,\lambda)$ and $\mathscr{G} = G_1^f(\xi,\lambda) - G_2^f(\xi,\lambda) + G_3^f(\xi,\lambda) - G_4^f(\xi,\lambda)$. The eigenvalues of this system of equation are simply its diagonal entries. It can be seen numerically, that the eigenvalue $-2(1+\lambda)\frac{\kappa^2-1}{\kappa^2+1}\phi_0 + Re\mathscr{G}$ does not change sign for either of the fixed points. The criterion for second bifurcation is thus obtained by substituting the coordinates of the fixed points (eq. 3.28) in the other eigenvalue. The criterion becomes

$$Re^2((\mathscr{G}+2\mathscr{F})^2 - \mathscr{G}^2) + \frac{4(1+\lambda_{FG2})(\kappa^2-1)(1-\lambda_{FG2}\kappa^2)}{(\kappa^2+1)^2} = 0 \tag{3.32}$$

We therefore have the criteria for the pair of bifurcations in the flow-gradient plane.

Fixed points on the vorticity axis

The bifurcation criteria for the vorticity axis bifurcations remains identical to the oblate case and are given by

$$Re^2(F_2^f)^2 + \left(\frac{\kappa^2-\lambda_{V1}}{\kappa^2+1}\right)\left(\frac{\lambda_{V1}\kappa^2-1}{\kappa^2+1}\right) = 0 \tag{3.33}$$

$$Re(F_1^f + F_3^f) - \sqrt{Re^2(F_2^f)^2 + \left(\frac{\kappa^2-\lambda_{V2}}{\kappa^2+1}\right)\left(\frac{\lambda_{V2}\kappa^2-1}{\kappa^2+1}\right)} = 0 \tag{3.34}$$

A plot of $\lambda_{FG1}, \lambda_{FG2}, \lambda_{V1}, \lambda_{V2}$ as given by the expressions 3.30, 3.32, 3.33 and 3.34, and its variation with κ has been shown in Fig. 3.10. The effect of fluid inertia on the bifurcation thresholds is shown in Fig. 3.11

Interior fixed points

As for the oblate spheroid, the parameter space lying between the second flow-gradient plane bifurcation (λ_{FG2} - red curve in fig. 3.10 and 3.11) and second vorticity axis bifurcation (λ_2 - orange curve in fig. 3.10 and 3.11) must include interior fixed points (in addition to those on the vorticity axis and in the flow-gradient plane) owing to the Euler characterstic requirement.

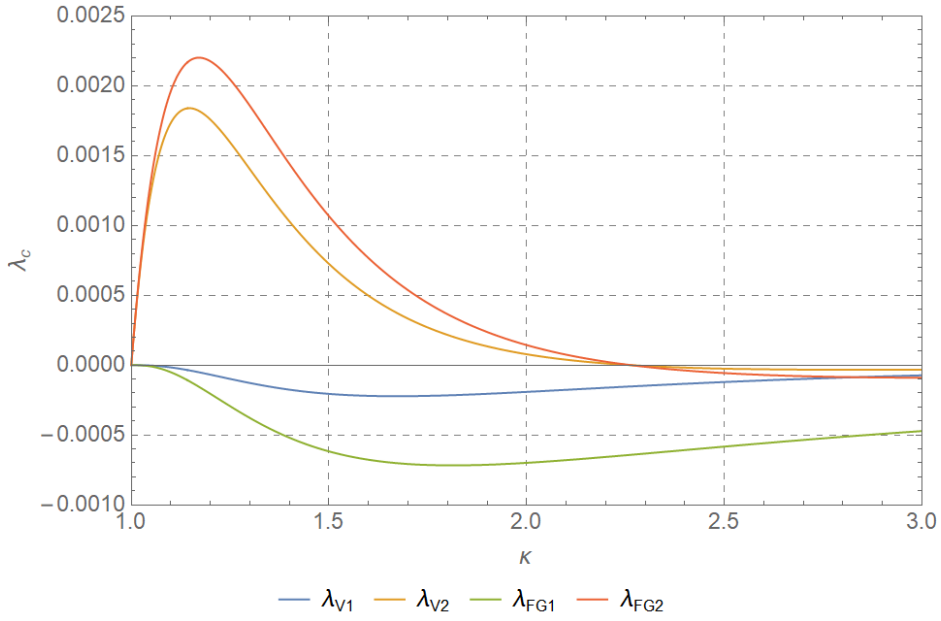

Fig. 3.10 Variation of critical λ with κ for a prolate spheroid for $Re = 0.5$. The Y-axis denotes deviation from $\lambda_c (= 1/\kappa^2)$.

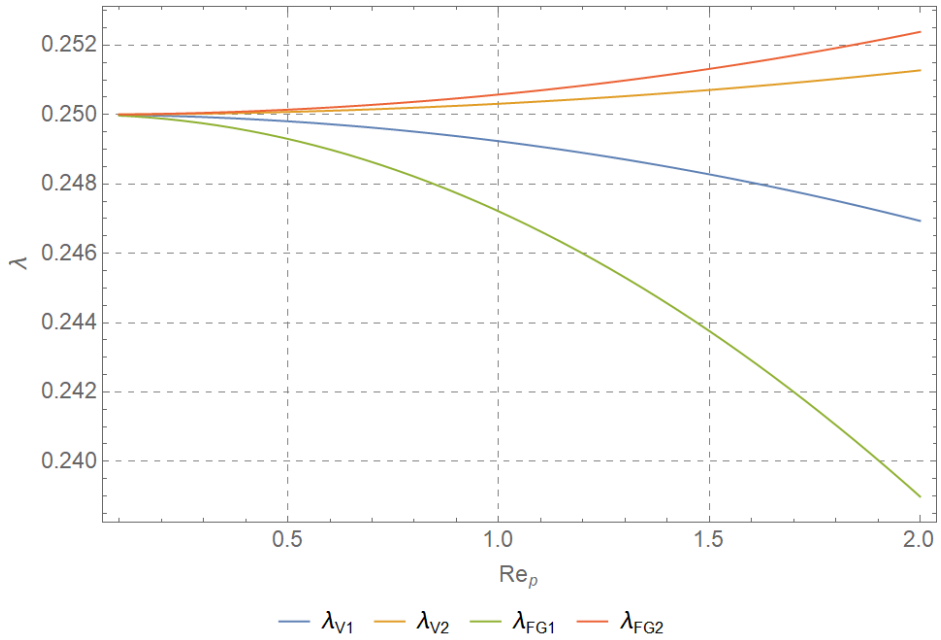

Fig. 3.11 Variation of critical λ with Re for a prolate spheroid with $\kappa = 2.0$.

The difference in the prolate case arises due to a crossing of the two bifurcation curves at $\kappa \approx 2.28$.

If $\kappa < 2.28$, increasing λ (for a fixed κ) causes the second bifurcation at the vorticity axis (λ_{V2}) to occur prior to the second bifurcation in the flow-gradient plane (λ_{FG2}). The interior fixed points are therefore generated at the vorticity axis and travel towards the flow-gradient plane with increasing λ. This is in contrast to the oblate case where, with increasing λ (for fixed *Re* and κ), the interior fixed points travel from the flow-gradient plane toward the vorticity axis. The bifurcation scenario in this regime can therefore be summarized as follows. For $\lambda < \lambda_{FG1}$, the vorticity axis consists of an unstable spiral and there are no fixed points in the flow-gradient plane. As λ increases beyond λ_{FG1}, a saddle and a stable node emerge in the flow-gradient plane. With increasing lambda, the vorticity axis spiral transforms to an unstable node at $\lambda = \lambda_{V1}$. As λ increases further beyond λ_{V2}, the unstable node at the vorticity axis bifurcates into a saddle, which remains at the vorticity axis and two unstable nodes which traverse towards the flow-gradient plane with increasing λ. These interior nodes coincide with the saddle in the flow-gradient plane at $\lambda = \lambda_{FG2}$ resulting finally in two stable / unstable node pairs in the flow-gradient plane and saddles along the vorticity axis. Fig. 3.12 illustrates this bifurcation sequence.

For $\kappa > 2.28$, the sequence of bifurcations with increasing λ is either $\lambda_{FG1} < \lambda_{V1} < \lambda_{FG2} < \lambda_{V2}$ (if $2.28 < \kappa < 2.83$) or $\lambda_{FG1} < \lambda_{FG2} < \lambda_{V1} < \lambda_{V2}$ (if $\kappa > 2.83$). Although the two sequences differ in the order of λ_{V1}, the transition of the vorticity axis fixed point from spiral to a node is inconsequential to the development of interior fixed points. In both these cases, two fixed points - a saddle and a stable node emerge in the flow-gradient plane as λ increases beyond λ_{FG1}. The saddle further bifurcates into two saddles and a stable node at $\lambda = \lambda_{FG2}$. With increasing λ, the interior saddle approaches the vorticity axis and, for $\lambda = \lambda_{V2}$, transforms the unstable node at the vorticity axis to a saddle. This sequence has been briefly demonstrated in fig. 3.13.

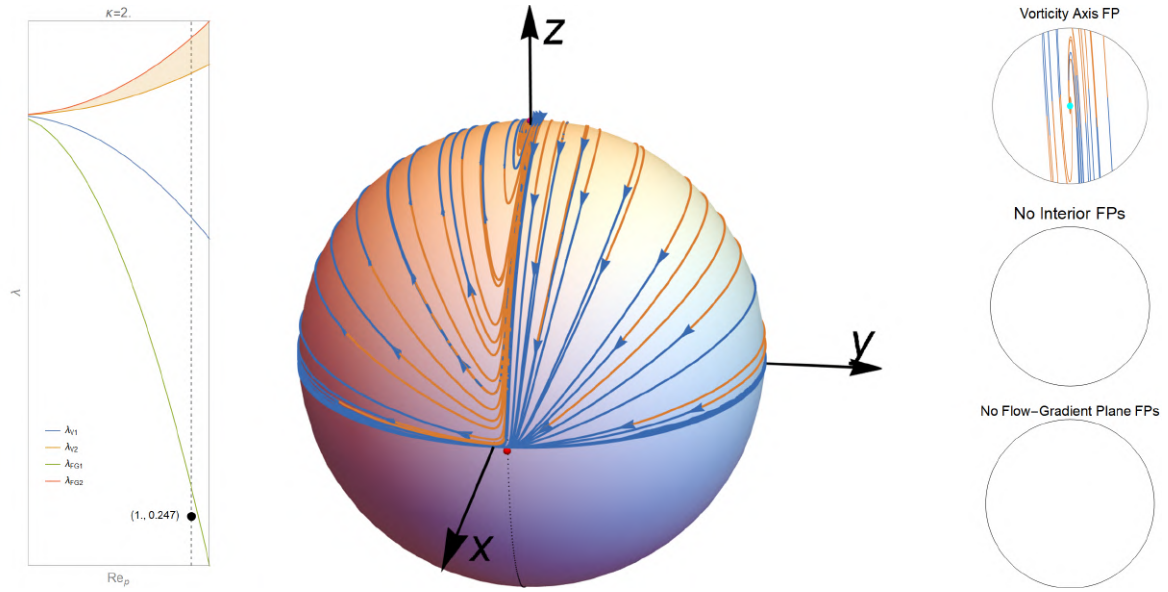

(a) $\lambda = 0.2470$. As for the oblate case, we start with a state already described by Marath and Subramanian [9]. In this state, there are no fixed points on the flow gradient plane and the vorticity axis fixed point is an unstable spiral.

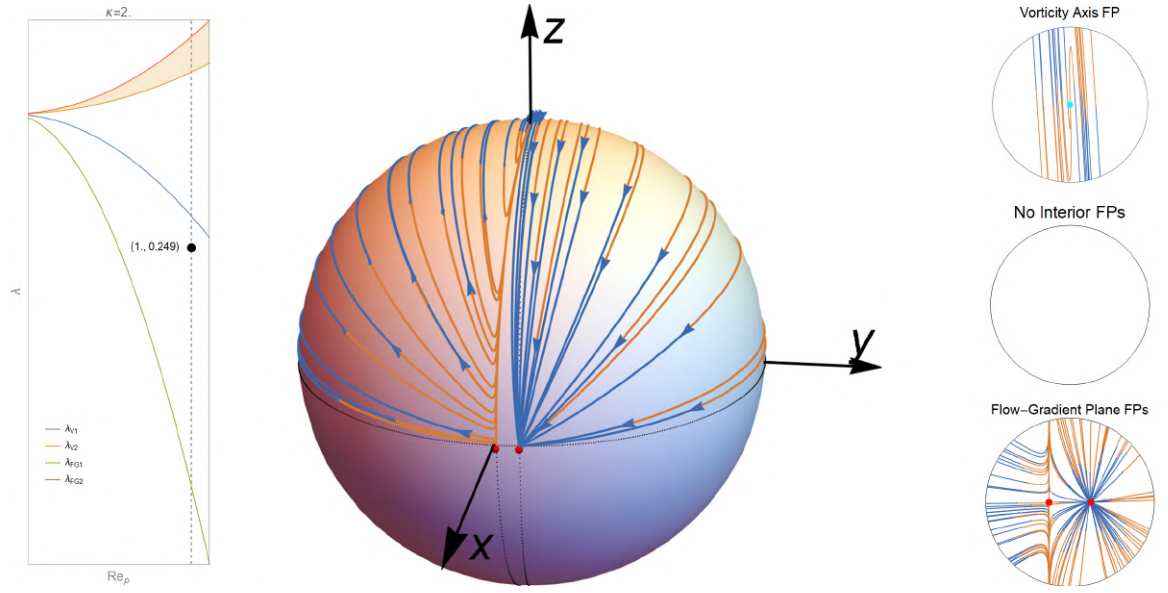

(b) $\lambda = 0.2490$. Two fixed points - a stable node and a saddle emerge in the flow gradient plane as λ is increased beyond λ_{FG1}. Two gray dotted lines denote meridians passing through flow gradient fixed points for reference.

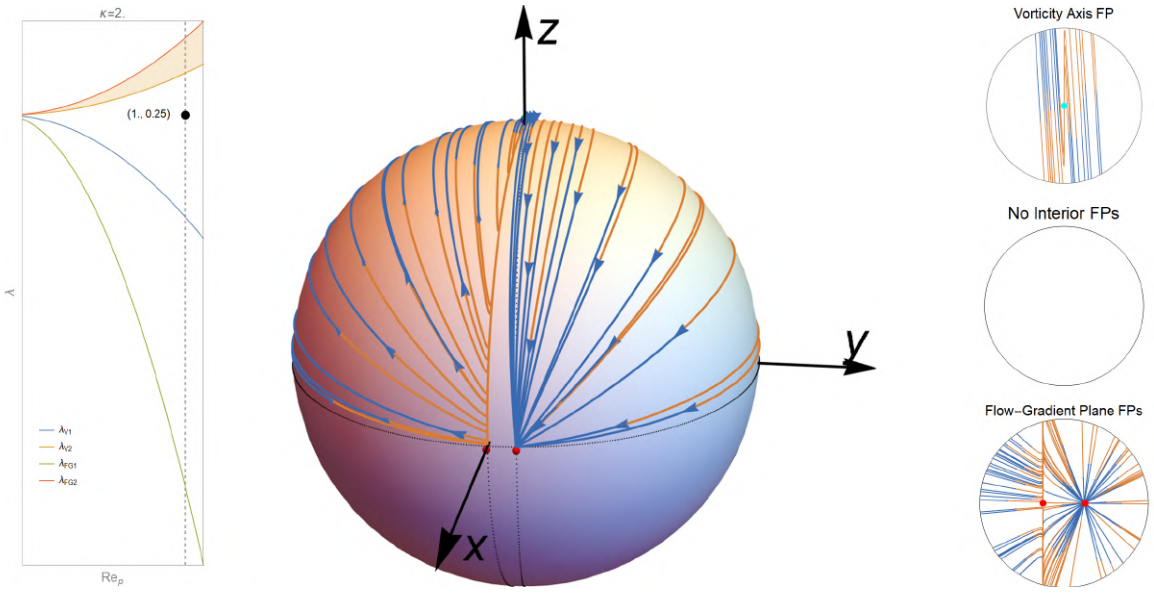

(c) $\lambda = 0.2500$. As λ increases beyond λ_{V1}, The vorticity axis spiral transforms to an unstable node.

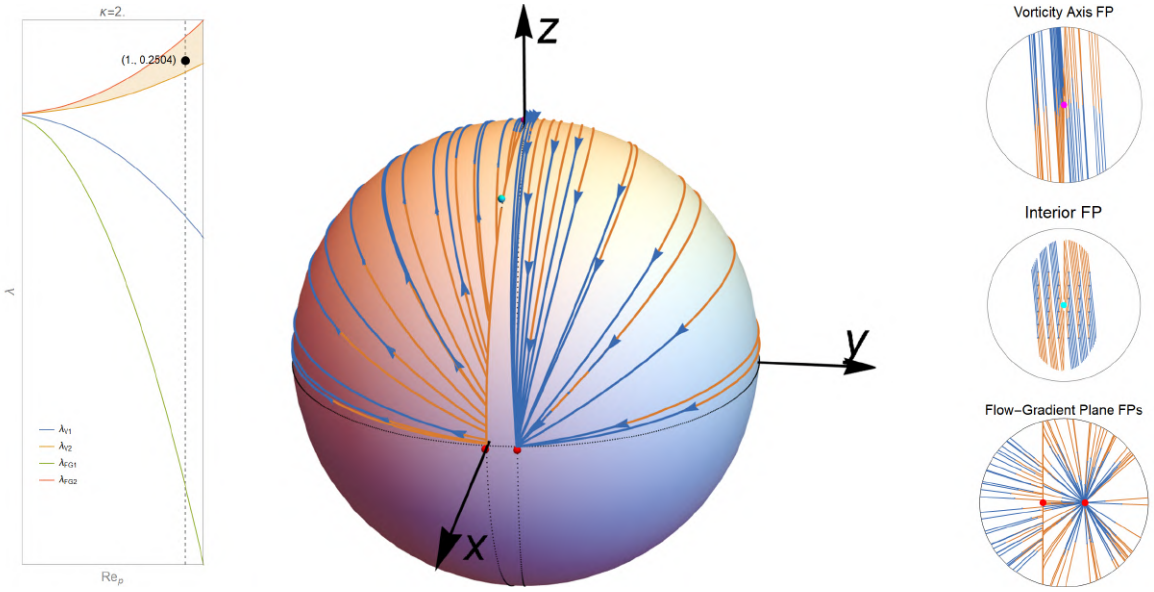

(d) $\lambda = 0.2504$. Increasing λ beyond λ_{V2} causes the unstable node at the vorticity axis to split into three fixed points - two unstable nodes (only one visible in the figure) and a saddle. The saddle stays at the vorticity axis and the two unstable nodes move towards the flow-gradient plane.

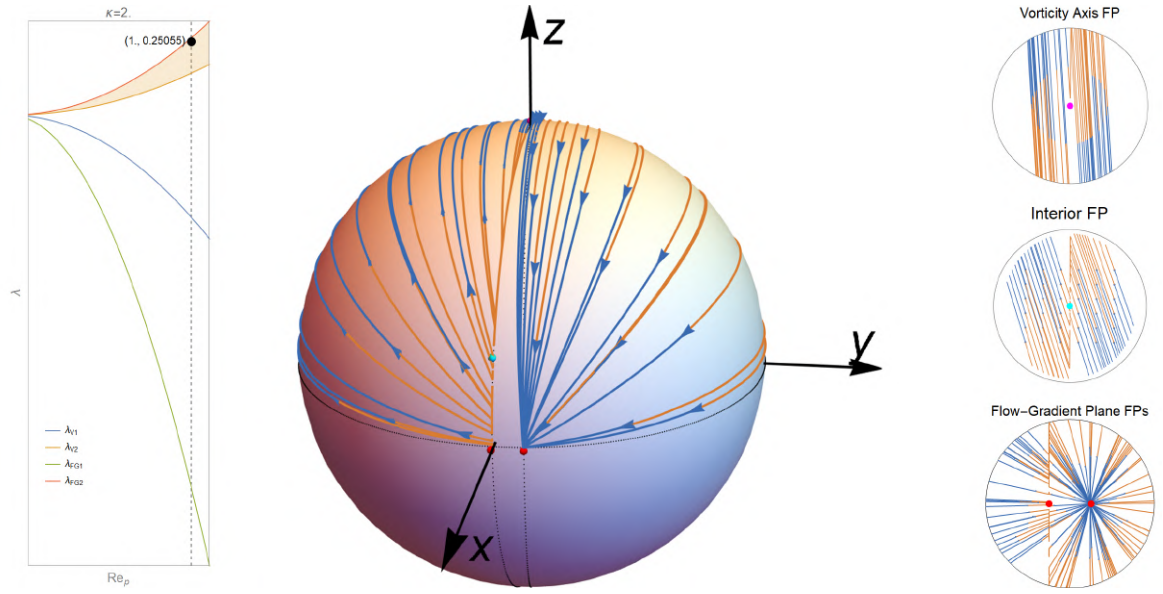

(e) $\lambda = 0.25055$. As λ increases further, the interior fixed points move toward the flow-gradient plane along a meridian passing through a fixed point in the flow-gradient plane.

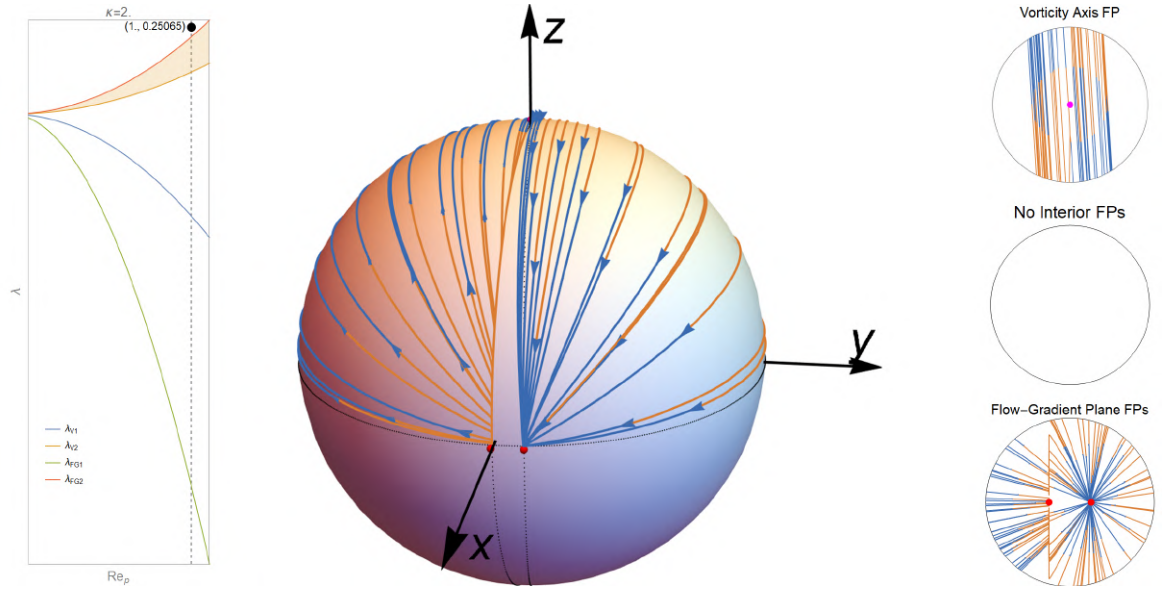

(f) $\lambda = 0.25065$. As λ increases past λ_{FG2}, two interior nodes collide with the flow-gradient saddle (one from each hemisphere) and result in an unstable node. In the final configuration, we have two saddles at the vorticity axis and two pairs of stable and unstable nodes in the flow-gradient plane, as expected due to the one-dimensional analysis of Marath and Subramanian [9].

Fig. 3.12 Global trajectory patterns for the prolate spheroid, with $\kappa = 0.1$, with increasing λ. For illustration purposes, Re has been taken to be 1. The inset on the left shows the bifurcation regimes determined from the fixed-point analysis. A black point within the inset denotes the current state of the system in the state space and indicates the bifurcation regime corresponding to each global trajectory plot. The shaded region in the inset indicates the regime where an interior fixed point exists. The figures on the right show the trajectory topology close to the visible fixed points.

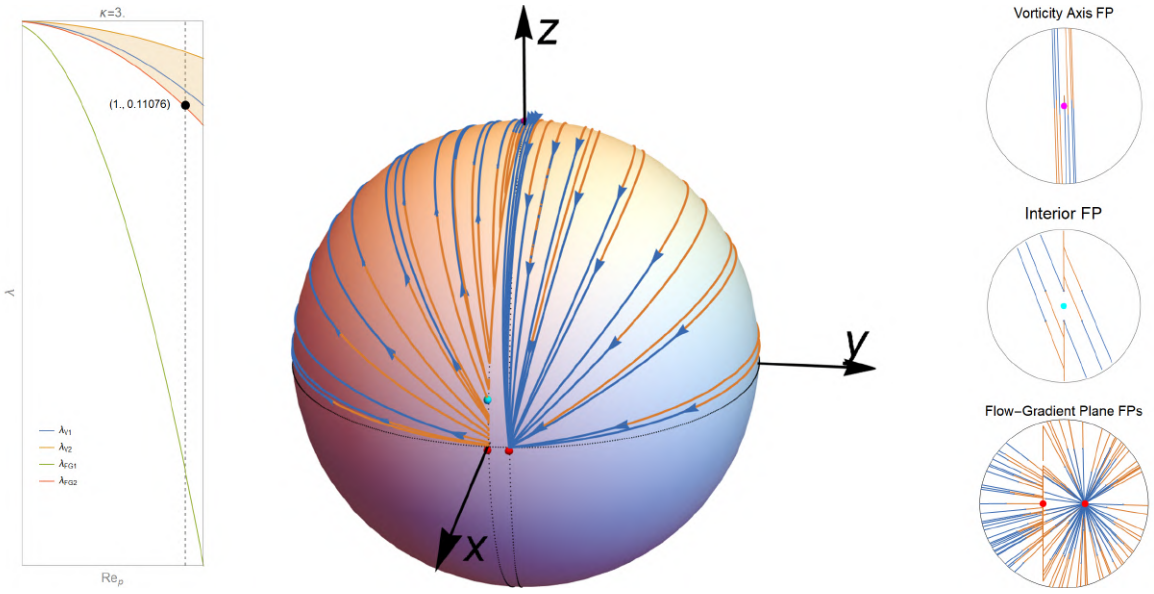

(a) $\lambda = 0.11076$. At $\lambda = \lambda_{FG2}$, the saddle in the flow-gradient plane bifurcates to yield an unstable node in the flow-gradient plane and two interior saddles (only one visible).

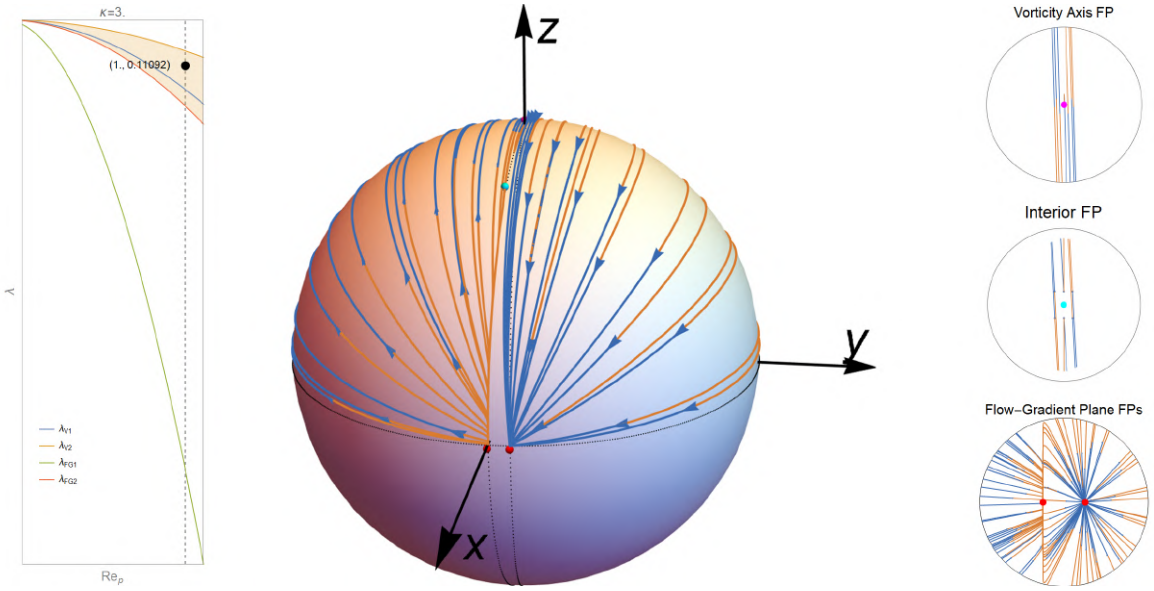

(b) $\lambda = 0.11092$. With increasing λ, the interior saddles travel toward the vorticity axis, eventually coalescing with the vorticity axis fixed point at $\lambda = \lambda_{V2}$

Fig. 3.13 Global trajectory topology for a spheroid with $\kappa = 3$, $Re = 1$ and increasing λ. For prolate spheroids with $\kappa > 2.28$, the interior fixed point is a saddle which it emerges from the saddle in the flow-gradient plane and moves towards the vorticity axis. If $\kappa < 2.28$, the interior fixed point is an unstable node which emerges from the vorticity axis and moves towards the saddle in the flow-gradient plane (fig. 3.12).

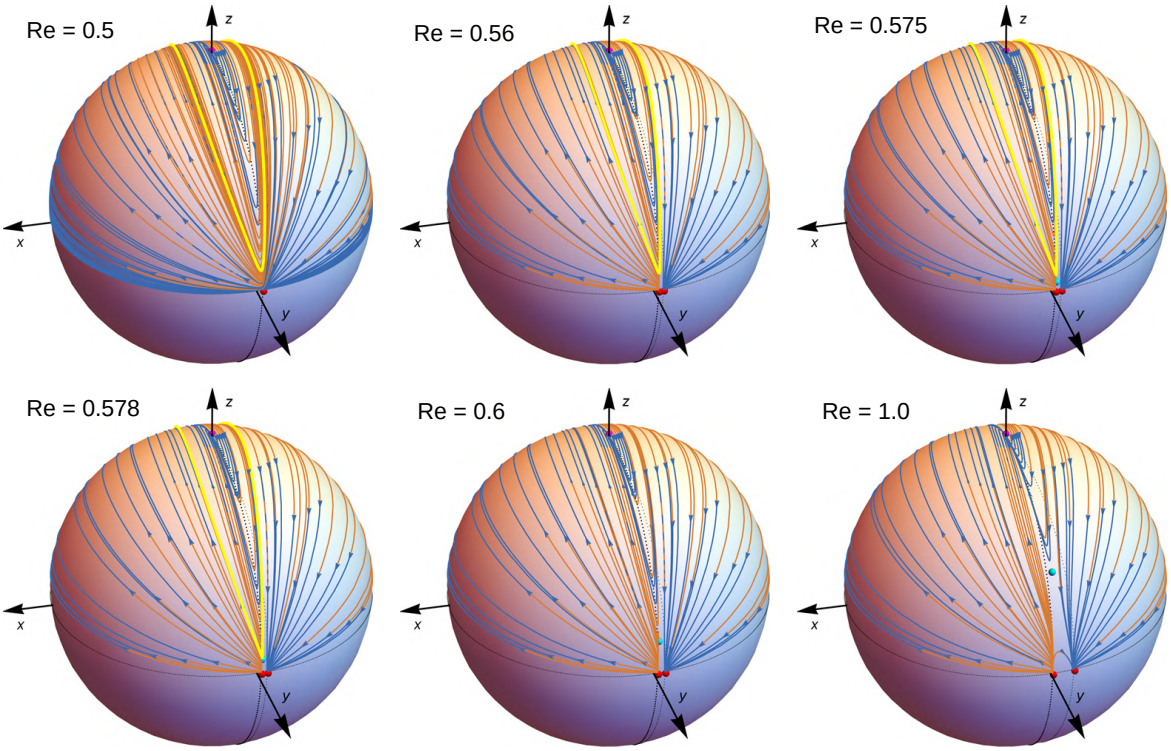

Fig. 3.14 Trajectory topology sequence for an oblate spheroid with $\kappa = 0.1$, $\lambda = 0.0085$ and increasing *Re*. Most of the regimes illustrated in Fig. 4 of [14] can be seen here, except the transformation of the vorticity axis node to a saddle.

3.4 Conclusion

We have presented our findings on bifurcations in trajectory topology of prolate and oblate spheroids suspended in a planar linear flow. Earlier works by Lundell et al [14] have obtained similar results via numerical simulations of neutrally buoyant spheroids in simple shear flow. Fig. 4 in [14] demonstrates the trajectory topology for a neutrally buoyant oblate spheroid with $\kappa = 0.25$, $\lambda = 0$ and increasing *Re*. Fig. 3.14 presents an analogous figure for a light oblate spheroid (no particle inertia) suspended in a linear flow with $\kappa = 0.1$, $\lambda = 0.0085$ and increasing *Re*. Most of the bifurcation regimes defined by Lundell et al in [] can be seen in this figure. The key difference between the two sequences lies in the order of the bifurcations. We believe that this difference can be attributed to the absence of particle inertia. Preliminary work on inclusion of particle inertia in the aforementioned analysis shows that this is indeed able to alter the order of the bifurcations in fig. 3.14 occur while the nature of these bifurcations remains unaltered.

In a separate article [15] Lundell et al have summarized the bifurcations of spheroids suspended in simple shear flows via a *Re* vs κ plot (Fig. 11 in [15]). This plot includes both,

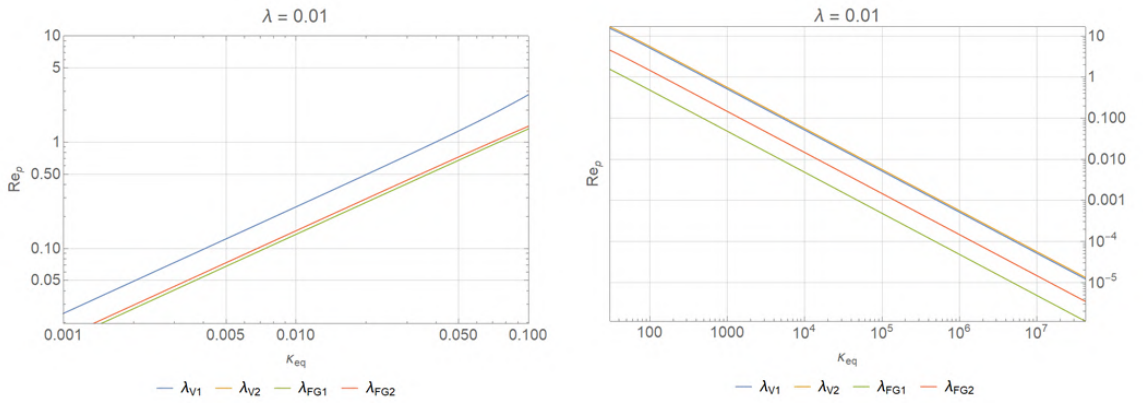

Fig. 3.15 A Log-Log plot for Re vs κ_{eq} for $\lambda = 0.01$ for oblate (left) and prolate (right) spheroids.

the numerical findings for moderate aspect ratios and analytical results for extreme aspect ratio spheroids. We have similarly illustrated the bifurcations on the Re vs κ_{eq} plane for both oblate (left) and prolate (right) spheroids in fig. 3.15. Here, κ_{eq} is defined as

$$\kappa_{eq} = \frac{\kappa^2 - \lambda}{1 - \kappa^2 \lambda} \tag{3.35}$$

which maps critical oblate spheroids ($\kappa = \sqrt{\lambda}$) to zero and critical prolate spheroids ($\kappa = 1/\sqrt{\lambda}$) to infinity. On a log axis then, one has critical oblate spheroids to the extreme left, spherical particles ($\kappa = \kappa_{eq} = 1$) in the center and critical prolate spheroids to the extreme right. The curves in fig. 3.15 denote the asymptotes for these extreme equivalent aspect ratio spheroids for the bifurcations discussed in this chapter. The usage of κ_{eq} will allow us to generalize this plot to the entire family of planar linear flows. Furthermore, we intend to include the effects of particle inertia and compare our analytical results to the computational results in [14]. This will allow us to show that the dynamics required for the bifurcations obtained in [14] is contained in the equations derived in [9].

References

[1] Chandrasekhar, S. (1981). *Hydrodynamic and Hydromagnetic Stability*. Dover Books on Physics Series. Dover Publications.

[2] Drazin, P. G. and Reid, W. H. (2004). *INTRODUCTION*, page 1–31. Cambridge Mathematical Library. Cambridge University Press, 2 edition.

[3] Gillis, J. and Kaufman, B. (1962). The stability of a rotating viscous jet. *Quarterly of Applied Mathematics*, 19(4):301–308.

[4] Hocking, L. M. (1960). The stability of a rigidly rotating column of liquid. *Mathematika*, 7(1):1–9.

[5] Hocking, L. M. and Michael, D. H. (1959). The stability of a column of rotating liquid. *Mathematika*, 6(1):25–32.

[6] Jha, N. K. and Govardhan, R. (2015). Interaction of a vortex ring with a single bubble: bubble and vorticity dynamics. *Journal of Fluid Mechanics*, 773:460–497.

[7] Kubitschek, J. P. and Weidman, P. D. (2007). The effect of viscosity on the stability of a uniformly rotating liquid column in zero gravity. *Journal of Fluid Mechanics*, 572:261–286.

[8] Leal, L. and Hinch, E. (1971). The effect of weak brownian rotations on particles in shear flow. *Journal of Fluid Mechanics*, 46(4):685–703.

[9] Marath, N. K. and Subramanian, G. (2018). The inertial orientation dynamics of anisotropic particles in planar linear flows. *Journal of Fluid Mechanics*, 844:357–402.

[10] Moore, D. and Saffman, P. G. (1971). Structure of a line vortex in an imposed strain. In *Aircraft wake turbulence and its detection*, pages 339–354. Springer.

[11] Moore, D. W. and Saffman, P. G. (1975). The instability of a straight vortex filament in a strain field. *Proceedings of the Royal Society of London. A. Mathematical and Physical Sciences*, 346(1646):413–425.

[12] Pedley, T. (1967). The stability of rotating flows with a cylindrical free surface. *Journal of Fluid Mechanics*, 30(1):127–147.

[13] Rayleigh, L. (1878). On the instability of jets. *Proceedings of the London mathematical society*, 1(1):4–13.

[14] Rosén, T., Do-Quang, M., Aidun, C., and Lundell, F. (2015). Effect of fluid and particle inertia on the rotation of an oblate spheroidal particle suspended in linear shear flow. *Physical Review E*, 91(5):053017.

[15] Rosén, T., Nordmark, A., Aidun, C. K., Do-Quang, M., and Lundell, F. (2016). Quantitative analysis of the angular dynamics of a single spheroid in simple shear flow at moderate reynolds numbers. *Physical Review Fluids*, 1(4):044201.

[16] Rosenthal, D. (1962). The shape and stability of a bubble at the axis of a rotating liquid. *Journal of Fluid Mechanics*, 12(3):358–366.

[17] Ross, D. K. (1974). Stability of an annulus of rotating liquid to plane disturbances. *The Physics of Fluids*, 17(6):1119–1120.

[18] Thomson, W. (1880). Xxiv. vibrations of a columnar vortex. *The London, Edinburgh, and Dublin Philosophical Magazine and Journal of Science*, 10(61):155–168.

[19] Tsai, C.-Y. and Widnall, S. E. (1976). The stability of short waves on a straight vortex filament in a weak externally imposed strain field. *Journal of Fluid Mechanics*, 73(4):721–733.

[20] Weidman, P., Goto, M., and Fridberg, A. (1997). On the instability of inviscid, rigidly rotating immiscible fluids in zero gravity. *Zeitschrift für angewandte Mathematik und Physik ZAMP*, 48(6):921–950.